

**X-ray Absorption Spectroscopy of Pd₄₀Ni₄₀P₂₀ Metallic Glass
and Boron Doped Silicon**

**X-RAY ABSORPTION SPECTROSCOPY OF Pd₄₀Ni₄₀P₂₀ METALLIC
GLASS AND BORON DOPED SILICON**

BY

Frank Joseph Esposto, B.Sc. (Hons.)

A thesis submitted to the school of Graduate
Studies in partial fulfilment of the
requirements for the degree of
Master of Science

Department of Chemistry
McMaster University

July 1990

Hamilton

Ontario

Canada

MASTER OF SCIENCE (1990)

McMASTER UNIVERSITY

Hamilton, Ontario.

**TITLE: X-ray Absorption Spectroscopy of Pd₄₀Ni₄₀P₂₀ Metallic Glass
and Boron Doped Silicon**

AUTHOR: Frank J. Esposito, B.Sc. (Hons.) (University of Windsor)

SUPERVISOR: Dr. A.P. Hitchcock, Ph.D. (UBC)

NUMBER OF PAGES: xiii, 169

ABSTRACT

Ni K extended X-ray absorption fine structure spectroscopy recorded with synchrotron radiation at 77 K and 300 K, has been used to investigate various annealed $\text{Pd}_{40}\text{Ni}_{40}\text{P}_{20}$ metallic glass samples. The structural parameters (radial distance, coordination number, Debye Waller factor) for the Fourier filtered first coordination shell were obtained via curve analysis using MFIT (multifitting analysis) and plotted as a function of annealing temperature. Similar trends between 77 K and 300 K data were not observed in all cases. These results lead one to believe that the curve fitting procedure is not yet optimized and makes one sceptical of attributing any meaning to the results.

X-ray absorption near edge spectroscopy via electron yield detection has also been used to study the B K edge in boron doped silicon. It was found that a strong peak at 195 eV is directly related to trigonally coordinated boron. Non trigonally coordinated boron did not seem to produce this spike. Results show that B 1s spectroscopy is a very sensitive probe of the local structure of boron.

ACKNOWLEDGEMENT

The author would like to express his gratitude to a number of individuals. Foremost of these is my supervisor Dr. A.P. Hitchcock who has allowed this thesis to be possible. In addition, I would like to thank R. Brüning, a graduate student from McGill University, for all of his help regarding the metallic glass project, and Dr. T.E. Jackman from the National Research Council (NRC) in Ottawa, for his kind support as well as giving me the opportunity to be the prime investigator in our research. I would also like to express my appreciation to Dr. T. Tyliczszak who has been very helpful, even at times when "the going got rough".

The author acknowledges the people responsible for each of the beam lines for their help and use of the lines; Dr. T. Elam (NIST-X23B), Dr. C.E. Bouldin (NRL-X23A2), G.M. Lamble, J. Scrofani (NRL-X11A), Dr. K.H. Tan, Dr. J.D. Bozek, Dr. Jin-Ming Chen (CSRF-grasshopper) and the CHESS staff scientists.

A special thank you to my wife Rhonda, for her patience and kind encouragement throughout my M.Sc. studies. Finally to my parents Mr. and Mrs. Salvatore Esposto, who have been extremely supportive throughout my academic career. This thesis is dedicated in a special way to both of them.

TABLE OF CONTENTS

DESCRIPTIVE NOTE.....	ii
ABSTRACT.....	iii
ACKNOWLEDGEMENTS.....	iv
TABLE OF CONTENTS.....	v
LIST OF FIGURES.....	viii
LIST OF TABLES.....	xii
INTRODUCTION.....	1
CHAPTER 1: BASIC PRINCIPLES.....	4
1.1 General Introduction.....	4
1.2 Theory of X-ray Absorption.....	4
1.3 X-ray Absorption Coefficients.....	8
1.4 EXAFS Theory.....	10
1.5 The EXAFS Equation.....	15
1.6 Theory of XANES.....	18
CHAPTER 2: EXPERIMENTAL.....	23
2.1 General Introduction.....	23
2.2 Synchrotron Radiation.....	24
2.3 Transmission Technique.....	25
2.4 Electron Yield Technique.....	32
(a) Electron Yield.....	32
(b) B 1s Detection.....	35
2.5 Sample Preparations.....	37
(a) Transmission.....	37
(b) Pd ₄₀ Ni ₄₀ P ₂₀ Metallic Glass Samples.....	40
(c) Si(B) Semiconductor.....	41
CHAPTER 3: EXAFS DATA ANALYSIS.....	42
3.1 General Introduction.....	42
3.2 Extraction of EXAFS and Fourier Analysis.....	43
(a) EXAFS Extraction.....	43

(b) Fourier Analysis.....	45
(c) Phase Shifts and Backscattering Amplitudes.....	49
3.3 Single Component Ratio Method Analysis.....	51
3.4 Multi Component Analysis.....	54
(a) General Aspects.....	54
(b) General Procedures for MFIT.....	57
(c) Fitting of Ni Metal using Theoretical and Experimental Phase Shifts and Amplitudes.....	61
3.5 Errors in Analysis.....	65
 CHAPTER 4: NI 1s EXAFS FOR Pd ₄₀ Ni ₄₀ P ₂₀ METALLIC GLASS	 67
4.1 General Introduction.....	67
4.2 Introduction.....	68
4.3 Scientific Problem.....	72
4.4 Preliminary Steps in Analysis of Pd ₄₀ Ni ₄₀ P ₂₀ EXAFS Data.....	74
4.5 Comparison of the EXAFS of Amorphous Pd ₄₀ Ni ₄₀ P ₂₀ and Crystalline Pd ₅₀ Ni ₅₀	75
4.6 Investigation of the Sensitivity of Ni K and Pd K EXAFS to the First Shell Composition.....	81
4.7 Ni, Pd, and Backscattering Amplitudes.....	88
4.8 EXAFS Difference Plots.....	90
4.9 Multiple Fitting Procedures for the Pd ₄₀ Ni ₄₀ P ₂₀ Irreversibly and Reversibly annealed samples.....	94
4.10 Presentation and Discussion of Multiple Fit Analysis for the Irreversibly and Reversibly Annealed Pd ₄₀ Ni ₄₀ P ₂₀ samples.....	101
(a) Irreversible Annealing.....	109
(b) Reversible Annealing.....	112
4.11 Discussion and Conclusions.....	113
 CHAPTER 5: B 1s NEAR EDGE SPECTRA OF Si(B) AND MODEL COMPOUNDS	 116
5.1 General Introduction.....	116
5.2 Introduction.....	116
(a) Silicon Semiconductors.....	116
(b) Doping of Silicon Semiconductors.....	117
(c) Boron Doped Silicon.....	120

5.3 EHT Procedures.....	123
5.4 The I_0 Normalization Problem.....	127
5.5 B 1s Spectra of Model Compounds.....	128
5.6 Effect of Etching on Si 2p and B 1s Spectra: Depth Sensitivity of Electron Yield Detection.....	135
5.7 Effect of Annealing on B 1s Spectra and B Environment.....	138
5.8 Conclusions.....	144
 CHAPTER 6: Concluding Remarks	 148
 REFERENCES.....	 150
 APPENDIX I Multiple Fitting Results Obtained from MFIT for Various Irreversibly Annealed Pd ₄₀ Ni ₄₀ P ₂₀ Samples Recorded at 300 K with Synchrotron Radiation.....	 159
 APPENDIX II Multiple Fitting Results Obtained from MFIT for Various Reversibly Annealed Pd ₄₀ Ni ₄₀ P ₂₀ Samples Recorded at 300 K with Synchrotron Radiation.....	 161
 APPENDIX III Multiple Fitting Results Obtained from MFIT for Various Irreversibly Annealed Pd ₄₀ Ni ₄₀ P ₂₀ Samples Recorded at 77 K with Synchrotron Radiation.....	 164
 APPENDIX IV Multiple Fitting Results Obtained from MFIT for Various Reversibly Annealed Pd ₄₀ Ni ₄₀ P ₂₀ Samples Recorded at 77 K with Synchrotron Radiation.....	 166

LIST OF FIGURES

Fig. 1.1	Variation of absorption coefficient in terms of increasing energy.....	7
Fig. 1.2	Arrangement for X-ray Absorption.....	7
Fig. 1.3	Experimental Ni K X-ray absorption spectrum of nickel metal recorded with synchrotron radiation.....	11
Fig. 1.4	Schematic representation of an EXAFS event.....	14
Fig. 1.5	Photoelectron scattering paths.....	17
Fig. 2.1	Spectral distribution of synchrotron Radiation from bending magnets.....	26
Fig. 2.2	Floor plan of the National Synchrotron Light Source experimental area.....	28
Fig. 2.3	Schematic of the transmission XAS experiment.....	29
Fig. 2.4	Schematic of the typical electronics used for transmission mode XAS.....	31
Fig. 2.5	The Ni-K edge EXAFS of the "as made" sample of amorphous $\text{Ni}_{40}\text{Pd}_{40}\text{P}_{20}$ for X-ray absorption and electron yield measurements.....	33
Fig. 2.6	Schematic illustration of a typical electron yield experiment. The entire system is under vacuum.....	36

Fig. 2.7	Incident photon flux (I_0) spectrum from the CSRF grasshopper monochromator.....	38
Fig. 3.1	The steps performed for EXAFS extraction.....	44
Fig. 3.2	Steps performed for Fourier analysis.....	47
Fig. 3.3	Calculated and experimental Ni metal phase shifts.....	50
Fig. 3.4	An example illustrating the fitting quality obtained for filtered first shell EXAFS of four irreversibly annealed $\text{Pd}_{40}\text{Ni}_{40}\text{P}_{20}$ samples.....	58
Fig. 3.5	Ni K-edge fitting of the first four coordination shells of nickel metal using calculated and experimental phase shifts and amplitudes.....	62
Fig. 4.1	X-ray diffraction results of various irreversibly and reversibly annealed $\text{Pd}_{40}\text{Ni}_{40}\text{P}_{20}$ metallic glass samples states.....	73
Fig. 4.2	Ni K-edge EXAFS and Fourier transforms of a polycrystalline $\text{Ni}_{50}\text{Pd}_{50}$ alloy and "as made" and reference state (608 K) amorphous $\text{Pd}_{40}\text{Ni}_{40}\text{P}_{20}$ sample measured at 300 K.....	77
Fig. 4.3	Pd K-edge EXAFS and Fourier transforms of a polycrystalline $\text{Ni}_{50}\text{Pd}_{50}$ alloy and "as made" and reference state (613 K) amorphous $\text{Pd}_{40}\text{Ni}_{40}\text{P}_{20}$ sample measured at 300K.....	78
Fig. 4.4	FTs of Simulations of the Ni K EXAFS of $\text{Pd}_x\text{Ni}_{1-x}$ ($0 < x < 1$) for two different structural models.....	82

Fig. 4.5	FTs of Simulations of the Pd K EXAFS of $\text{Pd}_x\text{Ni}_{1-x}$ ($0 < x < 1$) for two different structural models.....	83
Fig. 4.6	Comparing the Fourier transforms of the Ni K EXAFS of $\text{Pd}_{50}\text{Ni}_{50}$ alloy, to simulations of $\text{Pd}_{0.5}\text{Ni}_{0.5}$ and $\text{Pd}_{0.5}\text{Ni}_{0.5}\text{P}_{0.25}$ for two structural models.....	86
Fig. 4.7	Comparing calculated Ni, Pd, P and experimental backscattering amplitudes.....	89
Fig. 4.8	Ni K-edge EXAFS difference plots of various irreversible $\text{Pd}_{40}\text{Ni}_{40}\text{P}_{20}$ samples measured at 300 K.....	91
Fig. 4.9	Ni K-edge EXAFS difference plots of various reversible $\text{Pd}_{40}\text{Ni}_{40}\text{P}_{20}$ samples measured at 300 K.....	92
Fig. 4.10	Ni K-edge EXAFS difference plots of various reversible $\text{Pd}_{40}\text{Ni}_{40}\text{P}_{20}$ samples measured at 77 K.....	93
Fig. 4.11	Flowchart showing the order in which the samples measured at 300 K have been fitted.....	99
Fig. 4.12	Flowchart showing the order in which the samples measured at 77 K have been fitted.....	100
Fig. 4.13	Radial distance versus annealing temperature for various irreversible samples.....	103
Fig. 4.14	Coordination number versus annealing temperature for various irreversible samples.....	104
Fig. 4.15	Debye Waller versus annealing temperature for various irreversible samples.....	105

Fig. 4.16	Radial distance versus annealing temperature for various reversible samples.....	106
Fig. 4.17	Coordination number versus annealing temperature for various reversible samples.....	107
Fig. 4.18	Debye Waller versus annealing temperature for various reversible samples.....	108
Fig. 5.1	The one dimensional band structure of intrinsic, n-type, and p-type semiconductors.....	118
Fig. 5.2	Comparison of the B 1s experimental and calculated spectra for BF ₃ (gas) and KBF ₄ (solid) [SM+83].....	129
Fig. 5.3	EHT calculation of the B 1s spectra of B(OH) ₃ , BO ₃ (simulating B ₂ O ₃), B ₁₂ (elemental boron) and BSi ₄ (substitutional boron in Si).....	132
Fig. 5.4	B 1s spectra of B(OH) ₃ , B ₂ O ₃ , and β-rhombohedral boron measured by electron yield detection.....	134
Fig. 5.5	Comparison of the Si 2p and B 1s spectra from the high concentration as-grown sample.....	136
Fig. 5.6	Comparison of the B 1s spectra of the high (271) and low (658) concentration samples.....	139

LIST OF TABLES

Table 1.1	X-ray spectroscopic symbols.....	5
Table 2.1	Synchrotron ring properties.....	25
Table 3.1	Illustration of MFIT.....	59
Table 3.2	Parameter results obtained from the fitting of the first four coordination shells of Ni metal using both calculated and experimental phase shifts and amplitudes.....	63
Table 4.1	Various samples recorded with synchrotron radiation.....	76
Table 4.2	Variance (S) results obtained as a function of R for various samples.....	96
Table 4.3	Variance (S) results obtained as a function of DW for various samples.....	96
Table 4.4	Slopes, intercepts, and correlation values for the irreversible and reversible least square plots. Samples measured at 300 K.....	110
Table 4.5	Slopes, intercepts, and correlation values for the irreversible and reversible least square plots. Samples measured at 77 K.....	111

Table 5.1	Geometry, orbital energies (ϵ , eV), band widths (W, eV), and intensities ($c^2(C2p)$) for B 1s excited states of BF_3 , BF_4^- , $B(OH)_3$, BO_3 , B_{12} , and BSi_4 from extended Hückel theory.....	125
Table 5.2	Oxygen, boron and carrier concentrations in as-made and annealed Si(B) determined by SIMS and X-ray absorption.....	140

INTRODUCTION

X-ray absorption with synchrotron radiation has been used to investigate two very different materials analysis problems. Extended x-ray absorption fine structure (EXAFS) has been used to study the annealing of $\text{Pd}_{40}\text{Ni}_{40}\text{P}_{20}$ metallic glasses (a collaboration with Dr. R. Brüning and Professor J. Ström-Olsen, Department of Physics, McGill University). X-ray absorption near edge structure (XANES) has been used to investigate the near surface region of boron doped single crystal silicon (a collaboration with Dr. T.E. Jackman, Division of Physics, National Research Council, Ottawa)

Ni K-edge EXAFS results have been obtained for various thermally annealed $\text{Pd}_{40}\text{Ni}_{40}\text{P}_{20}$ metallic glass samples recorded with synchrotron radiation at 77 K and 300 K. Thermal annealing causes changes in their structure known as irreversible and reversible relaxation. The former involves changes that occur when as-prepared glasses are annealed for the first time. The latter involves cycling of the system between states with different properties and different bulk structures by annealing at different temperatures. The samples were prepared and supplied by Ralf Brüning, a recently graduated Ph.D. student of Professor J. Ström-Olsen at McGill University.

Results from a curve fitting analysis of the first coordination shell showed trends in radial distance (R), coordination number (N), and Debye Waller factors. Measuring EXAFS at 77 K should generally give a clearer structural picture than at 300 K. Other than that, one hopes that 77 K and 300 K measured data would show the same trends with annealing history. Since similar trends were not found in all cases, this leads one to believe the fitting procedure is not yet optimized.

The B 1s XANES, obtained via electron yield (EY) detection, was used to study B sites in Si(B) epilayers grown by molecular beam epitaxy (MBE) and in-situ B doping from evaporated B₂O₃. Comparisons of extended Hückel calculations and experimental B 1s spectra of various model compounds (BF₃, KBF₄, B₂O₃, B(OH)₃, elemental boron) have been used to show that B 1s near edge spectra are very sensitive to the local boron environment, and are particularly useful for distinguishing trigonal from non-trigonal environments.

The samples, prepared by the MBE group at NRC, were grown at temperatures of 680°C or 700°C followed by annealing at 900°C. Both as-prepared and annealed samples were measured. The B 1s spectra of all samples show a characteristic spike before annealing, which is interpreted as evidence for boron complexed with oxygen in a trigonal environment in the surface region sampled. After annealing of the most concentrated Si(B) sample studied ($[B]=3 \times 10^{20}$ at.cm⁻³), the surface boron environment changed dramatically to one in which boron is in a non-trigonal environment. In a lower concentration sample ($[B]=8 \times 10^{19}$ at. cm⁻³), this

change did not occur, and the B 1s spectra before and after annealing were practically the same in each case, with evidence of boron trigonally coordinated with oxygen.

Comparisons between the XANES results and those of SIMS/eCV on the same samples show that the X-ray absorption spectra may be strongly influenced by surface segregation. However they clearly demonstrate how sensitive B 1s spectroscopy is to local chemical environment, illustrating how useful B 1s spectroscopy can be for studies of boron doping of semiconductors.

CHAPTER 1

BASIC PRINCIPLES

1.1 General Introduction

This chapter discusses the following: theory of X-ray absorption, X-ray absorption coefficients, physical origin of extended X-ray absorption fine structure (EXAFS), a mathematical description of EXAFS, and a brief discussion of X-ray absorption near edge structure (XANES). A general review of X-ray absorption spectroscopy is given by Bertin [B70]. The experimental and theoretical aspects of EXAFS are treated in KP88, LC+81, S74, W86. Near edge spectroscopy is treated in KP88, W86.

1.2 Theory of X-ray Absorption

When matter is irradiated with photons of high energy (X-rays), electrons are ejected. In this event, the incident photon is absorbed and its energy is given up in expelling and imparting kinetic energy to an electron of a particular atomic level. The general process is referred to as X-ray absorption (XAS); the process of photo-induced electron ejection is called photoionization, and the ejected electron is called a

photoelectron.

The minimum photon energy that can excite an electron from a given energy level of a specific element is referred to as the absorption edge of the particular atomic level of that element. This thesis is only concerned with the excitation and ionization of inner shell electrons. In this case, each element has as many X-ray absorption edges as it has inner-shell ionization potentials: one K, three L (L_1, L_2, L_3), five M (M_1, M_2, M_3, M_4, M_5), and so on. Let us refer to table 1.1 which correlates X-ray and atomic notation. K, L, M... are the conventional X-ray spectroscopic symbols for principle quantum numbers $n=1, 2, 3, \dots$ respectively. The subscripts (1, 2, 3...) are related to j , the total angular momentum quantum number of the atomic core hole state (arising from a coupling of the spin and orbital angular momenta).

For example, in a $2p^5$ configuration, the orbital angular momentum (l) is 1 and the spin angular momentum (s) is $1/2$. The total angular momentum (j) may have values $j=(l+s), (l+s-1), \dots, |l-s|$. Thus in this particular example, j can have values

Table 1.1 Illustrating the correspondence between X-ray spectroscopic symbols and the respective quantum numbers for the atomic core hole state: principle (n), orbital angular momentum (l), spin (s) and total angular momentum (j).

X-ray symbol	atomic notation			
	n	l	s	j
K	1	0	$1/2$	$1/2$
L_1	2	0	$1/2$	$1/2$
L_2	2	1	$1/2$	$1/2$
L_3	2	1	$1/2$	$3/2$
M_1	3	0	$1/2$	$1/2$
M_2	3	1	$1/2$	$1/2$
M_3	3	1	$1/2$	$3/2$
M_4	3	2	$1/2$	$3/2$
M_5	3	2	$1/2$	$5/2$
.	.	.	"	.
.	.	.	"	.
etc.	etc.	etc.	etc.	etc.

of $3/2$ or $1/2$. Therefore, L_2 and L_3 in X-ray notation refer to the $2p_{1/2}$ and $2p_{3/2}$ states of the $2p^{-1}$ configuration. The X-ray and atomic notations are used interchangeably throughout this thesis.

At photon energies very much greater than that of a $1s$ core level, more than enough energy exists in order to expel $1s$ electrons. The probability of ejecting $1s$ electrons decreases as the energy becomes progressively greater, and a decrease in the absorption coefficient (μ_x) is observed.

In general, at energies below the inner shell excitation threshold a decreasing absorption coefficient is observed. At the threshold energy for excitation of a particular atomic energy level, an abrupt increase in the absorption coefficient is observed as shown in figure 1.1. As the energy increases above the edge, μ_x gradually decreases until the photon energy reaches the threshold for excitation of the next more tightly bound electrons where an abrupt increase in μ_x is observed again.

Even though a photon at an energy greater than that of a $1s$ core level possesses more than enough energy to expel a $1s$ electron, in most cases the energy of each photon absorbed is given completely to a single electron. The surplus energy imparts kinetic energy to the photoelectron.

The kinetic energy of a photoelectron is given by the Einstein photoelectric equation

$$E_k = h\nu - IP \quad (1-1)$$

where $h\nu$ is the energy of the X-ray, IP is the energy needed to ionize the core

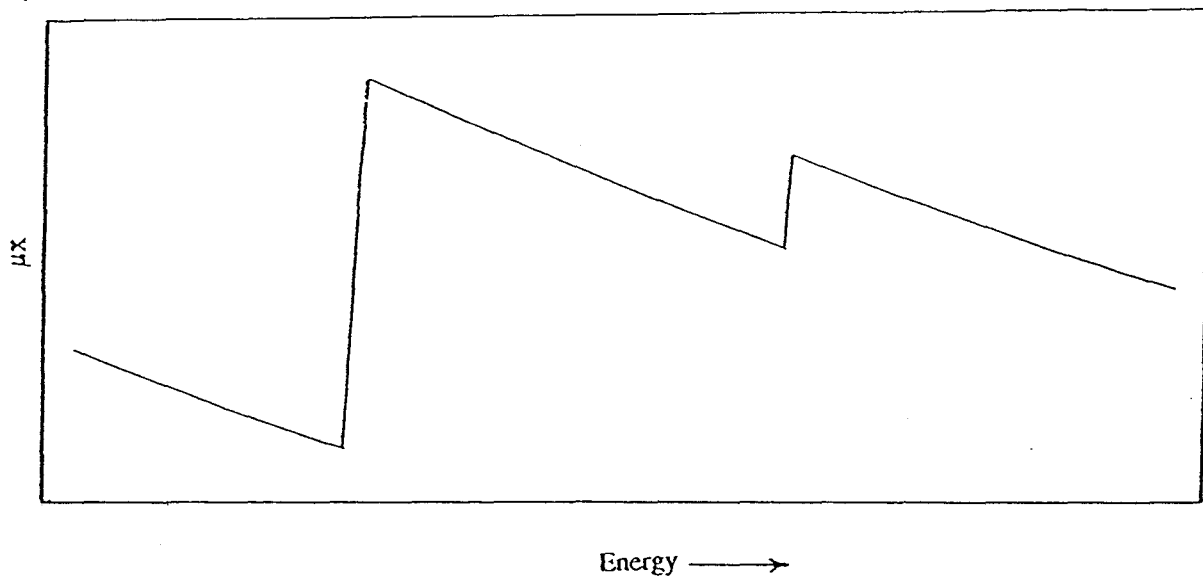


Fig. 1.1 Variation of absorption coefficient in terms of increasing energy.

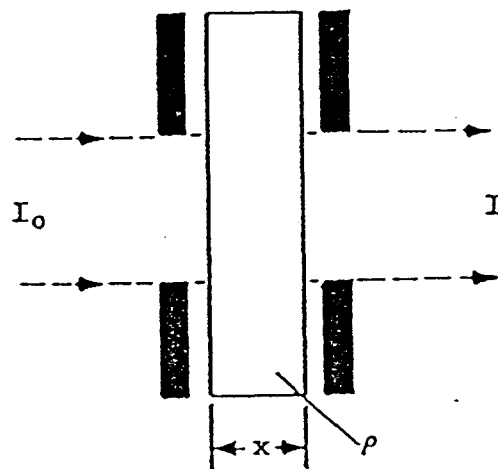


Fig. 1.2 Arrangement for X-ray Absorption. I_0 and I represent the intensities of the incident and emergent X-ray beam, x is the thickness of the sample, and ρ is its density.

electron, and E_k is the kinetic energy of the free electron.

1.3 X-ray Absorption Coefficients

Figure 1.2, illustrates terms relevant to treating X-ray absorption. A monochromatic X-ray beam having intensity I_0 is directed on a material having thickness x (cm) and uniform density ρ (g/cm^3). One may use X-ray opaque masks on both sides of the absorber that are in perfect registry. This shielding is to ensure that the detector (which is generally bigger than the sample) only sees X-rays which pass through the sample.

When an X-ray beam passes through a medium, its intensity is attenuated exponentially according to the Lambert equation,

$$I = I_0 \exp(-\mu x). \quad (1-2)$$

The emergent beam has intensity I , which is less than I_0 , and μ is the linear absorption coefficient in units of reciprocal centimetres (cm^{-1}). The following four X-ray absorption coefficients [B70] can be defined; (a) the linear absorption coefficient μ which gives absorption per unit thickness expressed in the form,

$$\mu = \ln(I_0/I)/x \text{ (cm}^{-1}\text{)}, \quad (1-3)$$

(b) the mass absorption coefficient μ_m which gives absorption per unit mass described by,

$$\mu_m = \mu/\rho \text{ cm}^2/\text{g}, \quad (1-4)$$

(c) the atomic absorption coefficient μ_a which gives absorption per atom by the following,

$$\mu_a = \mu A / \rho N_o = \mu / N \text{ cm}^2/\text{atom} \quad (1-5)$$

and, (d) the molar absorption coefficient which gives absorption per mole given by,

$$\mu_{\text{mol}} = (\mu / \rho) A \text{ cm}^2/\text{mole}. \quad (1-6)$$

The four coefficients are related as follows,

$$\mu = \mu_m \rho = \mu_a \rho (N_o / A) = \mu_{\text{mol}} \rho / A. \quad (1-7)$$

In equations 1-3 to 1-7, ρ is density (g/cm³); A is atomic mass (g/mol); N_o is the Avogadro number (6.02×10^{23} atoms/mole); N is the number of atoms per cubic centimetre; and N_o/A is the number of atoms per gram.

Of the four, the mass-absorption coefficient μ/ρ is the most useful. It is the property of each substance independent of state of physical aggregation. It is a function only of atomic number and wavelength. μ/ρ for a compound, solution, or mixture can be calculated from the values of the constituents (as discussed in chapter 2).

μ and μ_m are total absorption coefficients and are the result of three phenomena; photoelectric absorption, Compton scattering, and pair production. Linear and mass-absorption coefficients can be expressed for each component. In the energy range relevant to this thesis the photoelectric effect dominates.

1.4 EXAFS Theory

X-ray absorption spectra (e.g. fig. 1.3) can be divided into near edge (XANES) and extended fine structure (EXAFS) regions. The nature of bonding around the X-ray absorbing atom can be determined from the near edge structure which will be discussed later. EXAFS is the oscillatory modulation of the absorption coefficient starting somewhat past an absorption edge, as shown by the Ni K edge spectrum of metallic Ni in figure 1.3.

Extended X-ray absorption fine structure (EXAFS) is a powerful way of probing the local atomic structure of all forms of matter, particularly since the availability of synchrotron radiation. The features of EXAFS are the following: (a) it is element selective (b) it is sensitive to short range order in obtaining bond distance, coordination number and chemical identity of nearest neighbours and, (c) it applies to all states of matter in bulk and dilute forms, the latter includes surfaces and adsorbates. The oscillations are due to a final state effect arising from interference between the outgoing photoejected electron wave and the fraction of itself that is backscattered to the X-ray absorption centre from the neighbouring atoms. The net phase of the backscattered wave relative to that of the outgoing electron wave at the central atom determines the nature of this interference.

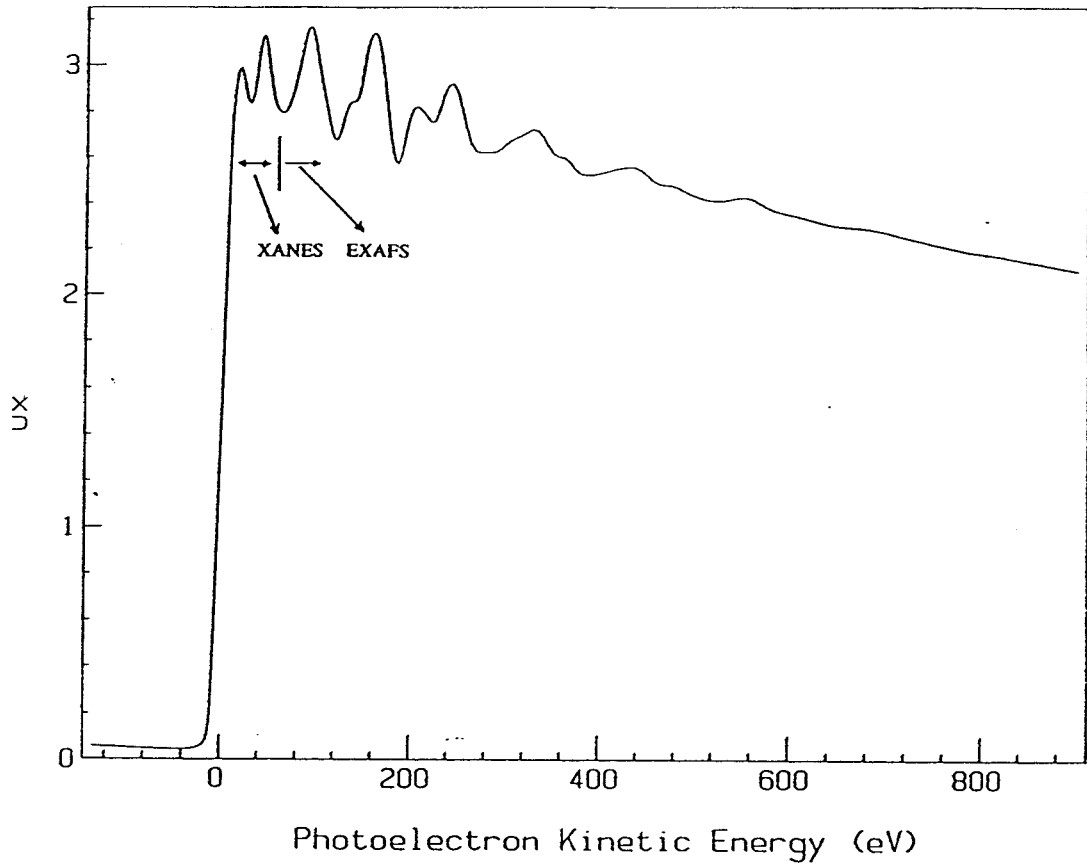


Fig. 1.3 Experimental Ni K X-ray absorption spectrum of polycrystalline nickel metal recorded with synchrotron radiation at 300 K. The zero of the photoelectron kinetic energy scale is the Ni K-edge (ionization potential) at 8326.7 eV.

In order to understand the mechanism of EXAFS in greater detail, let us consider K edge extended fine structure. The probability of X-ray absorption in the dipole approximation [BS59] is given by [W86],

$$P = 4\pi^3 e^2 (\nu c^2 m)^{-1} |M_{fs}|^2 \rho(E_f) \quad (1-8)$$

where $M_{fs} = \langle f | \epsilon \cdot \mathbf{p} | s \rangle$, $|s\rangle$ is the initial (ground) state, $|f\rangle$ is the final (K ionized) state, \mathbf{p} is the momentum operator, ϵ is the electric field vector of the X-ray, $\rho(E_f)$ is the density of states per unit energy at the energy E_f of the final state, and ν is the frequency of the X-ray. $\rho(E_f)$ gives a smooth contribution for X-ray energies well above the edge and can be approximated by that of a free electron of energy $E_{kin} = \hbar^2 k^2 / (2m)$, where k is the photoelectron wave vector described by,

$$k = [2m(E - E_0)]^{1/2} / \hbar \quad (1-9)$$

and E_0 is the zero of the k scale. Assuming $\rho(E_f)$ is smooth at energies above the edge, the only remaining factor that can contribute to the EXAFS signal is M_{fs} (the electric dipole matrix element connecting the initial and final states). The initial state $|s\rangle$ is fixed and doesn't change with ν , however the final state $|f\rangle$ does indeed change with ν and this produces the fine structure. The wave function of the final state photoelectron is a sum of two contributions: the outgoing and backscattered electron wave.

Let's first consider an isolated atom. The excited photoelectron in this case would be in a solely outgoing state from the central atom. This is shown in fig. 1.4a by the outgoing solid rings which indicates no backscattering. In the atomic case, M_{fs}

exhibits no fine structure and the X-ray absorption coefficient would vary smoothly with ν .

Let us now consider an X-ray absorbing atom that is surrounded by other atoms at a fixed distance. In this case the outgoing electron is scattered by the surrounding atoms to produce incoming waves as shown by the dashed lines in fig. 1.4. These incoming or backscattered waves interfere with the outgoing wave in the region of the 1s orbital function. If the relative phases of outgoing and backscattered waves are as in fig 1.4a then there will be a local maximum in the absorption probability. In figure 1.4b, the X-ray energy has been increased to E_2 , leading to a shorter photoelectron wavelength such that the outgoing and backscattered waves are 180° out of phase. In this case there is destructive interference at the absorbing atom A and a local minimum in the absorption probability. Thus the periodic interference in M_{fs} as ν is varied gives rise to the EXAFS oscillations such as those shown in fig. 1.3.

In most cases the outgoing photoelectron is either unscattered or scattered (elastically or inelastically) at an angle other than 180° . Such cases do not lead to modulation of the X-ray absorption probability but rather form a smooth background continuum which is the major portion of the X-ray absorption spectrum as depicted in fig. 1.1.

The extended fine structure is defined as,

$$\chi(k) = [\mu(k) - \mu_0(k)] / \mu_0(k) \quad (1-10)$$

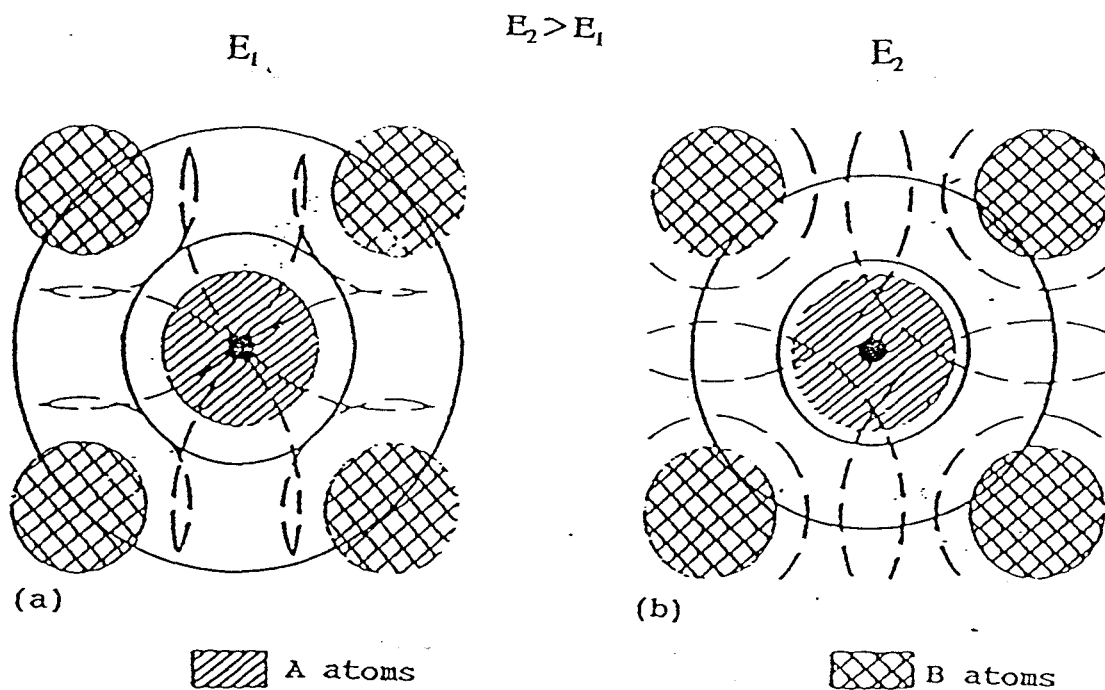


Fig. 1.4 Schematic representation of an EXAFS event. The excited electronic state is centered about the A atom. The full circles represent the crests of the outgoing part of the photoelectron wave. The surrounding B atoms backscatter the outgoing part as shown by the broken circles. Constructive interference is represented in (a) and destructive interference in (b).

where $\mu(k)$ is the total absorption above the absorption edge and $\mu_o(k)$ is the smoothly varying portion of $\mu(k)$, corresponding to the absorption coefficient of the isolated atom [W86] in the EXAFS regime.

1.5 The EXAFS Equation

For an unoriented specimen, $\chi(k)$ above the K or L_1 edge can be described in a plane-wave single scattering formalism as [S74, AD75, LP75],

$$\chi(k) = \sum_j N_j A_j(\pi, k) / k R_j^2 \exp(-2k^2 \sigma_j^2 - 2R_j / \lambda) \sin(2kR_j + \delta_j(k)) \quad (1-11)$$

The summation in eqn. (1-11) is taken over successive coordination shells (j) of atoms surrounding the central atom, with N_j (the coordination number) atoms in shell j located at an average distance R_j from the central atom. σ_j^2 is a Debye-Waller type term and is the mean square relative displacement of the central and backscattering atoms associated with both thermal and structural disorder. λ is the mean free path of the photoelectron, $\delta_j(k)$ is the phase shift experienced by the photoelectron as it travels through the potential of the central and backscattering atoms, $A_j(\pi, k)$ is the backscattering amplitude of the atoms in the jth shell, k is the ejected photoelectron wavenumber.

Two assumptions are made in deriving equation 1-11. The first assumption is that the curvature of the incident wave at the neighbouring atoms is small such that it can be approximated by a plane wave. This approximation is generally reasonable

above $k \approx 4 \text{ \AA}^{-1}$ since above this value the curvature of the wave is small compared to the dimensions of the ionic core responsible for the backscattering (the wavelength is greater than 4 \AA for photoelectrons above 50 eV whereas the ionic core is less than 0.5 \AA). The second assumption is that it considers only single scattering from neighbouring atoms. Single 180° scattering events (fig. 1.5a) dominate EXAFS. Multiple scattering processes (figure 1.5b) can be described by an interference path length which is equal to the sum of the scattering paths. This gives rise to a number of rapidly oscillating terms in k space which tend to cancel each other. Forward scattering (fig. 1.5c), referred to as the focusing effect, is the only case in the EXAFS regime where double scattering is important relative to single scattering. Because of the large probability for elastic forward scattering of electrons [E90] the intervening B atom between the excited A atom and the backscattering C atom effectively focuses the photoelectron wave on both the outgoing and returning paths. This mechanism (illustrated in fig. 1.5c) can introduce detectable enhancement of EXAFS signals from more distant shells. It is only important in this type of collinear geometry and does not affect first shell signals such as those dealt with exclusively in chapter 4 of this thesis.

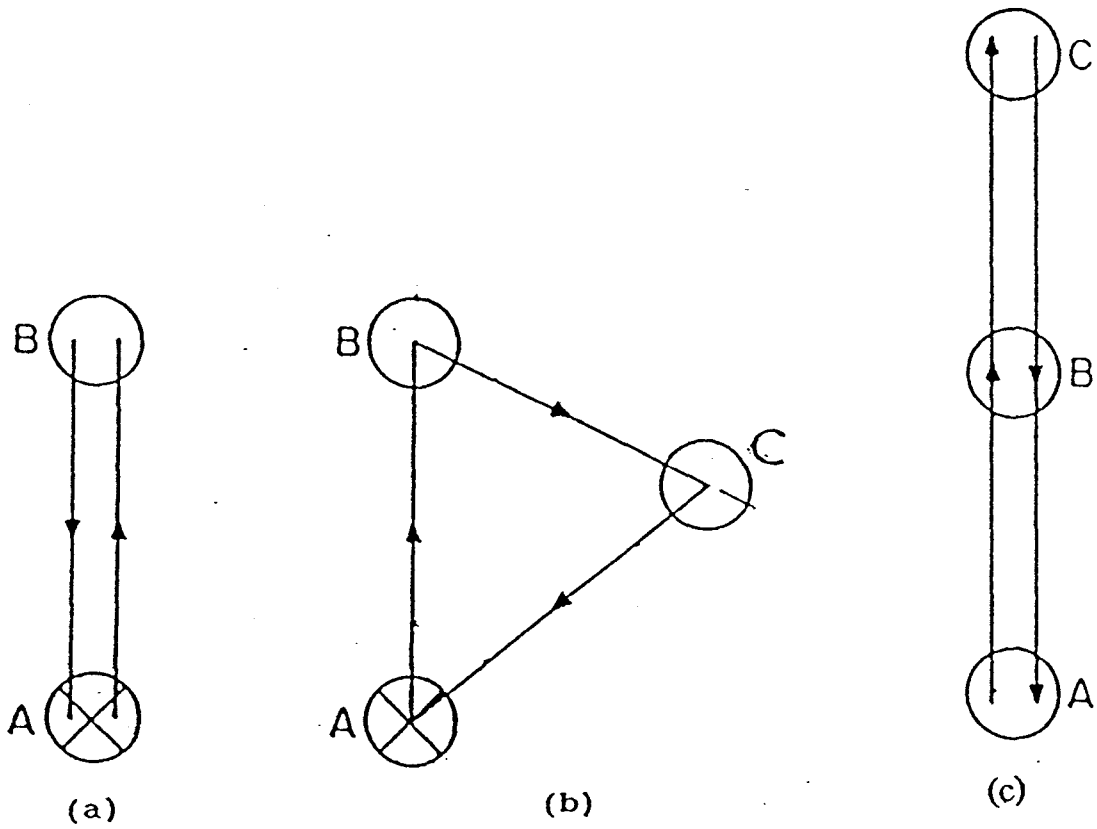


Fig. 1.5 Illustrating (a) a single-scattering path for the photoelectron, (b) a double-scattering path, and (c) forward scattering.

1.6 Theory of XANES

The X-ray absorption near edge structure (XANES) covers the range between the threshold and the part at which the EXAFS commences. Although an exact boundary can not be defined, identifiable XANES (i.e. non EXAFS) features can extend up to 50 eV above the edge (fig. 1.3). Bianconi [B80] suggests that the energy dividing the XANES from the EXAFS region is approximately that at which the wavelength of the excited electron ($1/k$) is equal to the distance between the absorbing atom and its nearest neighbours.

The electronic states of condensed systems that are most easily understood are those of very low and very high energy. Low energy core excited/ionized states are closely related to local electronic structure. The energies and transition probabilities are sensitive to many factors such as the shifting of core level binding energies in different chemical environments [BS83] and the density of unoccupied electronic excited states (or local, unoccupied molecular orbitals in a covalently bonded solid with localised electronic structure). On the other hand, the influence of other atoms in the system becomes quite small at very high energies in the continuum. In this range plane waves that are only weakly scattered by neighbouring atoms adequately describe the photoelectron. Practically all the interest in condensed matter electronic structure theory centres on the low lying extended states, which are the states that bond the atoms together and determine the electronic structure. The whole

apparatus of electronic structure theory [F82] has been assembled to describe these states. The states populated in the XANES region belong to this last category.

Multiple scattering becomes very important at the low photoelectron energies of the XANES region. Multiple scattering of the excited electron is sensitive to all of the details of the spatial arrangement of neighbouring atoms around the absorbing atom, giving information not only about their distances but also about orientation relative to one another, i.e. bond angles, etc. A more detailed discussion of XANES theory can be obtained elsewhere [KP88]. Examples where XANES has been used to extract information can be found from references BKK89, GD+81, GG+82, and MDG82.

Since the XANES region is extremely sensitive to the detailed nature of both the valence and core potentials a first principles calculation such as multiple scattering [DD+79] or molecular orbital theories [OR+80] can give a complete and quantitative understanding of the absorption spectra. What is convenient to have is some practical general rules, with a simple physical meaning, which can provide useful information from a straight forward analysis of the experimental data. One recent approach has been to relate near edge features to specific local bonds.

Experimental [GL81, HB81, SSH84] and theoretical [OR+80] investigations of the K-edge XANES spectra of different diatomic gas phase molecules suggested the existence of a correlation between the energies of certain XANES features and the bond length between the excited atom and its neighbour [GL81, OR+80]. "A theoretical basis of a possible correlation between δ , the energy relative to the K shell

IP, and R, the bond length, is provided by multiple-scattering theory [DD+79]. In this picture XANES features are described as resonances or quasi-bound excitations arising from a resonant scattering process of the excited photoelectron in the intramolecular potential" [SG+89]. For this reason the excitation energy of a shape resonance (a broad feature obtained from the promotion of an electron to a quasibound state above the ionization limit) is expected to be sensitive to the distance between the excited atom and its neighbour(s). In fact, an EXAFS-like rule, $k_r R = \text{constant}$, has been proposed [N83] between R and the photoelectron momentum k_r at the shape resonance, where k is defined relative to the mean intramolecular potential V_o . The practical usefulness of this relation is however severely impeded by the lack of knowledge of V_o , the energy dependent phase shifts in the XANES region, and the dependence of V_o and the phase shifts on Z.

A large number of K edge spectra of small molecules have been used [SSH84] to show that a simple relationship does indeed exist which links the position of the shape resonance to the bond length. Other examples can be found elsewhere [BF+85, BM+89, L89, WL+84].

As was briefly mentioned above, an alternative method for describing near edge features is via molecular orbital calculations. In these calculations the final state is not the scattering path, but empty molecular orbitals. One of these types of calculation (Extended Hückel Molecular Orbital Theory) was used in this thesis to help describe the local electronic structure for boron doped in silicon. A more detailed

discussion of this calculation is given in chapter 5.

Both of the above approaches treat only one electron excitations. In the one electron approximation only one core electron interacts with the incoming photon and all the other electrons are passive i.e. they are described with an orbital configuration which is the same in both the ground and excited state. The orbitals can be either those of the ground state (initial state frozen configuration) or those of the excited state (final state frozen configuration or fully relaxed configuration). Often a one electron theory provides good approximations to experimental data but in reality multi-electron transitions do occur. In multiple photoionization processes two or more electrons are excited by a single photon. Multiple ionization processes can be described in terms of the rearrangement of passive electrons in which the electrons adjust rapidly from the initial states to the final states [W83, Y87]. Following interaction with radiation and inner shell ionization the electrons of the atom may find themselves in various states of excitation. When this involves double excitation (promotion of a core and valence electron to a bound orbital), this produces an absorption peak in the XANES region. When the multi-electron process involves an electron excitation to a bound state plus electron ionization, this is referred to as shake-up and forms a continuum in the XANES region. Double ionization, referred to as shake-off, can also occur. The latter two multi-electron processes produce a broad continuum contribution. In a multi-electron description of the initial and final states, the shake-up peaks arise because of mixing of multi-electron configurations in

the final states. Cases where multiple electron transitions are found to give identifiable structure have been identified in both low energy [HB80] and high energy [BM+89, S82] inner shell near edge spectroscopy.

CHAPTER 2

EXPERIMENTAL

2.1 General Introduction

This chapter is concerned with the experimental aspects of X-ray absorption spectroscopy as measured using synchrotron radiation. It discusses the usefulness of synchrotron radiation as a source for spectroscopy, the synchrotron radiation sources and detection techniques used to acquire data. In addition the technique used to prepare powder samples (e.g. reference compounds) with appropriate thickness and sample preparations for the metallic glass and boron doped silicon are outlined. The author acknowledges, Dr. Ralf Brüning from McGill University, Dr. T.E. Jackman from NRC, and Drs. Tolek Tyliczszak, Philippe Aebi, A.P. Hitchcock all from McMaster University, who have helped make various measurements. In addition, the author acknowledges the people responsible for each of the beam lines for their help and use of the lines; Dr. T. Elam (NIST-X23B), Dr. C.E. Bouldin (NRL-X23A2), Dr. G.M. Lambie, J. Scrofani (NSLS-X11A), Dr. K.H. Tan, Dr. J.D. Bozek, Dr. Jin-Ming Chen (CSRF-grasshopper) and the CHESS staff scientists.

2.2 Synchrotron Radiation

Synchrotron radiation (SR) is electromagnetic radiation emitted by charged particles that move at relativistic velocities. The spectrum emitted extends from the infrared and visible through the vacuum ultraviolet soft X-ray range far into the X-ray range proper. The properties that make synchrotron radiation a very useful source for spectroscopy at photon energies above the visible are the following [K79]: (a) continuous high intensity, high brightness spectrum from the infrared to the X-ray region, (b) collimation of the emitted radiation in the instantaneous direction of flight of the emitting particles, (c) linear polarization with electric field vector parallel to the plane of the orbit, (d) circular polarization above and below the plane of the orbit, (e) time structure and pulse length down to 100 ps, (f) absolute calculability of all properties of the source, and (g) cleanliness of the source.

The synchrotron radiation (SR) sources that were used in this research were: (1) National Synchrotron Light Source (NSLS) at the Brookhaven National Laboratory (BNL) in Upton, New York (April 1989), (2) Synchrotron Radiation Centre (SRC) located at the University of Wisconsin at Madison, in Stoughton Wisconsin (November 1989), and (3) Cornell High Energy Synchrotron Source (CHESS), located at Cornell University in Ithaca, New York (February 1990). The people who have helped make the measurements at the various facilities were: (1) Ralf Brüning, Dr. T. Tyliczszak, Dr. A.P. Hitchcock, (2) Dr. T.E. Jackman, Dr. T. Tyliczszak, Dr.

A.P. Hitchcock, and (3) Dr. Philippe Aebi, Dr. T. Tyliczszak. Runs at NSLS and CHESS require many people since the X-ray beam at both facilities runs 24 hours per day/seven days a week. Table 2.1 lists some of the properties of the above three SR facilities. Figure 2.1 which shows the flux available at NSLS and SRC (before monochromation) illustrates the wide energy range, high intensity and unstructured spectral shape all important aspects of SR.

A wide range of sample types (powders, liquids, solids) and detection techniques such as transmitted flux, and yield techniques (electron (total, partial), fluorescence, ion, luminescence, etc.) can be used in XAS. Several X-ray ranges (hard (7 keV-16 keV), soft (0.1-0.6 keV)) and experimental techniques (transmission, electron yield, sample current) were used as appropriate to the experiments carried out for this thesis. These techniques are discussed separately below.

2.3 Transmission Technique

The Ni 1s and Pd 1s spectra for a number of $\text{Pd}_{40}\text{Ni}_{40}\text{P}_{20}$, metallic glass samples were acquired with transmission mode detection at the National Synchrotron

Table 2.1 Synchrotron ring diameter (RD), energy (E), initial current (i), and lifetime (τ) for CHESS, NSLS, and SRC.

	<u>RD (m)</u>	<u>E (GeV)</u>	<u>i (mA)</u>	<u>τ (h) @-mA</u>
<u>CHESS</u>	500	5.44	80	4 h @ 80 mA
<u>NSLS</u>	140	2.50	250	> 10 h @ 100 mA
<u>SRC</u>	20	0.80	200	3.9 h @ 100 mA

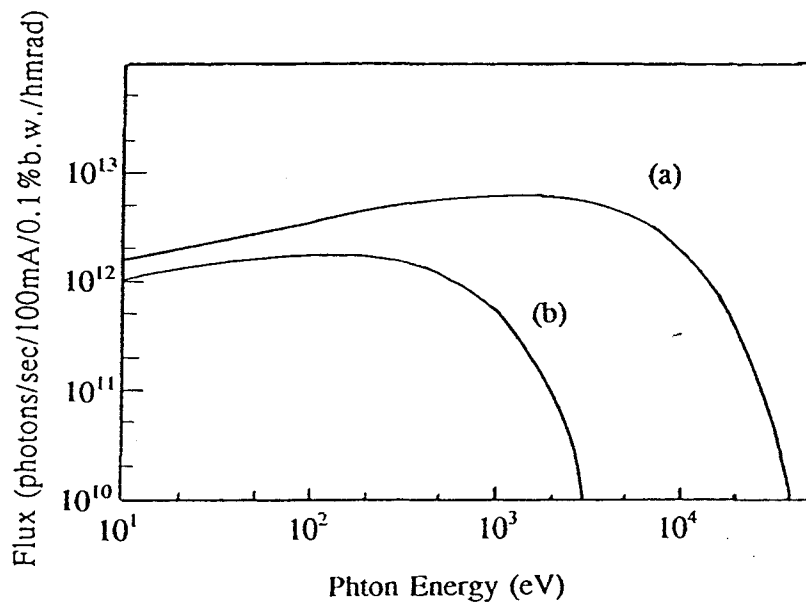


Fig. 2.1 Spectral distribution of synchrotron radiation from bending magnets (BM); (a) NSLS X-ray BM, (b) SRC (Aladdin) VUV BM.

Light Source (NSLS), at the Brookhaven National Laboratory (BNL) in Upton, New York, on the X23B, X23A2, and X11A beam lines. Figure 2.2 shows the NSLS floor plan to give an idea of the size of this facility and indicate the location of these beam lines.

The normal transmission mode, shown schematically in figure 2.3, requires two ion chambers (I_0, I_1) with the sample placed in between. One can also provide another detector, I_2 , so that the spectrum of a reference material may be collected in parallel for every sample (this was not done in the present work).

A number of variables relating to the monochromator may be adjusted by the user in a typical experiment. The spacing of the incident beam slits may be adjusted both vertically and horizontally since the resolving power of the device depends on the vertical adjustment and it is important to mask the sample with the horizontal slit (see fig 1.2). Furthermore, the position of the incident beam slits may be adjusted from outside the monochromator enclosure so that they may be scanned vertically to align their position to that of the X-ray beam. When present, mirrors can be adjusted so as to direct the most intense part of the beam toward the first monochromator crystal.

A double crystal monochromator was used in the transmission experiment. In these devices the first crystal accepts the full flux of the X-ray beam and rotates about a line. The second crystal rotates and translates simultaneously, always parallel to the first crystal.

Gas ionization detectors [K86, RS49, W50] were used to detect both the incident (I_0) and transmitted (I_1) X-ray flux. When X-rays traverse the gas (e.g. N_2 ,

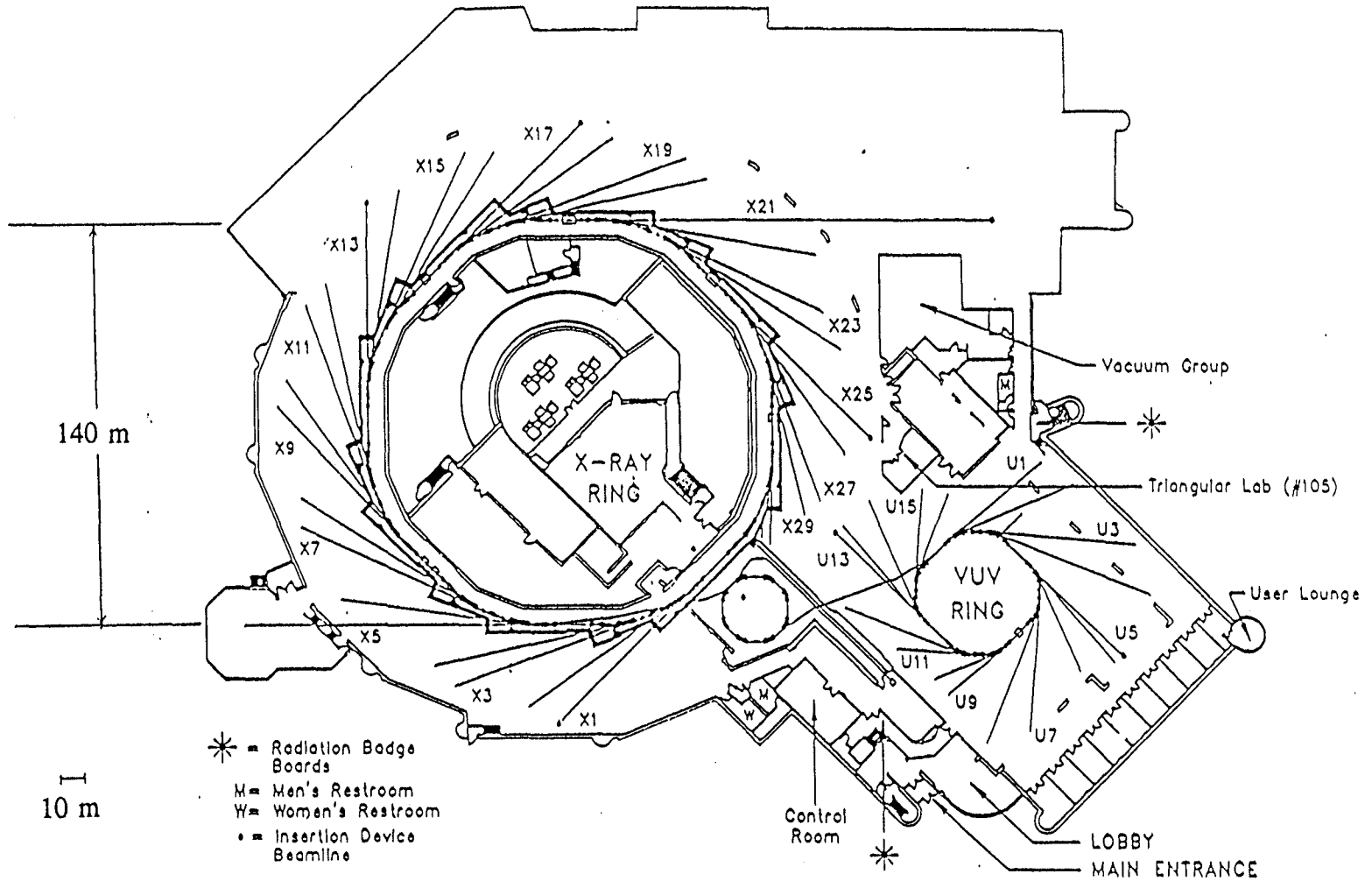


Fig. 2.2 Floor plan of the National Synchrotron Light Source experimental area.

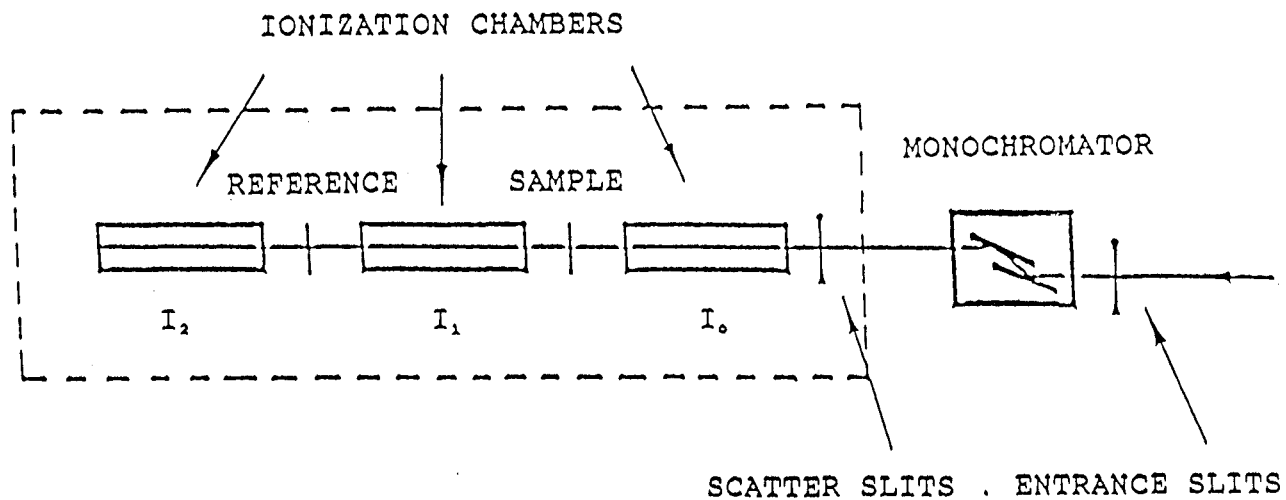


Fig. 2.3 Schematic of the transmission XAS experiment. The dashed line shows the radiation safety enclosure, "the hutch".

Ar) in an ion chamber a portion is absorbed. The photoelectrons produced further ionize the gas. A voltage applied across the detector separates the positive ions and electrons so that they can be collected before they recombine. The X-ray induced current in the detector is measured with an appropriate interface to the data acquisition computer, typically consisting of a current-to-voltage converter (CVC), a voltage-to-frequency converter (VFC) and a counter. The hardware, computer and software were supplied by the beamline in all cases.

Figure 2.4 shows a schematic of the typical electronics used for transmission mode XAS. The ion chambers are run in the plateau region with an applied bias voltage of approximately -200 VDC. The current collected from the gas chambers (I_1, I_0), is then amplified via a Kiethley current amplifier, where it is converted to a voltage (CVC). A voltage-to-frequency converter (VFC) may then be used. The advantage of a VFC is that data is accumulated during the whole measuring time and not only at one time as is the case with an analog-to-digital converter (ADC). In addition, the VFC has a resolution of 10^6 counts per 10V and not 10^3 - 10^4 as for an ADC. The output of the VFC is fed into a scaler for visual display and to up/down counters in the CAMAC. The counts displayed in the scalers are not photons/s but are simply proportional to the photon flux absorbed in the ionization chamber.

Finally, the data is stored on a computer which is interfaced to the CAMAC electronics, and may be plotted. The data is transferred back to McMaster University on floppy diskettes.

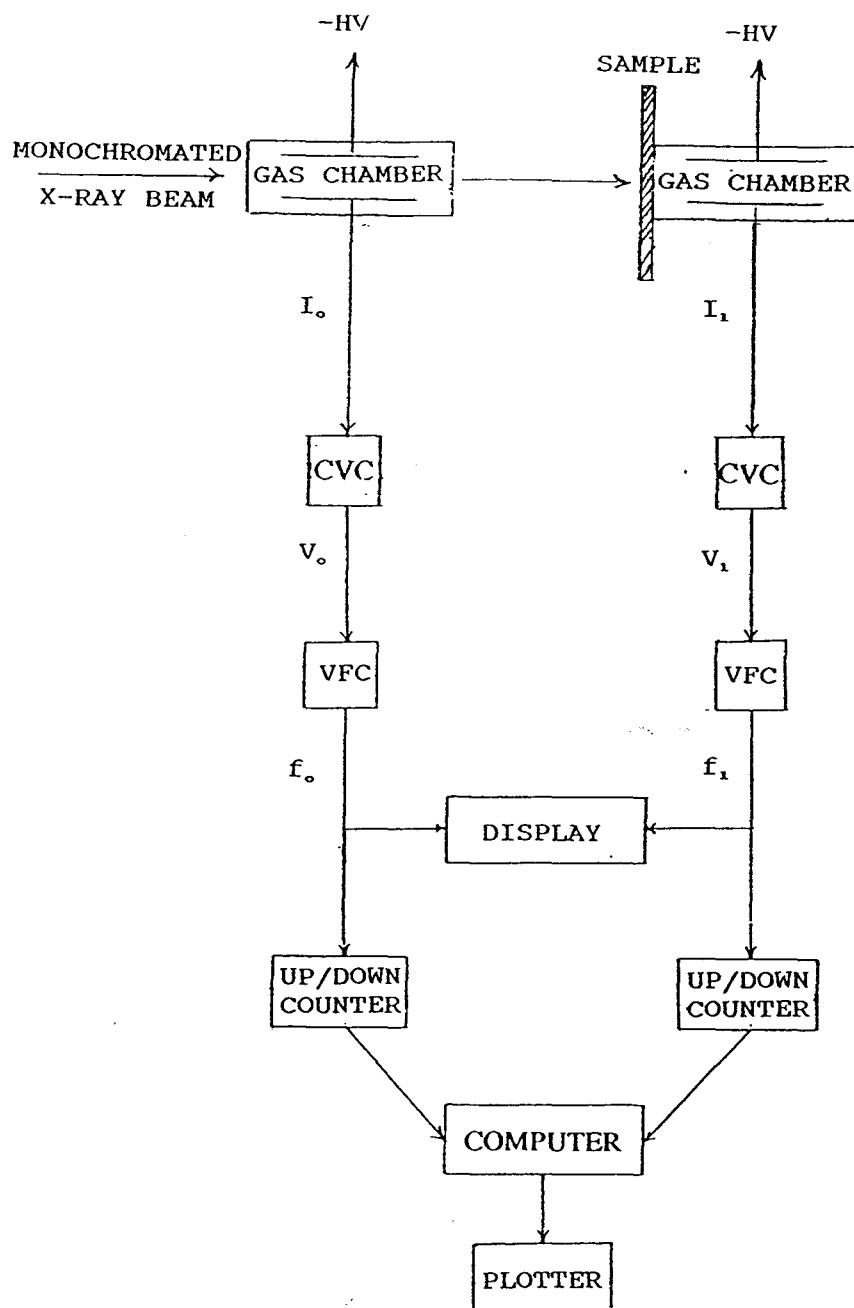


Fig. 2.4 Schematic of the typical electronics used for transmission mode XAS. CVC, VFC represent current to voltage and voltage to frequency converters respectively.

It is advantageous to have one's own on-site PC and data analysis program such as the one called BAN (developed by Dr. Tolek Tyliczszak at McMaster University) which is designed especially for EXAFS analysis. Your own PC allows near simultaneous data analysis which may guide proper decisions (regarding sample changes, instrumental checks, etc.) during the course of the experiment. Since the availability of beam time at synchrotron facilities is very limited, it is desirable to optimize the efficiency of data collection at all times.

2.4 Electron Yield Technique

(a) Electron Yield

Electron yield (EY) detection has been used in surface EXAFS and XANES experiments, usually in high vacua, where surface sensitivity is required [L89]. The transmission technique was not used for the boron doped silicon samples simply because they were too thick. One needs a thickness of approximately 100 Å for transmission measurements in the boron 1s spectral region (200 eV). Section 2.5a describes the appropriate formulae and techniques used to prepare samples with optimum thickness for transmission XAS.

Figure 2.5 A i,ii, and B i,ii, show a comparison in both energy and wavenumber (k) space between the Ni K edge EXAFS of the "as made" amorphous $\text{Pd}_{40}\text{Ni}_{40}\text{P}_{20}$ metallic glass at 300 K, recorded by transmission and electron yield. The curves in fig. 2.5 B have been plotted on the same scale. The similarities of electron

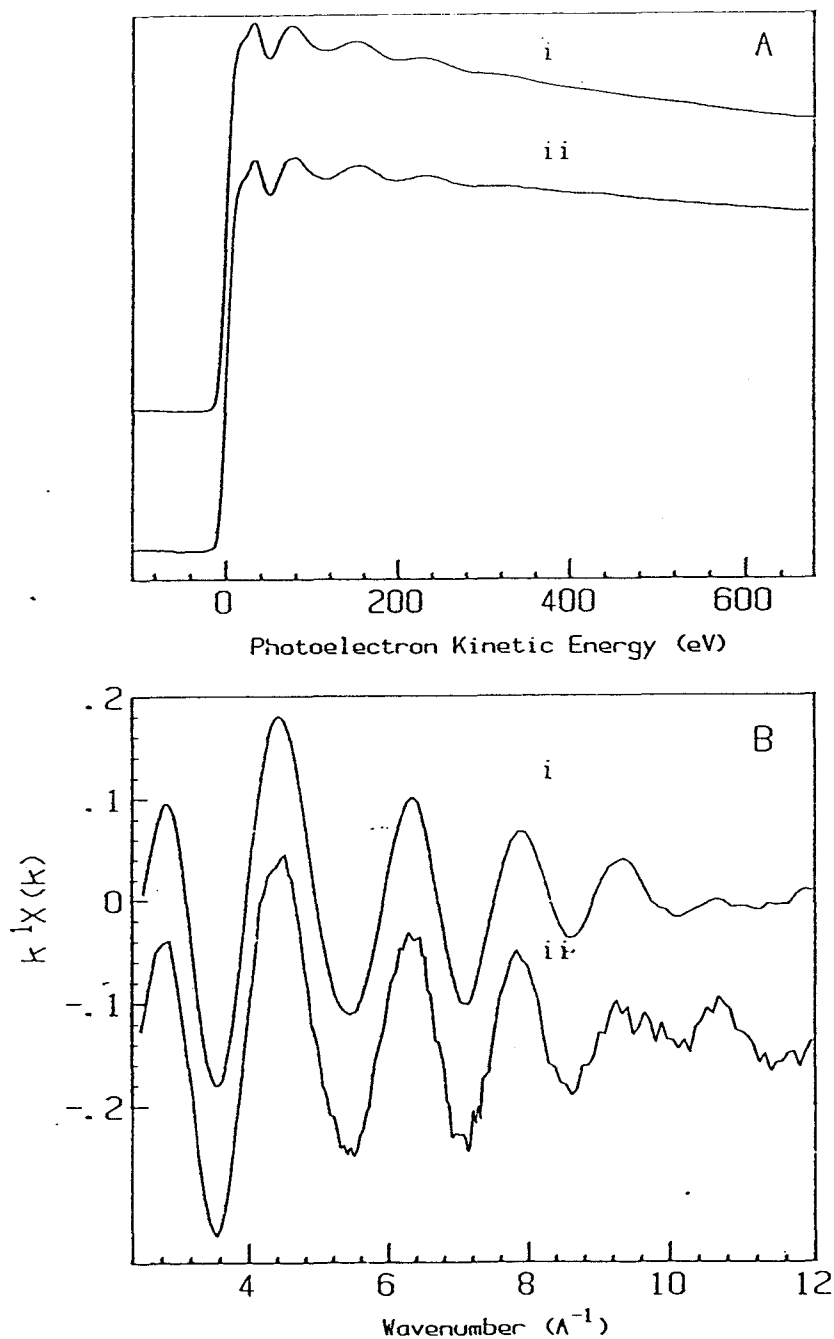


Fig. 2.5 The Ni-K edge EXAFS of the "as made" sample of amorphous $\text{Ni}_{40}\text{Pd}_{40}\text{P}_{20}$. (A) X-ray absorption (i) and electron yield (ii) spectra as a function of photon energy, and (B) $k^2\chi(k)$ spectra for (i) XAS and (ii) EY shown on the same scale after background subtraction.

yield and the transmission spectra (in shape, amplitude and statistical precision), both in energy space and normalized k-space (see chapter 3 for details on data processing), illustrates that total electron yield gives a true representation of the absorption coefficient in this case. This is generally true at higher energies where the escape depth of electrons is much higher than at energies below 1 keV and thus electron yield detection is essentially a bulk sensitive technique.

Among the many advantages of the EY technique are; (a) it is surface sensitive (although the degree depends on the material and photon energy), (b) it has higher signal levels than fluorescence due to the high efficiency of producing electrons and the gain that occurs during propagation in both the sample and in the ionization chamber (although this does depend on factors such as the energy level, specimen, etc.) (c) minimum sample preparation is required. The sample must be at least semiconducting and electrically connected to the detector. Otherwise a charge will build up and break down intermittently producing noise in the data, (d) thickness effects are avoided (since the incident X-ray penetration into the sample is always much greater than the electron escape depth, the sample is always effectively "thin"), (e) rapid sample change.

Some of the disadvantages are, (a) the high surface sensitivity (particularly with low photon energies) means that other species on the surface may be detected in addition to the species under study, which in fact may influence true spectral results of the latter, (b) the detailed physics is not known (sampling depth and energy distribution of electrons detected).

(b) B 1s Detection

The B 1s spectra were acquired with electron yield (sample current) detection at the Canadian grasshopper beam line [TB+82, BTB87] of the Synchrotron Radiation Facility (SRF) in Stoughton, Wisconsin. The pressure of the system was 3×10^{-8} torr and the samples were at ambient temperature (300K) during measurements.

Electron yield detection is well suited for hard X-ray studies of dopants in semiconductors [EW+88, TH89, THJ90] since the electron yield EXAFS depth sensitivity is well matched to typical dopant distributions and thicknesses of MBE grown layers. However the technique is less well suited for B 1s spectroscopy due to the very shallow depth sensitivity in this soft X-ray range. Fluorescence detection would have been preferable for this study since it is a deeper probe, but this requires a thin window X-ray detector which was not available for these measurements.

Two techniques were used to measure the electron yield (see figure 2.6 for a schematic of electron yield detection). The first involved using a channeltron to detect electrons ejected from the sample as an amplified current. The second technique involved measuring the current at the sample. Sample current detection was used for most measurements since the statistical precision was somewhat better. The two techniques measure complementary aspects of the same physical process and thus should provide equivalent information although the acceptance angle of the channeltron is smaller than the 2π sr effective 'acceptance angle' of sample current detection.

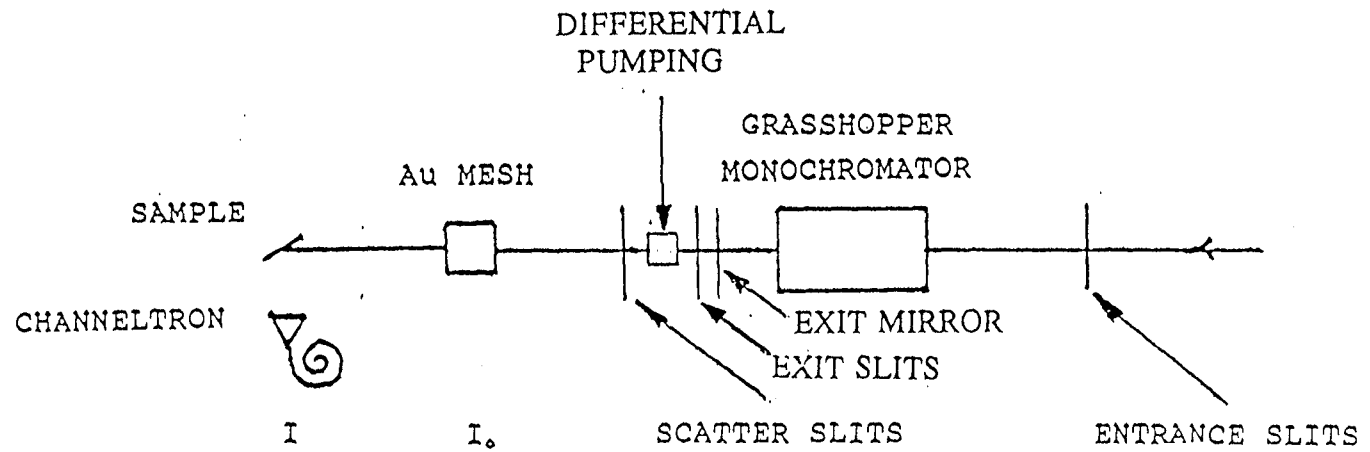


Fig. 2.6 Schematic illustration of a typical EY experiment. The entire system is under vacuum.

Simultaneously with each electron yield or sample current measurement, the incident photon flux (I_0) of the CSRF grasshopper beam line was measured as the current at a Au mesh located upstream of the sample. However, this signal was not appropriate for the Si(B) study since it contained artifacts. Figure 2.7 shows the incident flux as a function of photon energy. Note the large signal from the presence of carbon K-edge absorption in first order at 284 eV and second order at 140-150eV. In addition an artifact is observed at 195 eV, which is likely due to boron contamination on the gold mesh. This is better illustrated by a background subtracted 10 fold expansion as shown.

2.5 Sample Preparations

(a) Transmission

A good transmission XAS sample must be uniform and of correct thickness. Metallic samples can often be rolled, evaporated or sputtered to the desired thickness.

The goal for sample preparation is to choose the sample thickness and concentration for an attenuation $[1-I/I_0]$ between 30% (optimum for no self-absorption distortion) and 80% (optimum for statistical precision). Thus, one would like μx in the range of 0.3 to 1.6 just above the core edge of interest i.e. 0.3 for near edge studies (this minimizes distortions of strong peaks such as the so called "white lines" [S88a]), and 1.6 for EXAFS. For powder samples one may work in terms of desired thickness x , but the density (ρ) must be known. Therefore it is better to work with

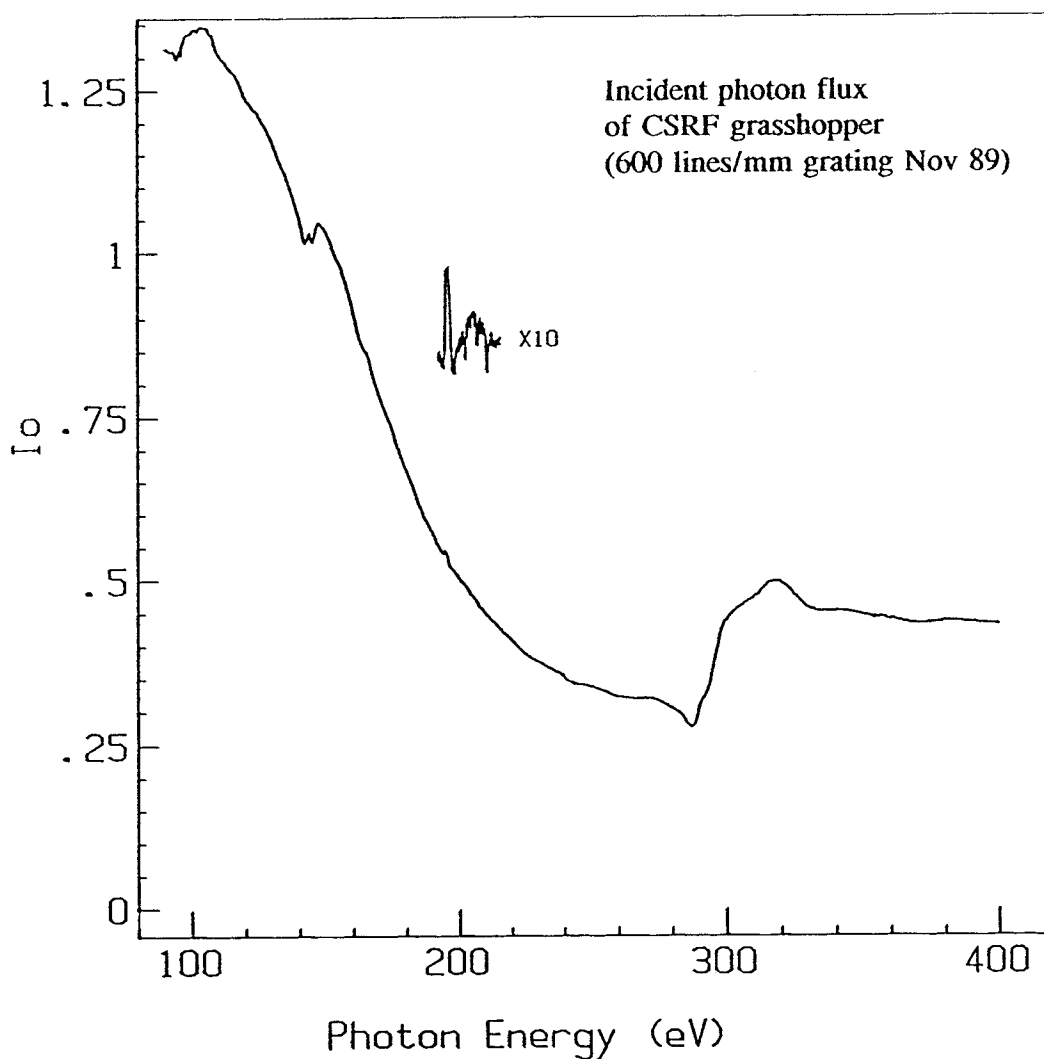


Fig. 2.7 Incident photon flux (I_0) spectrum from CSRF grasshopper monochromator at SRC. The signals at 284 eV and 140-150 eV are due to C K-edge absorption in first and second order respectively. The signal at 195 eV is perhaps due to boron contamination on the gold mesh.

mass. An example of the type of calculation used to determine the mass of a powder sample is given below.

For a given illuminated area A (or area packed with sample, which should be somewhat larger than the beam size of 15-20 mm by 1 mm) the mass of a sample required is then given by,

$$M = \frac{A}{\sum_i g_i (\mu/\rho)_i} \cdot (\mu x)^{\text{opt}} \quad (2-1)$$

where A = area of sample

g_i = mass fraction of atom type i

$(\mu x)^{\text{opt}}$ = optimum absorbance (0.1-1.6)

$(\mu/\rho)_i$ = mass absorption coefficient of atom type i just above the edge of interest

One may obtain $(\mu/\rho)_i$ from the Victoreen formula $\lambda^3(C-D\lambda)$ where C and D are constants and λ is the wavelength [RM62].

If the calculated mass is too small to fill the area needed, and the sample is a powder, one may dilute the sample with a low Z material i.e. Li_2CO_3 , sugar, etc. It is important to grind powders to a small size to avoid absorption saturation effects [S88a]. If appropriate (e.g. molecular complexes), solution spectra are preferable.

For metals one may obtain the thickness from,

$$x(\text{cm}) = [(\mu/\rho)(\rho)]^{-1} \cdot (\mu x)^{\text{opt}}.$$

For pure metal foils a useful rule-of-thumb is that one absorption length corresponds to a foil x μm thick for an edge at x keV.

(b) Pd₄₀Ni₄₀P₂₀ Metallic Glass Samples

The Pd₄₀Ni₄₀P₂₀ metallic glass samples were supplied and prepared by Ralf Brüning, a recently graduated Ph.D physicist in the group of Professor J.O. Ström-Olsen at McGill University.

The main method for making metallic glasses is the melt-spinning of a molten alloy [CT80]. Briefly, a jet of molten metal is driven onto the surface of a rapidly rotating metal disk or cylinder, which is held at or below room temperature. The liquid is then drawn into a film no thicker than a few ten thousandths of an inch. The metal cools and solidifies extremely quickly (the metal can be cooled by 1000K in a millisecond i.e. one million degrees per second) because the film is so thin, it is in contact with a heat sink of comparatively large volume, and because metals have an inherently high thermal conductivity.

The Pd-Ni-P metallic glass was prepared using the melt spinning method outlined above. Briefly a 2-3 g ingot prepared from metallic Pd and Ni₂P was melted in a quartz crucible and spun through a 0.8 mm orifice onto a Cu wheel. The wheel speed was approximately 10m/s on the surface. All samples were taken from the same ribbon.

In principle, the as-prepared samples were somewhat too thick for EXAFS measurements, and thus some thinning of the samples was desirable. However, this was not done to avoid any structural modification during thinning. The good agreement between transmission and EY spectra (fig. 2.5) indicated there is negligible distortion due to absorption saturation.

(c) Si(B) Semiconductor

The boron doped silicon samples were supplied by T.E. Jackman and prepared by M. Denhoff at the Division of Physics of the National Research Council (Ottawa). The growth procedures and molecular beam epitaxy facility have been described elsewhere [JH+88]. Briefly, the epilayers were grown on standard, 100-mm-diam Czochralski wafers in a Vacuum Generators V80 Silicon MBE facility. The boron doping was carried out by co-evaporation of B_2O_3 from a shuttered evaporation cell. The samples were extensively characterised by techniques at NRC other than XAS. SIMS spectra were recorded with a Cameca IMS 4f ion microprobe and the secondary ion yields were calibrated using ion-implanted reference standards. Carrier concentrations were measured with a Polaron PN4200 eCV profiler. Post-growth annealing was carried out on some pieces in a standard UHV furnace to remove oxygen from the epilayers. The sample characteristics are summarised in table 5.2, chapter 5.

Because of the extreme surface sensitivity of the electron yield detection technique, the samples were chemically cleaned by etching with concentrated HF acid to remove the native oxide, rinsed in deionized water, and dried with N_2 gas blowing just prior to insertion into the measurement chamber via a load-lock.

CHAPTER 3

EXAFS Data Analysis

3.1 General Introduction

This chapter is concerned with the analysis of the EXAFS component of X-ray absorption spectra. Reviews of the theory and procedures of EXAFS analysis can be found in references [KP88, LC+81, MK+69, TL79]. All software used in the EXAFS analysis was written by Dr. Tolek Tyliczszak at McMaster University. Extraction of EXAFS and single component (ratio method) analysis were performed using the program called BAN. This program provides a wide variety of features for data analysis. All curve fitting was performed using the program MFIT. The general aspects and procedures of curve fitting are discussed in section 3.4. The details of how MFIT was applied to the analysis of the $\text{Pd}_{40}\text{Ni}_{40}\text{P}_{20}$ metallic glass samples are discussed in chapter 4.

3.2 Extraction of EXAFS and Fourier Analysis

(a) EXAFS Extraction

A standardized procedure has been used [LSS75, LC+81] to extract the EXAFS signal $\chi(k)$ from the experimental X-ray absorption spectra. Let us use the Ni K-edge spectrum of nickel metal as an example to illustrate the steps performed systematically for the analysis of all amorphous samples of the Pd₄₀Ni₄₀P₂₀ metallic glass.

The E_0 of the X-ray absorption spectrum was selected as the principle maximum of the derivative spectrum. Figure 3.1a i,ii shows the Ni-K edge X-ray absorption spectrum of nickel metal and its corresponding derivative spectrum, the latter displayed only in the range -52 to 56 eV with respect to the edge. The value obtained from the principle maximum was then used to establish the zero of the photoelectron energy (fig. 3.1b) and EXAFS wavenumber (fig. 3.1c) scales.

This spectrum was then truncated in the approximate range of 25 to 680 eV (illustrated by the dashed vertical lines in fig. 3.1b). The first point of truncation was chosen as the next peak above the principle maximum in the derivative spectrum. Next, the photoelectron energy scale was then converted to k-space using eqn. 1-9. At the same step the data was multiplied by k^1 to yield the curve as shown in fig. 3.1c. k^n is a weighting which can be used to compensate for amplitude reduction as a function of k [LSS75]. Values for n suggested by Teo and Lee [TL79] for

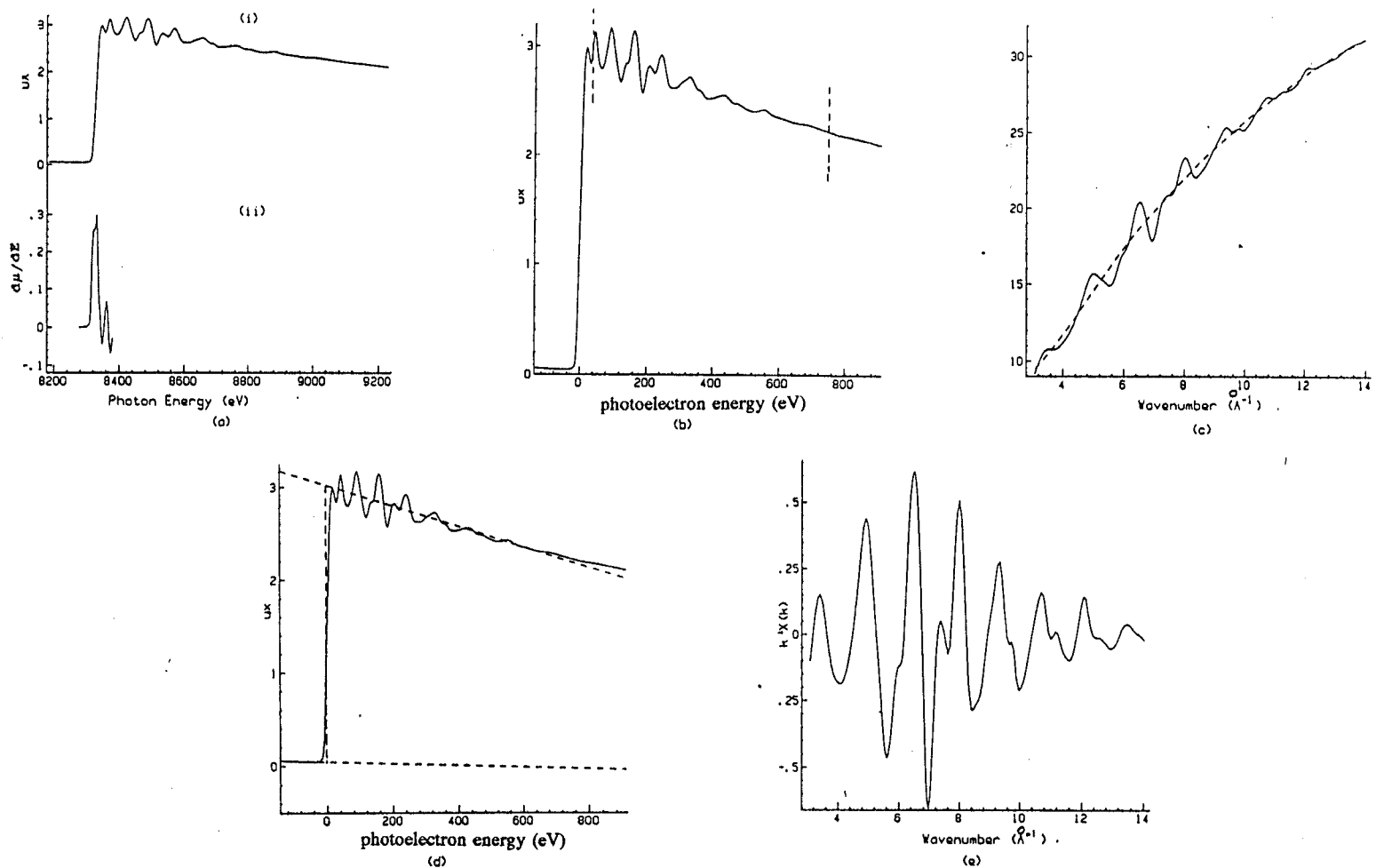


Fig. 3.1 The steps performed for EXAFS extraction; (a) the Ni K-edge X-ray absorption spectrum of nickel metal in (i), and the corresponding derivative spectrum taken in the range -52 to 56 eV (ii). The value of the principle maximum was used as E_0 . (b) spectrum on a photoelectron energy scale and the dashed lines represent the range (25-680 eV) of truncation; (c) the $k^1\chi(k)$ spectrum illustrating a 3 section, cubic spline, background subtraction by the dashed line; (d) illustrating the calculation of the difference in slopes between the pre and post edge using a least squares fit (used for improved amplitude normalisation); (e) the normalized $k^1\chi(k)$ spectrum of nickel metal.

backscatterers $Z > 57$, $36 < Z < 57$, and $Z < 36$ are 1, 2, and 3 respectively. For example, for the Ni K edge EXAFS of the Pd-Ni-P system, one may use k^3 , k^2 , and k^1 for the P, Ni, and Pd backscatterers respectively if those shells were sufficiently distinct. k^1 was systematically chosen in all cases for analysis of the Ni K-edge of the metallic glass since this allows a less biased view of amplitude shapes which is useful for semiquantitative identification of the Z of an unknown backscatterer (from comparison of McKale amplitudes in the last step of the processing procedure).

The EXAFS $k^1\chi(k)$ was then obtained by subtracting the post edge background function $\mu_o(k)$ [MK+69] which is approximated by the smooth part of $\mu(k)$. The post edge background is generated by fitting $\mu(k)$ to a multi-section polynomial spline function [TL79, LC+81] (usually 2 to 5 equal segments is adequate). In the spline fit the parameters of each section are constrained so that the function and its derivative are continuous over the junction. A rule of thumb is to use 1 section for every 3-4 \AA^{-1} . One must be careful when choosing the number of segments. If the number is too small, the background is not separated well enough and low frequency artifacts remain. If the number of sections is too large, the background follows the EXAFS oscillations and the EXAFS amplitudes are underestimated. Ideally the low frequency background components of $\mu(k)$ are removed by a subtraction of an appropriate spline polynomial without affecting the EXAFS oscillations which have a higher frequency. Figure 3.1c shows a (3 section, cubic spline) background subtraction performed on the Ni K EXAFS spectrum of nickel

metal. In all of the metallic glass analysis 2 sections were used due to the shorter k range.

In order to normalise the intensity of the fine structure, the program then divides this difference ($\mu(k)-\mu_o(k)$) by the edge jump (J) taking into account the difference in slope between the pre and post edge to obtain,

$$\chi(k) = \frac{\mu(k) - \mu_o(k)}{J} \quad (3-1)$$

where $J=(a_j+b_jE)$ and a_j is the value of the edge jump, and b_j is the difference in the slopes of linear least squares fits to the pre and post edge. The latter is illustrated by the dashed lines in figure 3.1d. The normalized $k^1\chi(k)$ spectrum is shown in figure 3.1e.

(b) Fourier Analysis

$k^1\chi(k)$ (fig. 3.1e) is then Fourier transformed. The magnitude of the Fourier transform (FT) of the Ni K EXAFS of Ni metal, shown in figure 3.2a, is a pseudo-radial structure function $F(R)$. This gives a qualitative picture of the local structure around the Ni. Other stages of the analysis are needed in order to obtain quantitative structural information about the local environment of the absorbing atom. One must not confuse EXAFS FT's with the well known pair distribution function $G(R)$, derived from experimental neutron and/or X-ray scattering intensities. The latter gives the number distribution of distances between pairs of atoms, independent of the type of

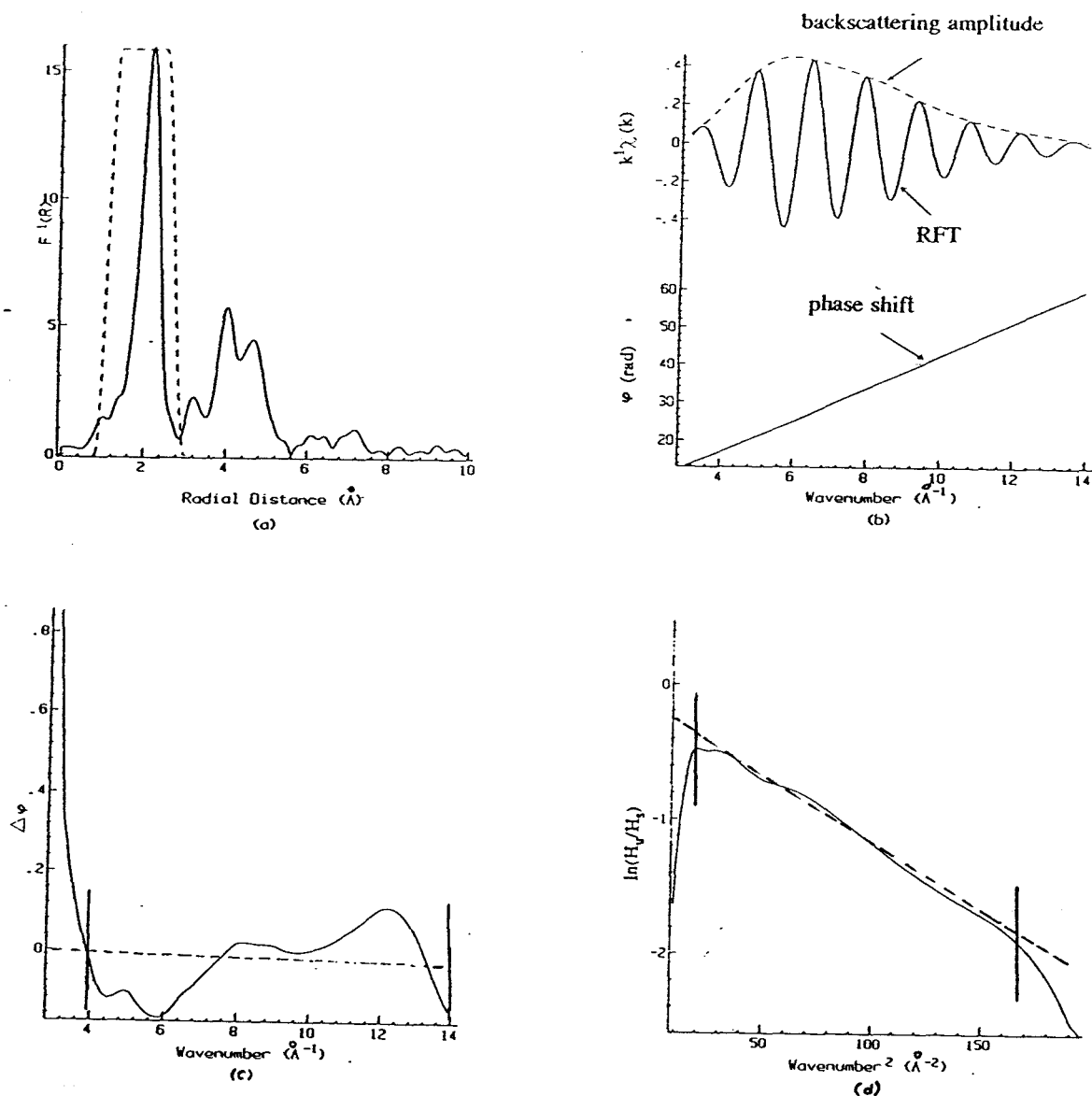


Fig. 3.2 (a) The magnitude of the Fourier transform of the normalized $k^1\chi(k)$ spectra (fig. 3.1 e). The dashed line shows the Fourier filtering of the first shell in the range 0.8-3.0 \AA using a symmetric window function; (b) the reverse Fourier transform (RFT) of the filtered region, experimental backscattering amplitude (illustrated by the dashed line), and the total phase obtained from the RFT; (c) phase shift difference obtained from the ratio method between the first shell of nickel and McKale's theoretically derived phase shifts. The dashed line shows the linear least square fit in the range 4-14 \AA^{-1} ; (d) the corresponding amplitude ratio obtained from the ratio method. The dashed line indicates the linear least squares fit used to determine the intercept and thus the coordination number.

atom. EXAFS FT's give radial distance distributions about specified atoms and provides only very short range information.

EXAFS spectra are recorded over a finite energy range (and hence finite k space). Thus the Fourier transform is taken between, k_{\max} and k_{\min} , the maximum and minimum k values of the experimental data.

$$F(R) = (2\pi)^{-1/2} \int_{k_{\min}}^{k_{\max}} W(k) k^n \chi(k) \exp(2ikR) dk \quad (3-2)$$

$F(R)$ consists of a number of peaks located at R values slightly less than the actual R_j distances. Since the transform is made without including the phase shift $\delta_j(k)$, all of the peaks in $F(R)$ are shifted closer to the origin by 0 to 0.5 Å. For medium Z backscatterers the phase shift is approximately linear ($\delta(k) \approx \alpha k - \beta$) and the peaks in the FT occur at $(R - 2\alpha)$. The factor $W(k)$ on the right-hand side of eqn. 3-2 is a window function. When transforming over a finite range in k space, the analogous infinite range transform is convoluted with the transform of the window function. When only a short data range is available, artifacts such as side lobes or ringing can occur in the Fourier transform. A window function that smoothly tapers the EXAFS intensity down to zero at k_{\min} and k_{\max} minimizes the FT artifacts at the expense of some loss of resolution. It should be noted here that a window function was not used in forward Fourier transforming in the analysis presented in this thesis.

(c) Phase shifts and Backscattering Amplitudes

If the identity of the backscattering atom is known theoretical values of $\delta_j(k)$, the EXAFS phase shift (see eqn. 1-11) appropriate to that element [TL79] can be incorporated in the FT in order to have a correct distance scale. Alternatively, $\delta_j(k)$ can be deduced from the EXAFS spectrum of a standard or reference compound of known structure where N_j and R_j are known. One may then deduce structural parameters for an unknown structure by using phase and amplitude functions derived from the model compound EXAFS and assuming phase transferability [S88b]. Figure 3.3 shows the phase shifts for Ni (i) calculated by McKale et. al. in a spherical wave scattering theory [MV88], (ii) calculated by Teo and Lee [TL79] in the plane wave approximation, and (iii) derived from the Ni metal experimental EXAFS data. For the latter the dominant 2kR component of the total phase has been subtracted. The slopes of a linear fit to these curves over 5-12 \AA^{-1} are -.6272, -.6565, -.6314 rad \AA^{-1} for i, ii and iii respectively. This suggests that the spherical wave calculation gives a better agreement with experiment than the plane wave calculation although the difference is actually very small. The spherical wave phases are believed to be more accurate in the low k region ($< 4 \text{\AA}^{-1}$) where the plane wave approximation breaks down. The metallic glass samples were analyzed (through curve fitting procedures) using McKale phase shifts and backscattering amplitudes. The types of analysis that were performed, (ratio method and curve fitting) are described in the next two sections.

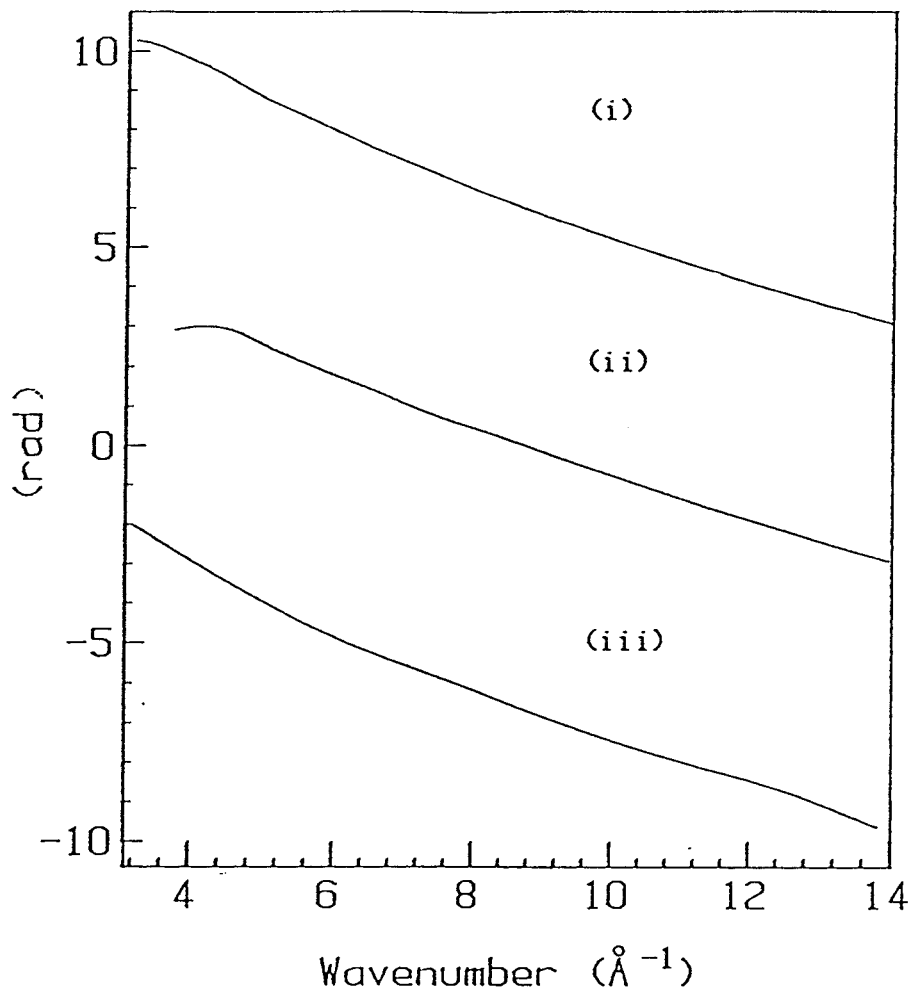


Fig. 3.3 Ni-Ni phase shifts (i) calculated from McKale's spherical wave model, (ii) calculated from Teo and Lee's plane wave approximation, and (iii) experimentally derived from Fourier filtered first shell EXAFS of polycrystalline nickel metal. The phase is modulo (2π) .

3.3 Single Component Ratio Method Analysis

The structural information that can be obtained from k space analysis includes the distance R_j , the coordination number N_j , Z_j the type of jth atom in the shell at R_j , and the relative mean square disorder σ_j^2 about the average distance R_j .

In general, the parameters ($R, N, \Delta\sigma, E_0$) relevant to a particular structural model are deduced from the Fourier filtered experimental EXAFS (via analysis of the reverse Fourier transform (RFT)). The results obtained are somewhat dependent on the choice of the R range and the reverse transform window. Choosing a wide R range that includes frequency components from other shells may interfere with the result. On the other hand, a too narrow R range may lose valuable information relevant to a multi component structural shell. The choice of Hanning window functions (symmetric or asymmetric) for Fourier filtering may also affect the result. Figure 3.2a illustrates the filtering of the first shell of Ni metal (at ≈ 2.1 Å in the FT, corresponding to the nearest neighbour distance of 2.49 Å [P58]) via a symmetric window function (shown by the dashed curve) over the range of 0.8-3.0 Å.

The RFT, experimental backscattering amplitude (shown by the dashed line) and total phase are shown in figure 3.2b. The RFT (shell-by-shell) permits a well defined phase and amplitude function to be determined for each shell distinguishable in the $F(R)$ function. From the phase and amplitude functions, one may obtain the structural parameters. In order to do this one needs to correct for the scattering phase

shift ($\delta(k)$) and 'calibrate' the amplitude scale. Model phases or amplitudes (either calculated or derived experimentally) are needed. One way to obtain these parameters is by the so called ratio method.

For the sample analysis described in this section, the unknown data is first shell nickel metal and the model data is McKale's calculated phase shifts and amplitude functions. When using theoretical phase shifts and amplitudes the R_s , σ_s^2 , λ , in $\chi_s(k)$ are equal to zero and N_s is equal to 1. In addition, spherical wave phase shifts and amplitudes are distance dependent. In the McKale approach one chooses values calculated for distances of 2.5 or 4 Å as appropriate. In this particular example, as in the metallic glass analysis, phase shifts and amplitudes for 2.5 Å were used.

Once the unknown $\chi_u(k)$, and known $\chi_s(k)$ have been obtained, the phase factor for a particular shell, $\varphi_j = 2kR_j + \delta_j(k)$, can now be separated. Taking the difference one obtains [C85, LP75],

$$\Delta\varphi = \varphi_u(k) - \varphi_s(k) = 2k(R_u - R_s) + [\delta_u(k) - \delta_s(k)] \quad (3-3)$$

In the case of theoretical phase shifts, one assumes they are valid for all chemical environments and thus $\delta_u(k) - \delta_s(k)$ is zero. When using experimental data as a model, the scattering phase shift $\delta_j(k)$, is similar for comparable chemical environments and thus the difference $\delta_u(k) - \delta_s(k)$ is negligible. The phase transferability assumption is likely to be much better for experimental than for calculated model phase functions.

The phase difference between a sample and a standard ($\varphi_u(k) - \varphi_s(k)$) should be a linear function of k if E_0 is chosen correctly and the standard is suitable. The

optimum E_0 difference may be obtained by two methods. The first is by adjusting ΔE_0 (i.e. the E_0 of 1 k-scale relative to the other) by some amount. This is repeated until the intercept of a least squares fit to $\Delta\phi$ equals zero. The second is to vary E_0 until the position of the peak in the sine equals that in the magnitude of the Fourier transform. Figure 3.2c shows an example of the phase difference plot for crystalline nickel metal (first coordination shell) based on McKale Ni-Ni phase shift and an optimized E_0 . Note the large difference in vertical scale (radians) between Figures 3.2b and 3.2c.

The Debye Waller factor and coordination number are now obtained for the unknown by isolating the amplitudes for both standard and unknown (H_u, H_s), calculating the ratio, then taking the logarithm. This gives [LC+81, AW85],

$$\ln[H_u/H_s] = -2k^2(\sigma_u^2 - \sigma_s^2) - 2(R_u - R_s)/\lambda + \ln [N_u R_s / N_s R_u] \quad (3-4)$$

$$\text{where } H_j = (N_j A_j / R_j^2) \exp(-2k^2 \sigma_j^2 - 2R_j / \lambda)$$

The difference between distances ($R_u - R_s$) is small compared to the mean free path λ , so that the middle term can be disregarded. According to eq. 3-4 a plot of $\ln(H_u/H_s)$ versus k^2 should give a straight line, with a slope of $2\sigma_s^2 - \sigma_u^2$ and an intercept of $\ln(N_s A_s R_u^2 / N_u A_u R_s^2)$. Since $A_u \sim A_s$, using the transferability of the backscattering amplitudes, one can deduce the coordination number (N_u) from the intercept [I84]. Figure 3.2d illustrates the log amplitude ratio plot obtained from an analysis of the first shell EXAFS of Ni using McKale's amplitudes. BAN makes a least square fit to a user-selected portion of this curve and obtains the coordination number from the

intercept and $\Delta\sigma^2 = (\sigma_s^2 - \sigma_u^2)$ from the slope. In both plots (fig. 3.2 c,d) the curves do not behave linearly at low k due to multiple scattering and at high k , possibly due to truncation effects. In many cases experimentally-derived phase and amplitude data are preferable to calculated model functions since many systematic biases in an analysis based on calculated functions (such as the neglect of λ) are removed.

The ratio method can be adapted only to systems with well separated coordination shells which arise from only one backscattering element (component). If a coordination shell includes 2 or more components then one must use a k or E space fitting approach. Since the $\text{Pd}_{40}\text{Ni}_{40}\text{P}_{20}$ metallic glass contained more than one component in the first coordination shell, the ratio method was not used. All of the analysis presented in chapter 4 was performed through curve fitting, which is explained in the following section.

3.4 Multi Component Analysis

(a) General Aspects

A number of curve fitting routines for analyzing EXAFS data have been prescribed [LB77, HB82]. A non-linear least squares procedure may be used to systematically determine the values of the parameters ($R, N, \Delta\sigma^2, \Delta E_0$) which minimize the variance between the Fourier filtered experimental data and that calculated from model (experimental or theoretical) phase and amplitude functions and the combined

structural and scattering parameters.

Curve fitting analysis of the first shell Ni K EXAFS of $\text{Pd}_{40}\text{Ni}_{40}\text{P}_{20}$ (presented in chapter 4) was performed using the MFIT (multiple fit) program conceived and written by Dr. Tolek Tyliczszak at McMaster University. McKale's theoretical phase shifts and backscattering amplitudes [MV+88] were used in all cases. In order to carry out this procedure, experimentally or theoretically derived amplitude and phase shift files must first be created for the appropriate components (atoms). One assumes these values will be appropriate for an unknown material, such as a metallic glass with Ni-Ni components. Experimental phase shifts and backscattering amplitudes were not used since they were not available for all 3(Ni-Ni, Ni-Pd, and Ni-P) components. A detailed explanation of MFIT is given in section 3.4c. The underlying concepts of curve fit analysis upon which MFIT is based are described below.

In curve fitting analysis of EXAFS, based on the single scattering formulation and assuming harmonic motion (Gaussian distribution of neighbour distance), there are four parameters for each backscattering component: (a) Radial Distance (R), (b) coordination number (N), (c) Debye-Waller factor ($\Delta\sigma^2$), and (d) the energy at which the free electron has $k=0$ (ΔE_0). The Δ in c and d indicate each of the parameters are relative to the σ^2 or E_0 values of the model data. Of these parameters, R and ΔE_0 are highly correlated as are N and $\Delta\sigma^2$.

When using the MFIT program the following inputs must be made: the number of components used in the fitting, the RFT file(s) (one has the choice to fit a single file or up to a total of 4 files simultaneously), and the initial parameter values. The initial parameter values for nickel metal, for example, may be $R(\text{Ni-Ni})=2.43\text{\AA}$, $N=11$, $\Delta\sigma^2=0.01\text{\AA}^2$, and $\Delta E_0=.1\text{ eV}$. Each parameter may be allowed to vary or may be fixed to its initial value. For example in the above, all parameters except E_0 may be allowed to vary, i.e. E_0 is held constant during the least squares optimization of the other 3 parameters.

The fitting analysis is not trivial. One may obtain a perfect fit to the RFT file, and yet end up with parameter results to which one can not attribute any meaning (i.e. R, N , or σ^2 values outside of physically plausible limits). Also, the more files and components one has in the fitting the more parameters one has to deal with. MFIT allows great flexibility in choosing the number of independent parameters. This can be very useful in systematic searches for the combination of parameters which give the best fit within a physically reasonable range of parameter values. Notwithstanding, the fitting procedure is somewhat of an art and one must be very careful when trying to interpret the results (see chap. 4).

(b) General Procedure for MFIT

In order to introduce the language of MFIT the reader is referred to figure 3.4 and table 3.1. Figure 3.4 illustrates the quality of the optimized simultaneous fit to the Fourier filtered first shell Ni K EXAFS data of four irreversibly annealed Pd₄₀Ni₄₀P₂₀ samples (as made, 480K, 540K, 608K). In all cases of the metallic glass analysis sets of four files were fit simultaneously (see chapter 4 for further specific details).

Table 3.1 illustrates the output presented by MFIT. The top of table 3.1 shows the input theoretical amplitude and phase shift files (in this case, from McKales's spherical wave theory) corresponding to Ni, Pd, and P components i.e. components 1, 2, 3. The S value immediately below these files, is a number which describes the quality of the fit. The lower this number is the better the fit. S is the variance, given by

$$S = \sum_i^n (\chi_i^f - \chi_i) \quad (3-5)$$

where χ_i^f is the Fourier filtered experimental data, and χ_i is the analytical expression given in equation 1-11, which describes χ_i^f for n data points. Section A of the output (table 3.1) lists the optimized values of the fitting parameters. Section B indicates any parameters that have been fixed during the fitting i.e parameters whose values are not changed from their initially assigned value during iteration (in this case the E₀ values).

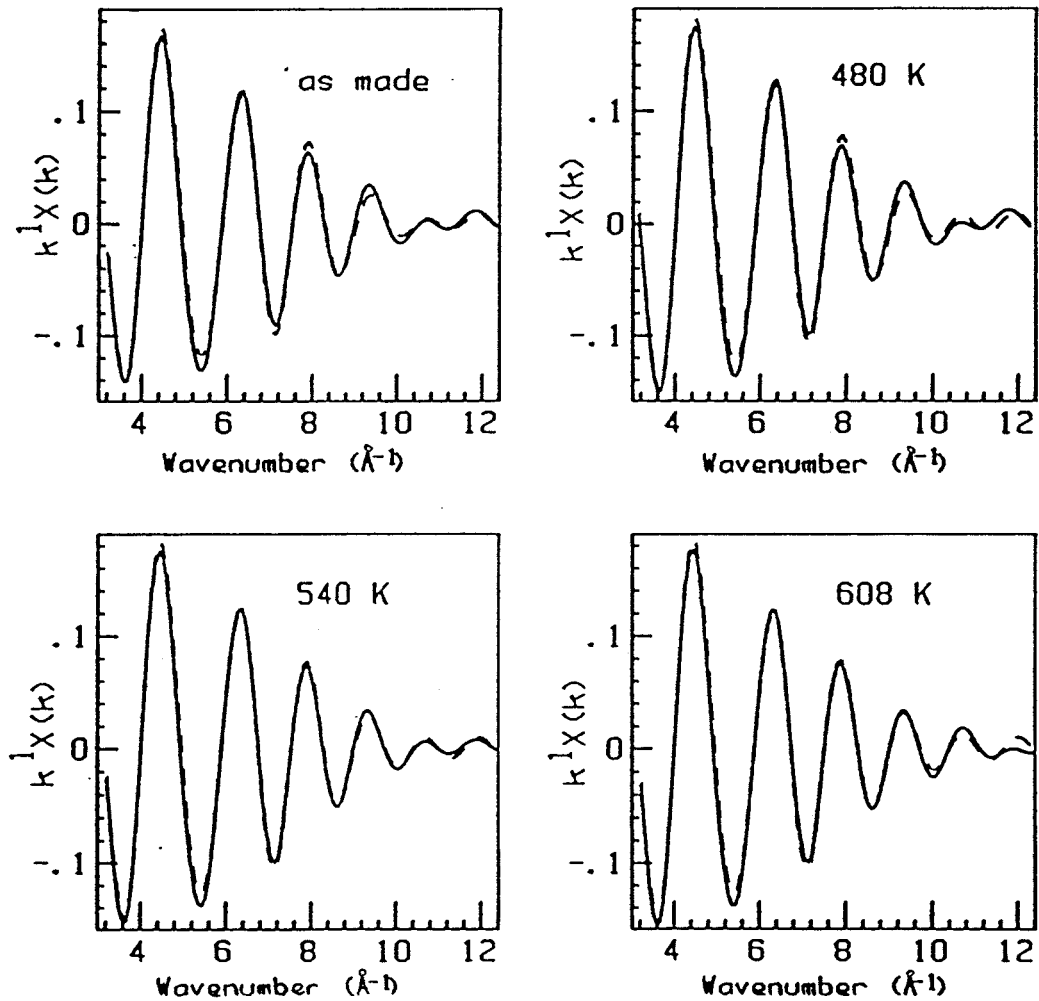


Fig. 3.4 An example illustrating the fitting quality obtained from four irreversibly annealed amorphous $\text{Pd}_{40}\text{Ni}_{40}\text{P}_{20}$ samples, (a) as made, (b) 480 K, (c) 540 K, and (d) 608 K, recorded at 300 K.

Table 3.1 Illustration of MFIT based on a simultaneous fit to the Fourier filtered Ni K EXAFS spectra of four Pd₄₀Ni₄₀P₂₀ samples.

Amplitude files [MVP+88]

Oni.ak2
Opd.ak2
Op.ak2

Phase files [MVP+88]

Onini.pk2
Onipd.pk2
Onip.pk2

S=.019

Parameter Values

	as made			480 K		
	Ni	Pd	P	Ni	Pd	P
R	2.497	2.674	2.210	R 2.497	2.679	2.207
N	0.491	1.15	0.715	N 0.565	1.26	0.726
DW	0.0029	0.0235	0.00282	DW 0.0029	0.0235	0.00285
E ₀	0.32	-0.21	0.033	E ₀ 0.32	-0.21	0.033
	540 K			608 K		
	Ni	Pd	P	Ni	Pd	P
R	2.497	2.675	2.209	R 2.497	2.678	2.216
N	0.564	1.24	0.778	N 0.575	1.32	0.836
DW	0.0029	0.0241	0.00374	DW 0.0029	0.0256	0.00479
E ₀	0.32	-0.21	0.033	E ₀ 0.32	-0.21	0.033

SECTION A: parameter values obtained from MFIT.

R = radial distance (Å)
DW = $\Delta\sigma^2$ (Å²)
N = coordination number
E₀ = ΔE_0 (eV)

Fixed Parameters

1 2 3

SECTION B: parameters that have been fixed during the fitting.

parameter matrix

	file 1			file 2			file 3			file 4		
component	1	2	3	1	2	3	1	2	3	1	2	3
	(Ni)(Pd)(P)			(Ni)(Pd)(P)			(Ni)(Pd)(P)			(Ni)(Pd)(P)		
R	17	19	20	17	24	27	17	25	28	17	26	29
N	6	4	5	7	10	13	8	11	14	9	12	15
DW	30	16	18	30	31	21	30	32	22	30	33	23
E ₀	1	2	3	1	2	3	1	2	3	1	2	3

SECTION C: labelling scheme for the parameters in section A.

Section C indicates the labelling scheme for the parameters in the upper section (section A) of the table. For example, parameter number 19 corresponds to the Ni-Pd distance in file 1 which has a converged value of 2.674 Å. The MFIT program allows the user to fix and/or set the value of any parameter through section B and to reduce the number of parameters by forcing related parameters (e.g. ΔE_0 or R values) to be equal, through section C.

The values of the parameters may be allowed to vary dependently or independently with one another. For dependent variation, the parameter number(s) must be set equal in some or all files so that the result obtained after iteration is the same for all files. For example in table 3.1, parameter number 17 refers to R(Ni-Ni) for all four files. The converged value of 2.497 Å is the value which simultaneously optimizes R(Ni-Ni) for all 4 files. For independent variation, the parameter number(s) of each file must not be equal to that of other files so that the result obtained from the fitting is independently optimized for each file. For example, parameter numbers 6, 7, 8, 9 (table 3.1) indicate that the number of Ni backscatterers is being optimized independently for each file. Thus the converged values (.491, .565, .564, .575) differ from each other.

The advantage of dependent and independent variation as well as the ability to fix values is that one can explore the fit surface in a logical manner. In the metallic glass analysis a systematic procedure was followed to identify which parameter(s) of a particular component of a particular file have large effects on S.

EXAFS is a "sparse" data set, i.e. there is not much information contained in it. Thus, when a large number of parameters are used (12/file in this case) it is probable that the fit is over determined ,i.e. there are more degrees of freedom in the analytical expression than there is in the data. One needs to be very cautious in fitting and use the minimum number of parameters which gives a 'reasonable' fit to the data and which gives physically meaningful information.

(c) Fitting Ni Metal using Both Theoretical and Experimental Phase shifts and Amplitudes.

Figure 3.5 is an example of the fitting quality (dashed line) of an MFIT analysis of the Ni K EXAFS of polycrystalline nickel metal measured at 300 K. The first four coordination shells were analysed using phase shifts and amplitudes from (a) calculation (McKale's spherical wave model) [MV+88] and (b) experiment (first shell Ni metal). Table 3.2a and b presents the results obtained from the above fits. Table 3.2c gives the actual R and N values calculated from the Ni fcc lattice parameters [P58]. The Debye-Waller factor was estimated to be 10% of R.

As with other EXAFS analysis programs, the coordination numbers reported by MFIT are ratios of the unknown to the model (either theory or experiment). Since the actual coordination numbers are 12, 6, 24, and 6 respectively for Ni(1) to Ni(4) [P58], one would hope to obtain relative coordination numbers of 1, .5, 2, and .5 first for the four shells in the analysis using experimental models (table 3.2b) (since the

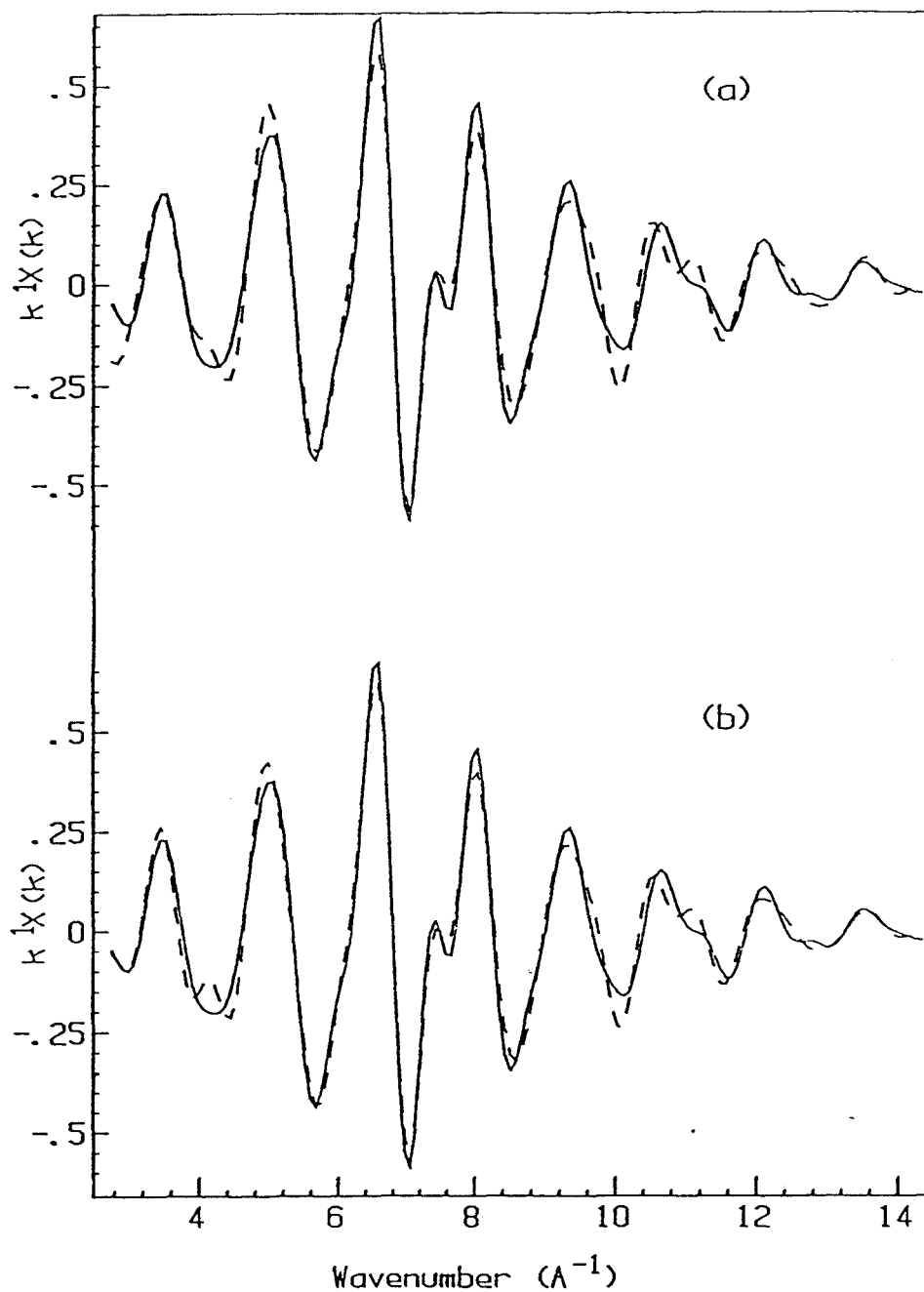


Fig 3.5 Results (dashed) of a curve fit analysis of the Fourier filtered Ni K EXAFS (solid) to the first four coordination shells of nickel metal using phase shifts and amplitudes from (a) McKale spherical wave model, and (b) Ni experimental model.

Table 3.2 Parameter results obtained from the fitting of the first 4 shells of nickel metal using phase shifts and amplitudes from (a) McKale spherical wave model, (b) Ni experimental model. R, N, DW, represents radial distance, coordination number, and Debye Waller respectively. E_0 is the energy at which the free electron has $k=0$. Actual values are shown in (c) [P58].

(a) Calculated (spherical wave) models

	<u>Ni(1)</u>	<u>Ni(2)</u>	<u>Ni(3)</u>	<u>Ni(4)</u>
R (Å)	2.488	3.482	4.362	5.237
N	4.80	1.57	5.87	4.27
ΔDW (Å ²)	4.33E-03	4.33E-03	4.33E-03	4.33E-03
ΔE_0 (eV)	-4.71	-4.71	-4.71	-4.71

S=.31

(b) Experimental (Ni first shell) model

	<u>Ni(1)</u>	<u>Ni(2)</u>	<u>Ni(3)</u>	<u>Ni(4)</u>
R (Å)	2.491	3.501	4.359	5.225
N	1.04	0.226	1.12	0.844
ΔDW (Å ²)	6.37E-05	6.37E-05	6.37E-05	6.37E-05
ΔE_0 (eV)	-6.75E-02	-6.75E-02	-6.75E-02	-6.75E-02

S=.21

(c) Actual

	<u>Ni(1)</u>	<u>Ni(2)</u>	<u>Ni(3)</u>	<u>Ni(4)</u>
R (Å)	2.487	3.517	4.307	4.973
N	12	6	24	12
DW (Å ²)	0.062	0.124	0.185	0.247

amplitude model corresponds to 12 backscatterers). On the other hand the calculated model (table 3.2a) should give the actual coordination numbers, since the model is supposed to correspond to a single Ni backscatterer. Since many factors are not included in calculated models (such as λ , σ^2 , correction for-multi-electron processes), the values obtained for the coordination numbers are approximately 2 to 3 times lower than they should be in reality. Also one would expect the difference of DW factors between the model and unknown, to have a finite positive value since the first shell motion is more correlated than motions between absorber and second, third and fourth shells. ΔE_0 should be zero since all of the atoms are Ni in the sample and thus the interatomic potential should be constant. The radial distances (R) for the four nickel backscattering components (Ni(1) to Ni(4)) corresponding to the four coordination shells are in fairly good agreement with known values for both fits a and b. On the other hand the coordination number (N), Debye Waller (DW) factors, and E_0 values are perhaps better when using experimental phase shifts and amplitudes (tab. 3.2 b). In addition the variance (S) is better for experiment (.2) than for calculated (.3). When calculated phase shifts and amplitudes are used many factors (such as λ etc.) are not included from the EXAFS equation. Thus it is not surprising that the N and DW values are rather poor.

Although the radial distances obtained from the calculated phase shifts and amplitudes are in fairly good agreement with literature, the N and DW values seem to be less reasonable (when compared to actual values) than that from experimental phase

shifts and amplitudes. Thus it seems that using experimental model phase shifts and amplitudes would be better when performing curve fit analysis. In the case of amorphous metals, crystalline compounds of similar composition can be used as a standard for EXAFS analysis. Since the local environment and chemical state (local bonding) should not be much different between crystalline and amorphous states, phase shifts and backscattering amplitudes are expected to be transferable [HS80, CBJ84]. All of the fitting analysis of the $\text{Pd}_{40}\text{Ni}_{40}\text{P}_{20}$ of Ni K EXAFS was performed using calculated phase shifts and amplitudes from McKale's spherical wave model since appropriate models were not available for the Pd-Ni-P system. The specific fitting procedures used for the metallic glasses are discussed in more detail in section 4.9.

3.5 Errors in EXAFS Analysis

Most errors in the results arise from systematic errors in the analysis. The largest uncertainties are associated with the fundamental limitations (inaccuracies or incomplete descriptions) of the EXAFS theory. The correct determination of E_0 is not fully known. Several phase and amplitude models have been developed (plane wave and spherical wave approximations) for EXAFS analysis. When using a reasonably large k_{min} ($>4 \text{ \AA}^{-1}$) there is little difference (see fig. 3.3).

The second class of errors in relative importance involves factors associated with the manipulation of the data during analysis. These include k-space conversion (weighting factor), background subtraction (number of sections, power of spline, etc.), Fourier transforming (truncation effects), and RFT (type of window used, filtered range). Variation in these procedures can affect results in many different ways. The influence of these error sources is best explored by repeating the analysis of a single data file with a range of (reasonable) choices of analysis procedures (e.g. background subtraction with a 3 section cubic, 4 section cubic, 4 section quadratic). Only answers which are relatively insensitive to these variations should be accepted.

Thirdly, random statistical precision such as beam fluctuations, samples with non uniform thickness, may lead to uncertainties in normalization. Comparison of different data files for the same sample is useful in evaluating the relative importance of this source of error. In general, the statistical precision for EXAFS of bulk samples recorded in transmission, is a negligible limitation on the accuracy of the final result.

CHAPTER 4

Ni K EXAFS OF Pd₄₀Ni₄₀P₂₀ METALLIC GLASS

4.1 General Introduction

Sections 4.2 and 4.3 introduce metallic glasses and the problem of structural relaxation during thermal annealing. The Ni K and Pd K edge EXAFS studies performed on the Pd₄₀Ni₄₀P₂₀ metallic glass in comparison to a polycrystalline Pd₅₀Ni₅₀ alloy are then presented in section 4.5. The following section (sec. 4.6) presents simulations of the Ni K and Pd K EXAFS of Pd_xNi_{1-x} using two different structural models, in order to explore the sensitivity of EXAFS to the composition and geometry of the first coordination shell. In addition, simulations of first shell EXAFS signals which include Pd, Ni, and P backscatterers were explored in order to observe the effect P has on the shape or position of the features. Comparison of these simulations with those for the Pd₅₀Ni₅₀ alloy as well as with experimental data were made. Section 4.7 presents the experimental backscattering amplitude for the "as made" sample, and calculated backscattering amplitudes for Ni, Pd, and P in order to show that the Ni atoms in the Ni-Pd-P system are surrounded by a mixture of all three components. Section 4.8 presents EXAFS difference analysis of samples annealed at

various temperatures in order to observe expected trends in the data. In order to attain sensitivity to the rather small structural variation involved, a multiple file fitting procedure (MFIT) has been used. The details of how MFIT was applied to the Ni K-edge metallic glass data are given in section 4.9. The MFIT results are presented in section 4.10. The meaning of these results and the progress made towards a satisfactory structural analysis are discussed in section 4.11. Although a fully optimized analysis has not yet been achieved, this work is a foundation upon which a more satisfactory analysis may be carried out.

Pd K-edge spectra were also recorded, but have not been analysed with MFIT or presented in detail in this thesis due to time and space limitations. An attempt was made to record the P 2p (0.14 keV) spectra of these materials at SRC (Stoughton, Wisconsin), but this was not successful due to the extremely surface sensitive nature of X-ray absorption at low photon energies and the poor quality of the surface (top 100 Å) of these materials.

4.2 Introduction

A glass can be regarded as a stop action photograph of a liquid, but it is a solid. Generally, when a liquid freezes, the atoms or molecules take up positions in an orderly array i.e. they form a crystal. Extensive rearrangement must then take place during solidification for the atoms to adopt the configurations in the crystal. On

the other hand, in the formation of a glass, the atoms of the liquid essentially freeze in their tracks. Not only the material itself is frozen, but the very configuration of the atoms. The glass has no long range order, in other words it is amorphous. Although short range order may exist, there is no regularity or periodicity in the positions of the atoms over distances of more than a few atomic spacings. How to best describe the microscopic structure of amorphous materials is an active area of investigation, especially since some metallic glasses have technologically important chemical and mechanical properties, such as resistance to corrosion, high strength combined with ductility, as well as desirable electrical and magnetic properties [CT80].

There exists at least one crystalline phase that is more stable than the amorphous state for metals. That is to say, the crystalline form is favoured thermodynamically (lower free energy) and so metallic glasses will tend to crystallize spontaneously. The chemical bonding of atoms in a metal are not strongly directed from one atom to another in space. The solid coheres through the mutual interaction of the positively charged ions and negatively charged electrons. Therefore a crystal could be reconstructed from a metallic glass with a small investment of activation energy. It was for this reason that solidifying metals in an amorphous state was long considered impossible.

Metallic glasses therefore, are in metastable equilibrium. Thermal annealing causes changes in their structure known as structural relaxation [SB+88a]. Since this can affect their physical properties [IC+85, SB+88a] it is important to

understand the structural changes involved. Structural relaxation, can be divided into two categories, (1) irreversible relaxation which involves changes that occur when as-prepared glasses are annealed for the first time: and (2) reversible relaxation which involves the cycling of the system between states with different properties and different bulk structures by annealing at different temperatures.

Although structural relaxations are well documented, there is remarkably little known about the atomic changes involved, or even whether the irreversible and reversible processes differ qualitatively. Irreversible relaxation has been shown to lead to changes in density [CG+85], viscosity [TS+80], and diffusivity [CK+78]. This strongly suggests that irreversible relaxation involves a decrease in free volume through an increase in packing fraction (e.g. by elimination of voids), which leads to an increase in topological short range order (TSRO), as detected by X-ray diffraction. Such a process would involve long range diffusion. On the other hand, since the energy of a metal is a strong function of volume, it seems unlikely that reversible relaxation involves significant changes of volume. The latter suggests that reversible relaxation involves the local atomic rearrangement with only a few jumps per atom, which is believed to be a change in chemical short range order (CSRO). Unfortunately there have not been many measurements made to test these hypotheses directly and quantitatively.

General structural studies of amorphous metals have been reviewed by Cargill [C84]. Many EXAFS studies of disordered solids have been made [H78,

HB82], including a considerable body of work on amorphous metals [CB+87, CE+87, MT+88]. Yu et al. [YR+88] have used Fe K EXAFS to probe the changes associated with initial low temperature anneals of an Fe-Si-B alloy. Based on their results they concluded that there were only small changes in the CSRO around Fe in the low temperature annealing.

Other techniques [BRS90, BS90, SB+88] have been used to study the structural relaxation of Pd-Ni-P metallic glasses. There is evidence from differential scanning calorimetry (DSC) and Mossbauer [SB+88] for a fundamental difference in Pd₄₀Ni₄₀P₂₀ between reversible changes occurring at low temperature (<480 K) and high temperature (>500 K). However, conventional X-ray diffraction is not sensitive enough to detect the changes created by the low temperature anneal.

To my knowledge, there have not been any EXAFS studies of the Pd₄₀Ni₄₀P₂₀ metallic glass prior to this work. The local structure changes in reversible and irreversible relaxation for the Pd-Ni-P system may be detected by the local structure sensitive capabilities of EXAFS. If EXAFS can detect and quantify changes in local structure associated with relaxation, this would provide direct evidence for the hypothesized chemical ordering.

Measuring EXAFS from all three elements (Ni, Pd, P) of Pd₄₀Ni₄₀P₂₀ should provide information about the local structure around each element as a function of annealing temperature. Combining this information would be the best way to use EXAFS as a probe of the small changes involved in the structural relaxation of this

material. Since the properties of some metallic glasses depend highly on the structure, information obtained from EXAFS describing the processes occurring with annealing could give valuable information to scientists concerned in this area of research.

4.3 Scientific Problem

The sample preparation and framing of the scientific problem was performed by Ralf Brüning, from McGill University. In addition to this he helped in data acquisition at NSLS as well as some data analysis at McMaster. Figure 4.1 shows results obtained from X-ray diffraction studies [BRS90] of the Ni-Pd-P system, which illustrate the fundamental difference between irreversible and reversible changes at low and high temperatures. Fig 4.1a shows $S(q)$, the X-ray structure factor of the sample in the reference state (570 K which is the highest annealed state before it turns crystalline). Fig. 4.1b and c show the change in $S(q)$ associated with irreversible and reversible relaxation i.e. the difference between $S(q)$ of the material annealed to the specified temperature and $S(q)$ of the reference state.

The relaxation process for the irreversible samples is such that the samples reach a fully relaxed state with annealing to the highest possible temperature that can be reached without initiating crystallization. Thus, one expects and observes successively smaller differences (sample minus reference state) as the annealing temperature is increased from 300 K to 540 K during irreversible relaxation (fig. 4.1

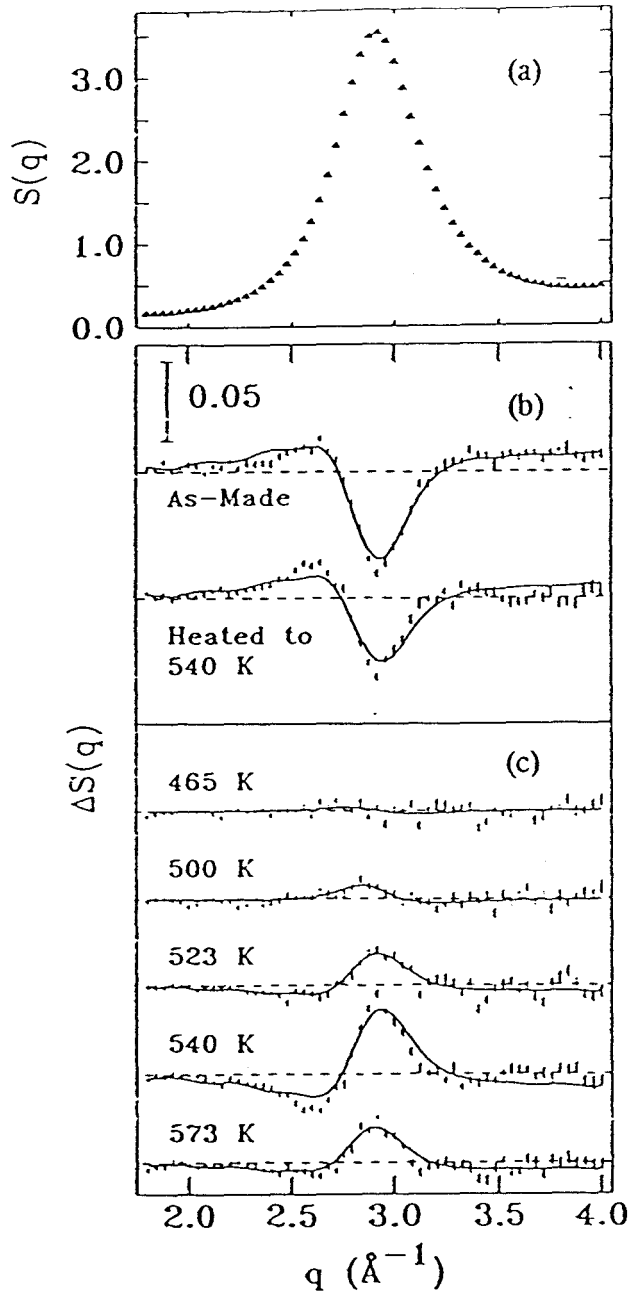


Fig. 4.1 X-ray structure factor $S(q)$ (a) of $\text{Pd}_{40}\text{Ni}_{40}\text{P}_{20}$ in the reference state (570 K anneal). Spectra of the various sample states with the reference state subtracted to illustrate the relaxation processes occurring in the (b) irreversible and (c) reversible samples [BRS90] (figure courtesy of R. Brüning).

b). The relaxation process for the reversibly annealed samples is somewhat different. The samples start at a somewhat relaxed state, since they have already undergone the structural changes of irreversible relaxation. As they are annealed to successively higher temperatures, the magnitude of the structure change relative to the reference state increases up to a certain temperature followed by a decrease. Thus an up and down trend in $\Delta S(q)$ is observed (fig. 4.1 c). An analogous difference analysis was performed on the EXAFS results to check for similar trends (see section 4.8).

It should be noted here that changes in $S(q)$ are $\leq 2\%$ (fig. 4.1). Since irreversible relaxation is believed to involve TSRO, one would expect that EXAFS would be less sensitive to these changes than X-ray diffraction. On the other hand, since reversible relaxation is believed to involve CSRO, EXAFS could be more sensitive than X-ray diffraction especially with regard to identifying preferential ordering, from differences between the Ni-K, Pd-K, and P-K EXAFS signals. The changes are still expected to be less than a few %, and thus they should be a real challenge to detect and quantify.

4.4 Preliminary Steps in the Analysis of the Pd₄₀Ni₄₀P₂₀ Ni K EXAFS Data

Although both the Ni K and Pd K edge EXAFS have been measured, only a partial analysis of the Ni K results has been achieved to date using MFIT. In addition, some qualitative information was obtained from the Pd K-edge EXAFS.

Table 4.1 indicates the samples that were measured.

A systematic analysis procedure was carried out for each of the Ni K and Pd K EXAFS spectra of the $\text{Pd}_{40}\text{Ni}_{40}\text{P}_{20}$ samples. The origin of the k-scale was set to the first maximum in its derivative spectrum (obtained by fitting a gaussian to the peak). A two section cubic spline background was subtracted in k-space. The k^1 weighted spectrum was then truncated to the zero crossing just after 2.5 \AA^{-1} and just before 12 \AA^{-1} . The R space data was truncated numerically between 0.8 and 3.8 \AA for the reverse Fourier transforms used to obtain the Fourier filtered first shell signal which was the input for the curve fitting analyses.

4.5 Comparison of the EXAFS of Amorphous $\text{Pd}_{40}\text{Ni}_{40}\text{P}_{20}$ and Crystalline $\text{Pd}_{50}\text{Ni}_{50}$

Figure 4.2 shows the Ni K EXAFS and Fourier transforms (FT) of a $\text{Pd}_{50}\text{Ni}_{50}$ polycrystalline alloy, the "as made" amorphous $\text{Pd}_{40}\text{Ni}_{40}\text{P}_{20}$ metallic glass (as spun off the Cu wheel i.e no annealing), and the reference state (highest temperature annealed amorphous sample i.e. 608 K (fig. 4.2) and 613 K (fig 4.3)). The corresponding data for the Pd K EXAFS of these three samples is presented in fig. 4.3. All spectra were measured with the samples at 300K .

Comparison of the amorphous vs crystalline results at both edges illustrates the high sensitivity of EXAFS to local order as well as the very short range over

Table 4.1 Pd₄₀Ni₄₀P₂₀ samples recorded with synchrotron radiation at NSLS, at the BNL (April 1989).

Samples Recorded at 77 K

	Annealing Temperature (K)	
	<u>Ni 1s</u>	<u>Pd 1s</u>
<u>Reversible</u>	440	440
	468	468
	493	493
	511	511
	542	523
	560	542
	613	560
<u>Irreversible</u>	as made	as made
	540	480
	613	540
		560
		580
		613

Samples Recorded at 300 K

<u>Reversible</u>	440	440
	468	468
	493	493
	511	511
	560	542
	608	560
<u>Irreversible</u>	as made	as made
	480	480
	540	540
	560	560
	580	580
	608	613

as made = no annealing

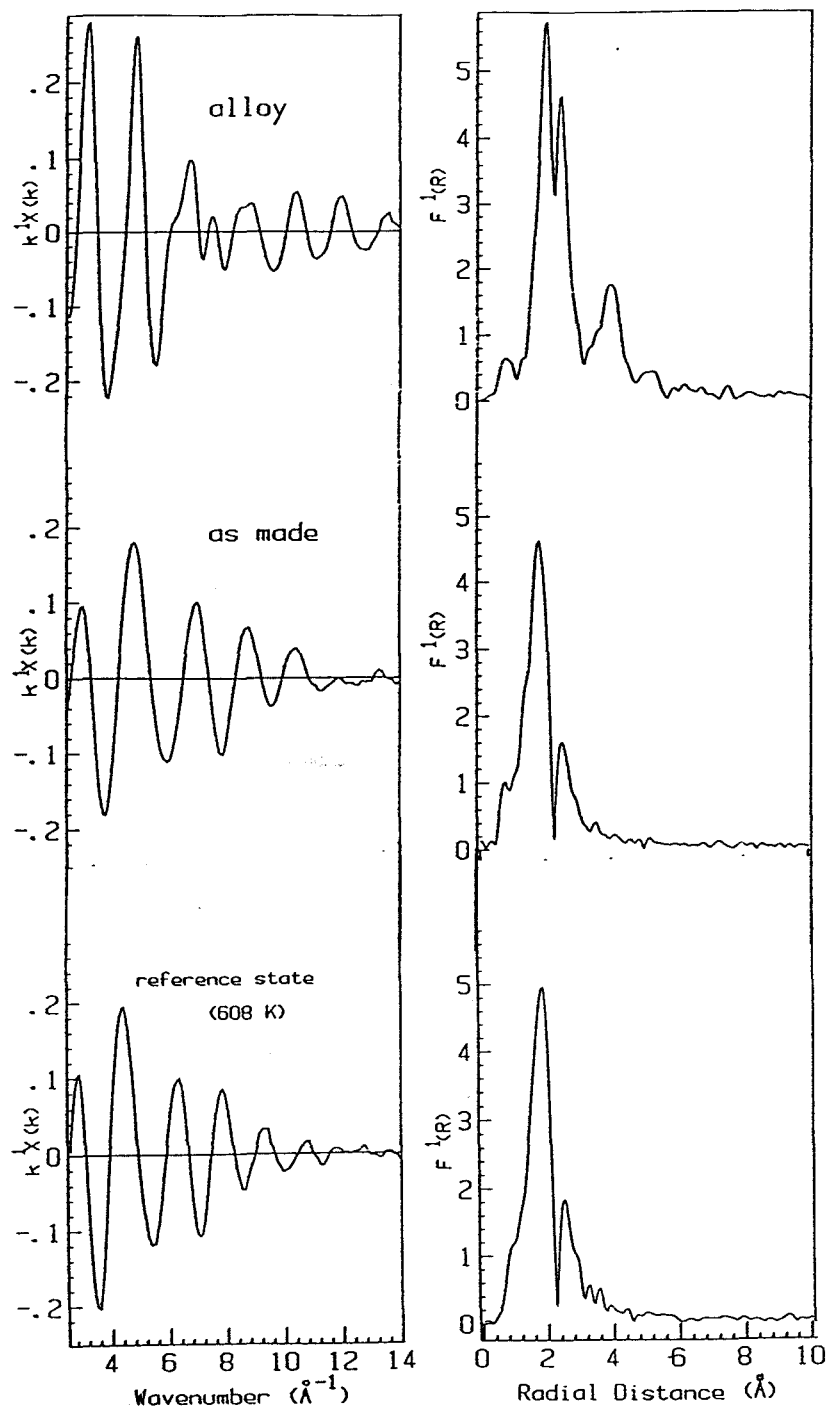


Fig. 4.2 Ni K-edge EXAFS and Fourier transforms of a polycrystalline $\text{Ni}_{50}\text{Pd}_{50}$ alloy, and "as made" and reference state (highest temperature annealed sample i.e. 608 K) amorphous $\text{Pd}_{40}\text{Ni}_{40}\text{P}_{20}$ samples measured at 300 K.

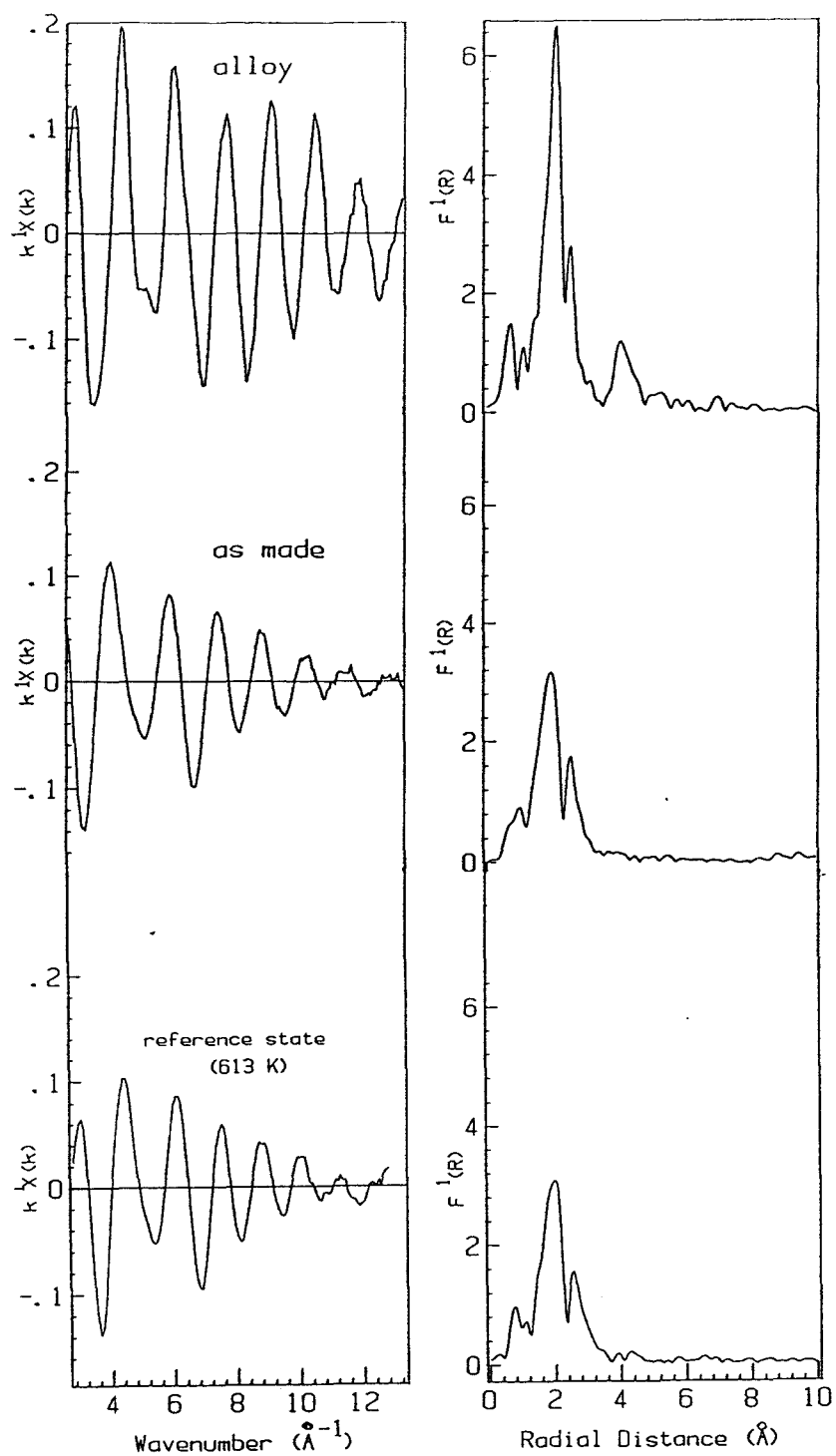


Fig. 4.3 Pd K-edge EXAFS and Fourier transforms of a polycrystalline $\text{Ni}_{50}\text{Pd}_{50}$ alloy and "as made" and reference state (highest temperature annealed sample i.e. 613 K) amorphous $\text{Pd}_{40}\text{Ni}_{40}\text{P}_{20}$ sample measured at 300 K.

which amorphous materials are ordered. A larger amplitude nearest neighbour signal is observed for the polycrystalline material in both the Ni K and Pd K k-space EXAFS signal and Fourier transforms. In addition, higher coordination shells of the polycrystalline alloy are observed at distances of approximately 4, 5, 6, and 7.2 Å in the Ni FT (fig. 4.2) and 4.2, 5.0, 5.5, 6.5 Å in the Pd FT (fig. 4.3). These are absent in the FT's of the amorphous samples. An increase in the number of well defined coordination shells and their amplitude is what one would expect with ordering of atoms. In the terminology of this chapter, the region between 0.8-3.2 Å in these FTs is referred to as a 2 component (Ni,Pd) single shell in the alloy, and a 3 component (Ni,Pd,P) single shell in the glass.

The shape of the first shell signal (0.8-3.2 Å) in the FTs of the metallic glass samples is similar but different in detail from that in the FTs of the Pd₅₀Ni₅₀ alloy (figs. 4.2 and 4.3). In all cases there are two maxima, located at approximately 2.0 and 2.5 Å in the alloy FT, and 1.8 and 2.5 Å for the amorphous samples, in both the Ni and Pd EXAFS. In large measure this structure is a beat pattern [KP88] i.e. a consequence of interference between the amplitude modulated sinusoids of slightly different frequency corresponding to the different backscattering elements. The details of the beating are known to be quite sensitive to the structural aspects of a multi-component shell [SB88]. In this case the difference between the FTs of glass and alloy should give qualitative and perhaps semiquantitative information on the differences in the first coordination shell composition.

The dip between the maxima is deeper in the FT of the EXAFS of the amorphous samples than of the alloy. The feature at 1.8 Å for the amorphous sample appears at a lower distance than that of the crystalline alloy (2.0 Å). In addition, the relative intensity of the two maxima in the alloy is different from that in the amorphous samples. The peak intensity ratio (first/second) is 1.3 (alloy) and 3 (glass) for the FT of the Ni K EXAFS and 2.3 (alloy) and 1.5 (glass) for the Pd K EXAFS. Simulations of the EXAFS of multicomponent (Pd-Ni-P) first shell were performed, as outlined in the following section, in order to investigate the sensitivity of the Ni K and Pd K EXAFS to the first shell composition.

The "as made" and reference state sample span the full range of expected variation of the EXAFS of the annealed glasses. Comparison of the EXAFS of the "as made" and maximally annealed amorphous samples in fig 4.2 shows they are very similar, although there is a slightly higher amplitude for the reference state for both the EXAFS and FTs, which is what would be expected for the ordering which occurs with annealing. Plots of the difference in the EXAFS of samples annealed at various temperatures were performed (sec. 4.8) in a manner similar to that performed by Brüning via structure factors (sec. 4.3), in order to investigate whether trends can be reliably extracted from the EXAFS data. This material is presented in section 4.9.

4.6 Investigation of the Sensitivity of Ni K and Pd K EXAFS to the First Shell Composition

Various EXAFS simulations were performed for different Pd-Ni and Pd-Ni-P systems in order to investigate the sensitivity of the first shell EXAFS signal to the composition of that shell. The simulations, performed using the program BCALC (courtesy of Dr. Tolek Tyliczszak), are based on the single scattering EXAFS formalism (eqn. 1-11). The inputs to BCALC include: (1) identity of the central absorbing atom, mean free path, k-weighting; and, for each component: (2) model phase and amplitude functions, (3) radial distance, (4) coordination number, (5) Debye Waller factor and, (6) identity of backscattering atom. The EXAFS function $\chi(k)$ is then calculated and may be Fourier transformed and otherwise analysed in a manner identical to experimental data.

Figures 4.4 and 4.5 show FTs of the simulated Ni K and Pd K EXAFS of $\text{Pd}_x\text{Ni}_{1-x}$ with various values of x, ranging from pure Ni (i) to pure Pd (vii), assuming two different models for the local structure. In all simulations, McKale's phase and amplitude functions were used, and the EXAFS spectra were truncated in the range 2.5-12 \AA^{-1} prior to Fourier transformations.

Model A (fig. 4.4a and 4.5a) assumes a structure with different distances i.e. Ni-Ni= 2.49 \AA , Ni-Pd=2.62 \AA , Pd-Pd=2.74 \AA [P58], and DW=0.001 \AA^2 . Model B (fig. 4.4b and 4.5b) assumes that the Ni-Ni and Ni-Pd distances are identical with the

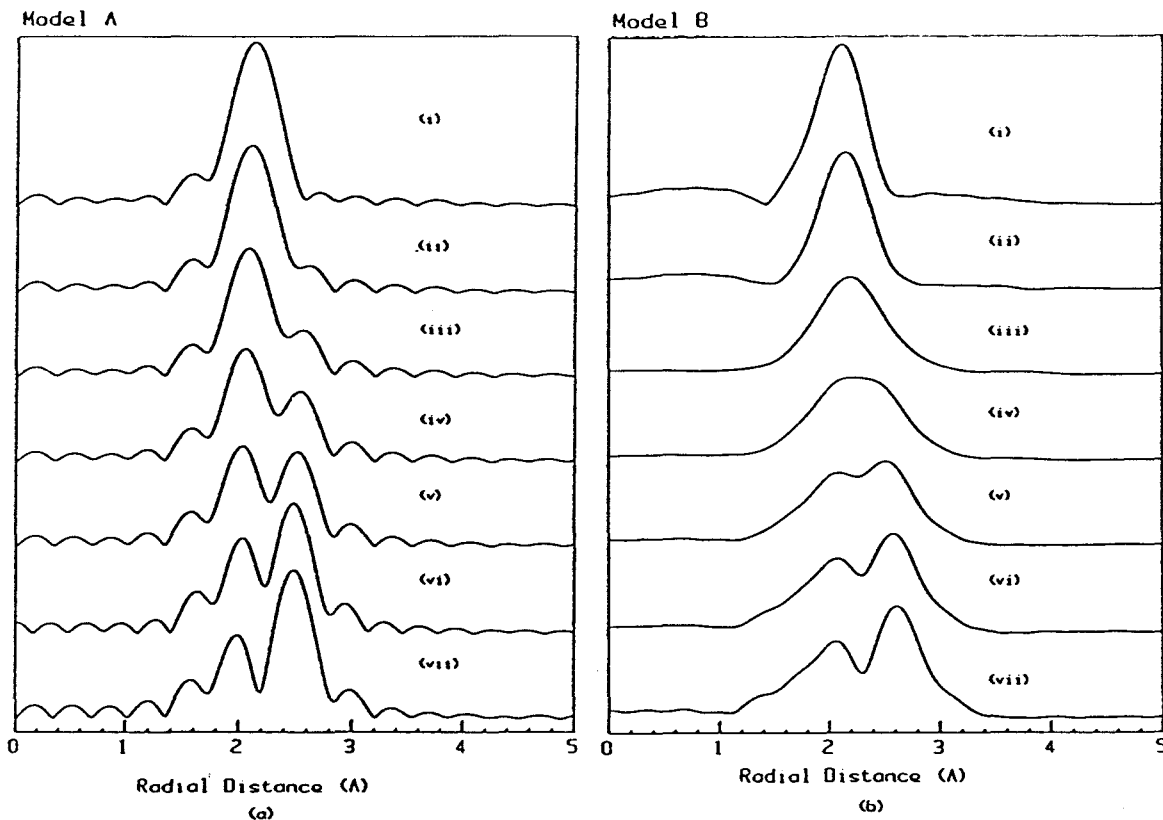


Fig. 4.4 Simulated first shell Ni K EXAFS of $\text{Pd}_x\text{Ni}_{1-x}$ where $x=0, .17, .33, .5, .67, .83, 1$ for (i) through (vii) respectively. In (a) the Ni-Ni and Ni-Pd distances were 2.49 and 2.62 Å, and in (b) the equal Ni-Ni and Ni-Pd distances were set to that determined from the fcc lattice spacing for the alloy of this composition (2.49, 2.54, 2.6, 2.64, 2.68, 2.72, 2.75 Å for (i) through (vii)). The K-range was 2.5-12 Å⁻¹, to match that used in the analysis of the alloys and metallic glasses (figures 4.2, and 4.3)

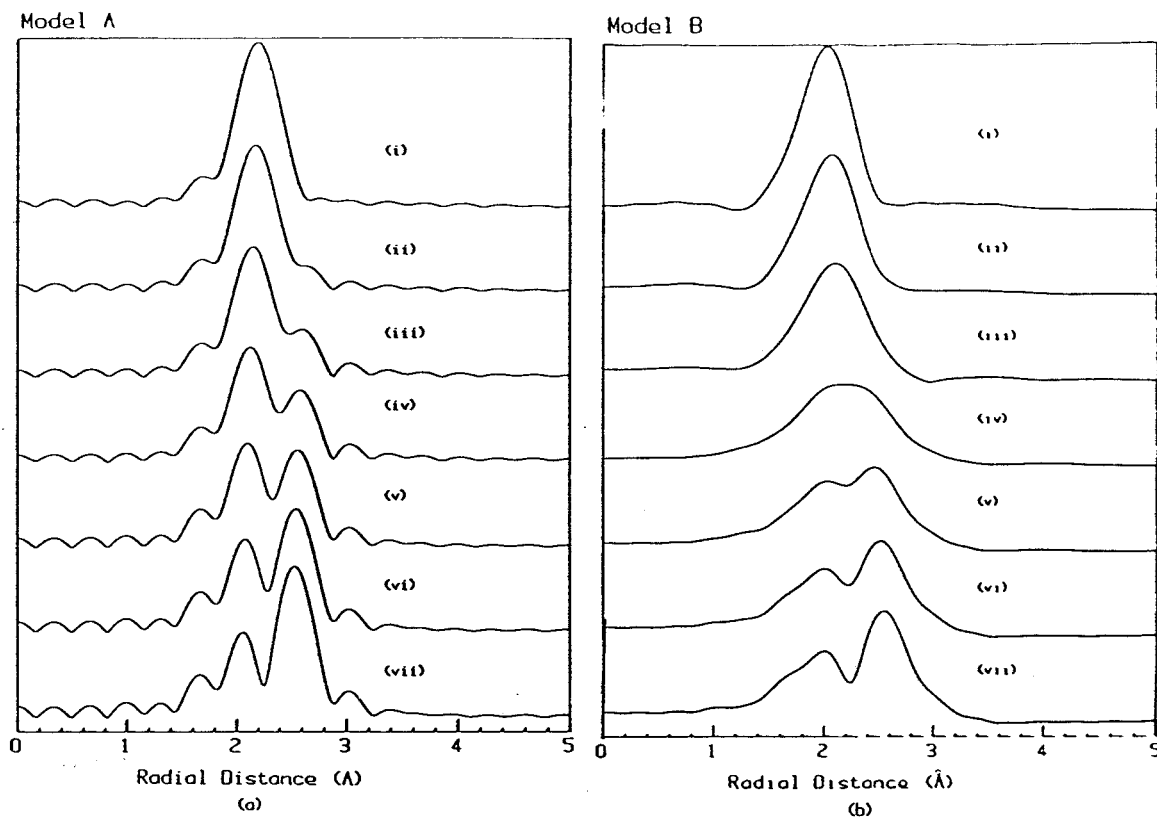


Fig. 4.5 Simulated first shell Pd K EXAFS of $\text{Pd}_x\text{Ni}_{1-x}$ where $x=0, .17, .33, .5, .67, .83, 1$ for (i) through (vii) respectively. In (a) the Ni-Pd and Pd-Pd distances were 2.62 and 2.74 Å and in (b) the equal Pd-Ni and Pd-Pd distances were set to that determined from the fcc lattice spacing for the alloy of this composition (2.49, 2.54, 2.6, 2.64, 2.68, 2.72, 2.75 Å for (i) through (vii)). The K-range was 2.5-12 Å⁻¹, to match that used in the analysis of the alloys and metallic glasses (figures 4.2, and 4.3)

value derived from the known fcc lattice spacing of that composition of a $\text{Pd}_x\text{Ni}_{1-x}$ alloy [P58], and the DW used was 0.01 \AA^2 . The curves are plotted on the same scale.

In model A (figs. 4.4 and 4.5) the FTs show a feature with principle components at approximately 2.0 and 2.5 \AA which systematically change in relative intensity with composition. The sharp minimum between the two peaks located at 2.0 \AA and 2.5 \AA is the result of two processes - in part it reflects the physical separation of the two components, but in part it also originates from interference between the contributions of closely spaced backscattering components [CB+89].

The Ni K and Pd K FTs for model B (fig. 4.4b and 4.5b) also change systematically with composition but they show a different trend in shape when compared to model A. The peak at 2.3 \AA broadens with increasing Pd composition and a second peak at 2.7 \AA is observed at (v) i.e $\text{Pd}_{0.67}\text{Ni}_{0.33}$ which eventually attains greater amplitude than the peak at 2.3 \AA . In no case is there the pattern of big peak-small peak which is seen in the experimental EXAFS of both alloy and metallic glass.

The FTs of the Ni K and Pd K EXAFS of the $\text{Pd}_{50}\text{Ni}_{50}$ and $\text{Pd}_{40}\text{Ni}_{40}\text{P}_{20}$ metallic glass samples (see sec. 4.5) show similar features and dips to those observed for model A (curve (iv), $x=0.5$) in figures 4.4 and 4.5. Curve (iv) i.e $\text{Ni}_{0.5}\text{Pd}_{0.5}$, in both the Ni K and Pd K model A simulations has the best match in shape and relative intensities of the first two peaks, i.e. 1.6 for Ni K and 1.6 for Pd K, to that of the alloy (figs. 4.2 and 4.3) which is consistent with the 1:1 ratio of Pd to Ni in this alloy (the Debye-Scherrer X-ray spectrum of this alloy was recorded to confirm its

crystallinity, composition and homogeneity). In addition, the relative intensity in curve (iii) of the Ni K simulation (2.6) has a close match to that of the metallic glass spectra in fig. 4.2 which suggests the first coordination shell around Ni is enriched in Ni relative to the stoichiometry. The relative intensities of the two peaks in the FT of the Pd K EXAFS of metallic glasses (fig. 4.3) give the best match to model A simulation for a composition in between curves (iii) and (iv) which suggests the first coordination shell around Pd is enriched in Pd. It should be noted here that these semiquantitative estimates will be weighted in favour of overestimating the Ni content of the first shell since the P component contributes only to the lower R peak. The fact that model A has a better match is very surprising since model B is accepted to be the actual structure of metallic alloys [P58]. One would expect that the quantitative analysis would give something in reasonable agreement with the trends indicated by this shape analysis.

Simulations of the Ni K EXAFS of Ni surrounded by a first shell component of Pd, Ni, and P atoms were explored in order to observe the effect P has on the shape or position of the first shell signal (fig. 4.6). As mentioned in section 4.5, the lower R feature in the FT of the metallic glass samples appears at a shorter distance (1.8 Å) than that of the alloy (2.0 Å), which may be due to the contribution of P to the first shell. Fig 4.6 compares (a) the FT of the Ni K EXAFS of the Pd₅₀Ni₅₀ alloy with (b) the model A, and (c) the model B simulations of the Pd_{0.5}Ni_{0.5} first shell EXAFS (curves (iv) in figure 4.4). The dashed curve is the result of a

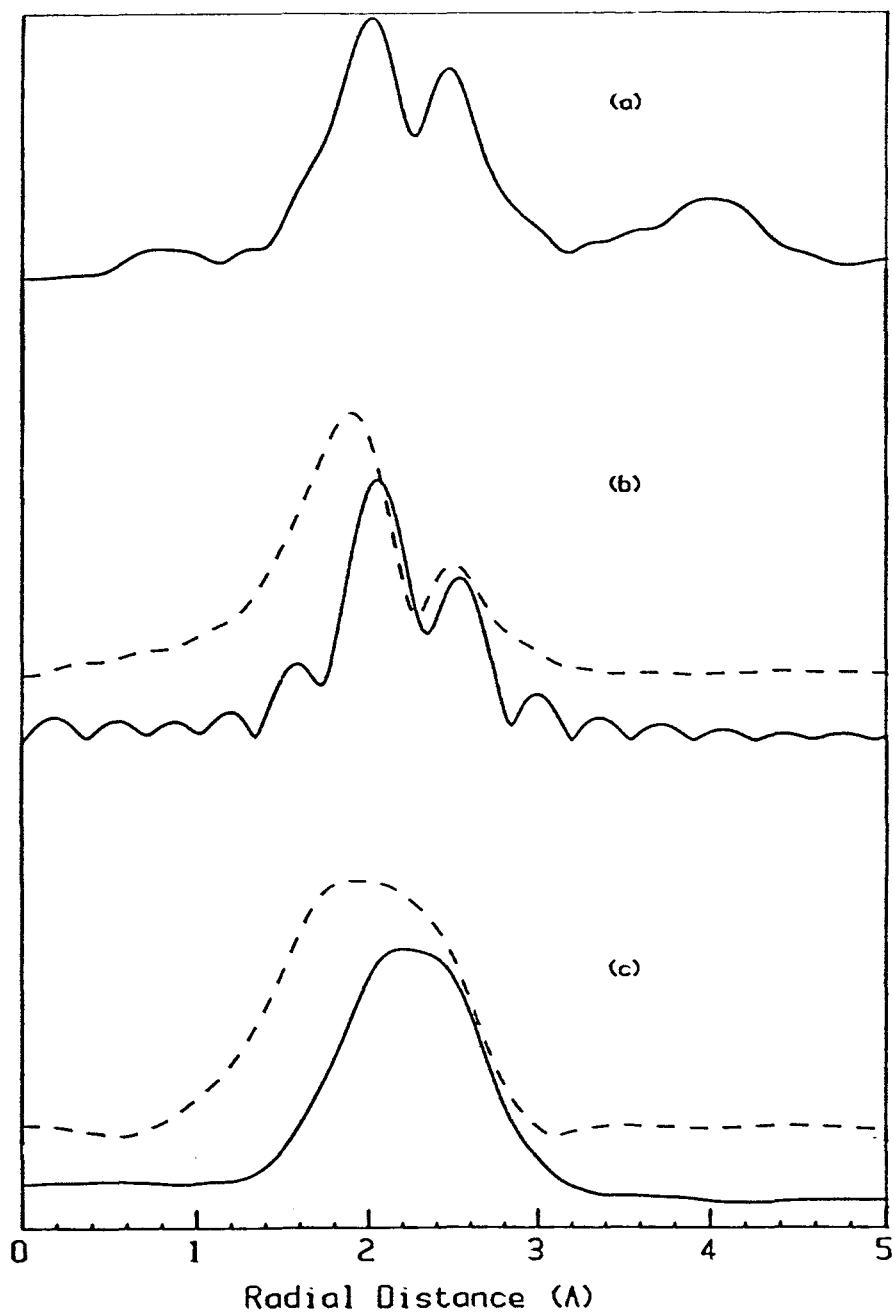


Fig. 4.6 Fourier transforms obtained from (a) experimental Ni K EXAFS of $\text{Ni}_{50}\text{Pd}_{50}$ alloy recorded at 300 K, and simulated first shell Ni k EXAFS of $\text{Pd}_{0.5}\text{Ni}_{0.5}$ calculated using model A (b) and model B (c) (see fig. 4.4). The dashed lines represent the corresponding curves obtained from FTs of simulated Ni k EXAFS of $\text{Pd}_{0.5}\text{Ni}_{0.5}\text{P}_{.25}$

$\text{Pd}_{0.4}\text{Ni}_{0.4}\text{P}_{0.2}$ simulation with a Ni-P distance Ni-P of 2.2 Å, and $\text{DW} = .01$ Å. The shapes of the curve and the ratio between the two peaks for the Pd-Ni and Pd-Ni-P systems suggest that model A (fig. 4.4a) is better than model B (fig. 4.4b). The addition of phosphorous in the first coordination shell does not change the general shape of the curve but additional intensity occurs at the lower R distances corresponding to the Ni-P contribution. Referring back to fig 4.2, it can be observed from the metallic glass FTs that the main peak is at lower distances (and has greatest intensity) than in the alloy, consistent with additional first shell phosphorous backscattering signal.

Although simulations obtained from structural model A show a better match to the $\text{Pd}_{50}\text{Ni}_{50}$ and $\text{Pd}_{40}\text{Ni}_{40}\text{P}_{20}$ metallic glass system it is generally accepted that the single distance assumed in model B is the correct description of the alloy structure. Thus, while the simulation exercise demonstrates that EXAFS is quite sensitive to the type of changes in first shell composition that are postulated in the chemical short range order (CSRO) model for relaxation in amorphous metals [C84], it also raises interesting questions as to the way in which EXAFS probes the local structure in metallic alloys. In this regard, it should be mentioned that the discrepancy between simulated and experimental EXAFS of the alloy is not related (1) to the use of McKale model phases and amplitudes since a better spherical wave treatment (FEFF) was explored with essentially identical results; (2) to DW effects since model B was tried with $\text{DW} = 0$ and did not show any splitting for a $\text{Pd}_{50}\text{Ni}_{50}$ composition like those

seen in fig 4.2; (3) to a problem of BCALC or eqn. 1-11 (the single scattering model) since the EXAFS of pure metals is reproduced perfectly (fig. 4.4, 4.5 (i) and (vii) respectively).

4.7 Ni, Pd and P Backscattering Amplitudes

The Fourier filtering analysis and the simulations discussed in the preceding section indicate that all three possible backscattering elements (Ni, Pd, P) contribute to the EXAFS signal of the metallic glasses. This is further emphasized by comparison of the shape of the first shell Fourier filtered backscattering amplitude for the amorphous "as made" sample measured at 300 K, and the theoretical backscattering amplitudes (from Mckale wave model) for Pd, Ni and P (fig. 4.7). The metallic glass EXAFS amplitude envelope shows maxima that more or less align with specific features in the Ni, Pd, and P backscattering amplitude shapes. In addition, the backscattering amplitudes (fig. 4.7) illustrate that the 3 different atomic types have readily distinguishable amplitude shapes, and thus one should be optimistic about the ability of curve fitting to derive a unique answer concerning the mix of elements in the first coordination shell. Not surprisingly, it appears that the Ni atoms in the Pd-Ni-P system are surrounded by a mixture of all three components. There is also the possibility that there is more than one Ni-X distance (where X=Ni, Pd, or P) contributing to the first shell. Thus, the challenge is to determine what the mixture is,

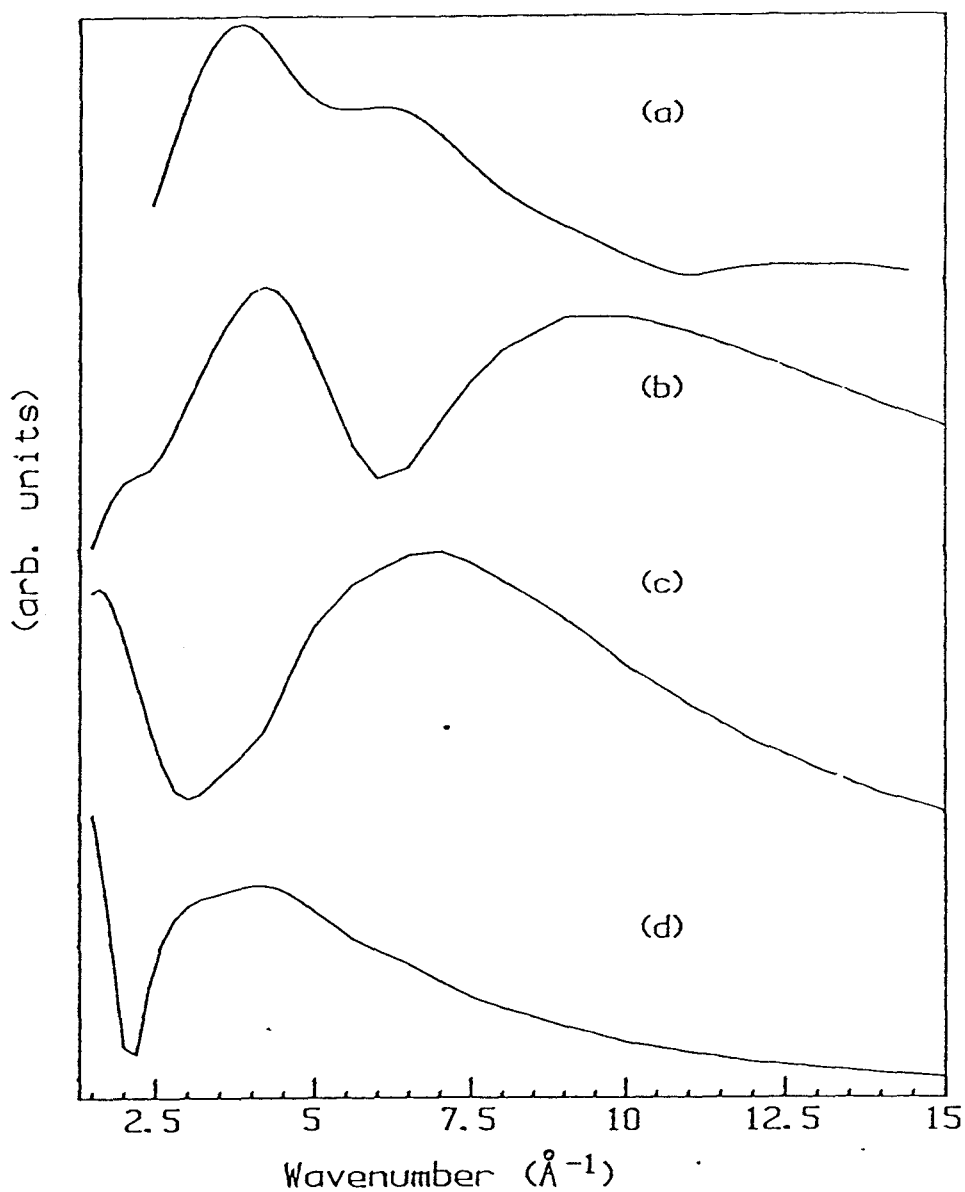


Fig. 4.7 (a) the first shell amplitude function derived from Ni K EXAFS of the "as made" sample measured at 300 K; (b), (c), and (d) show the calculated backscattering amplitudes for Ni, Pd, and P respectively as calculated by the McKale et. al. [MV+88] spherical wave formalism.

and how much it changes with annealing temperature. One hopes to see if changes in the Ni environment associated with relaxation can be deduced from the analysis of the first shell EXAFS as a combination of Ni-Pd, Ni-Ni, Ni-P backscattering components.

4.8 EXAFS Difference Plots

In order to determine if there were systematic changes in the data which could (eventually) provide structural information, difference files were prepared and analyzed. Figures 4.8-4.10 show EXAFS difference plots of samples annealed at various temperatures. The overplots (dashed lines) represent the differences of the back Fourier transforms of the first shell peaks, with respect to the reference state (highest temperature annealed sample i.e 608K and 613K for samples measured at 300K and 77K respectively). These comparisons were made to investigate if most of the difference signal is associated with physically significant frequency components (i.e. in the range 1.5-3.5 Å) rather than noise. Throughout these figures it can be seen that the difference signal is indeed associated with physically significant components. The same scale is used for all plots, and the differences were taken with respect to the reference state indicated. Figure 4.8 illustrates that the difference signal decreases when going from lower temperatures to higher temperatures which is what is expected i.e. there are smaller differences (sample minus reference state) with

IRREVERSIBLE ANNEALING

91

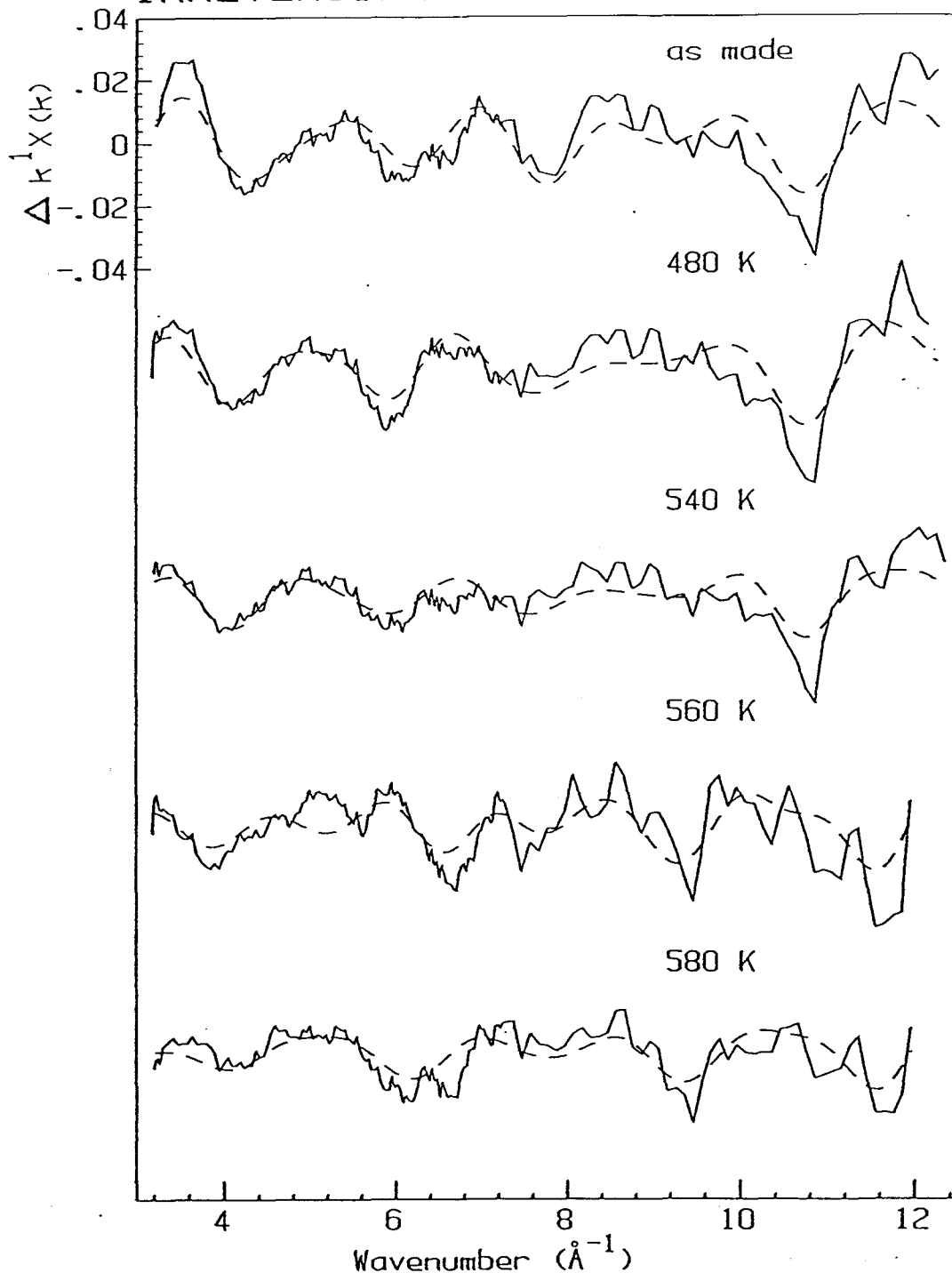


Fig. 4.8 Difference of the Ni K-edge EXAFS of various irreversible samples of $\text{Pd}_{40}\text{Ni}_{40}\text{P}_{20}$ measured at 300 K. The solid lines represent raw data differences (sample-reference) and the dashed lines represent the differences of the back Fourier transforms of the first shell peaks with respect to the reference state 608 K.

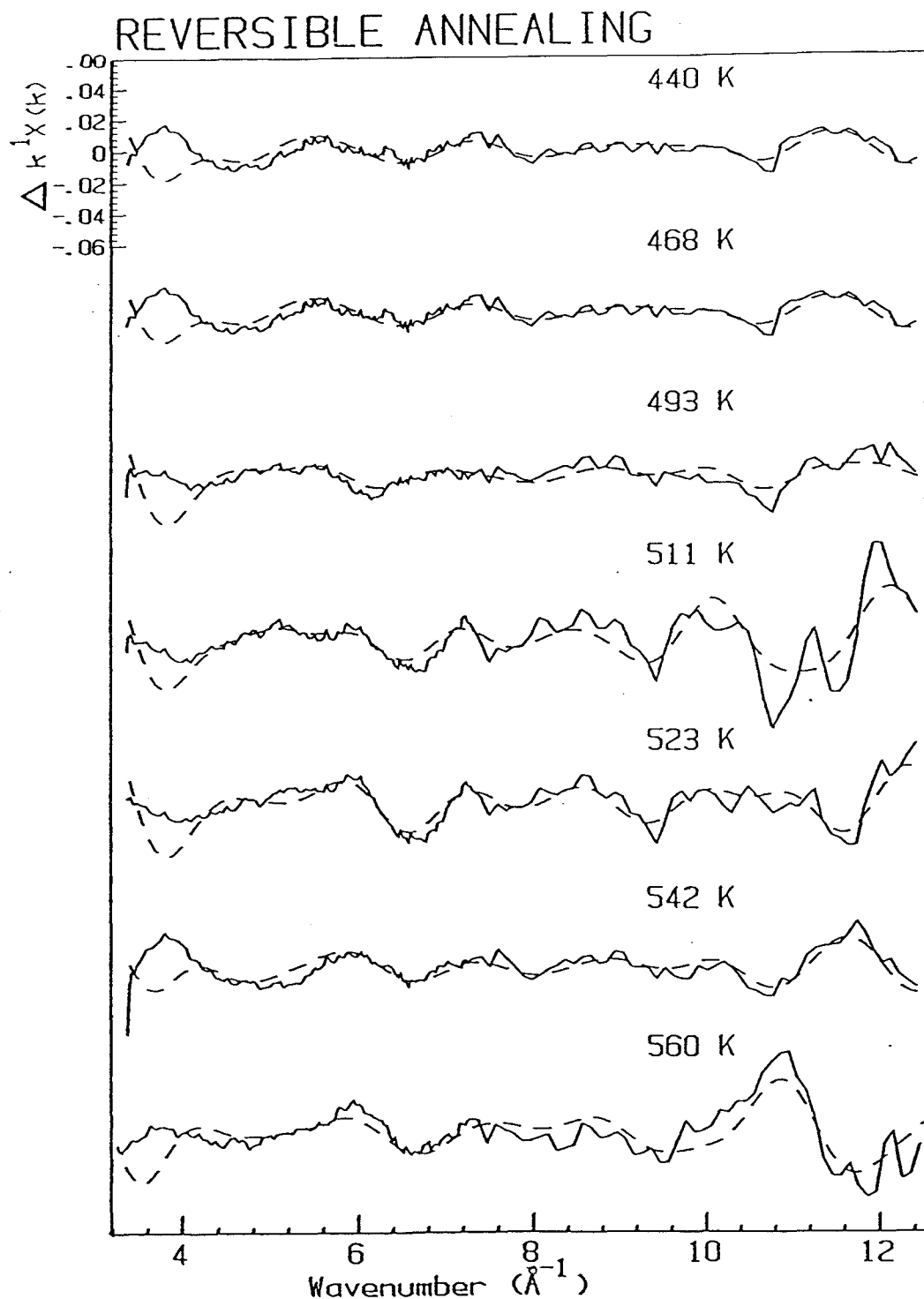


Fig. 4.9 Difference of the Ni K-edge EXAFS of various reversible samples of $\text{Pd}_{40}\text{Ni}_{40}\text{P}_{20}$ measured at 300 K. The solid lines represent raw data differences (sample-reference) and the dashed lines represent the differences of the back Fourier transforms of the first shell peaks with respect to the reference state 608 K.

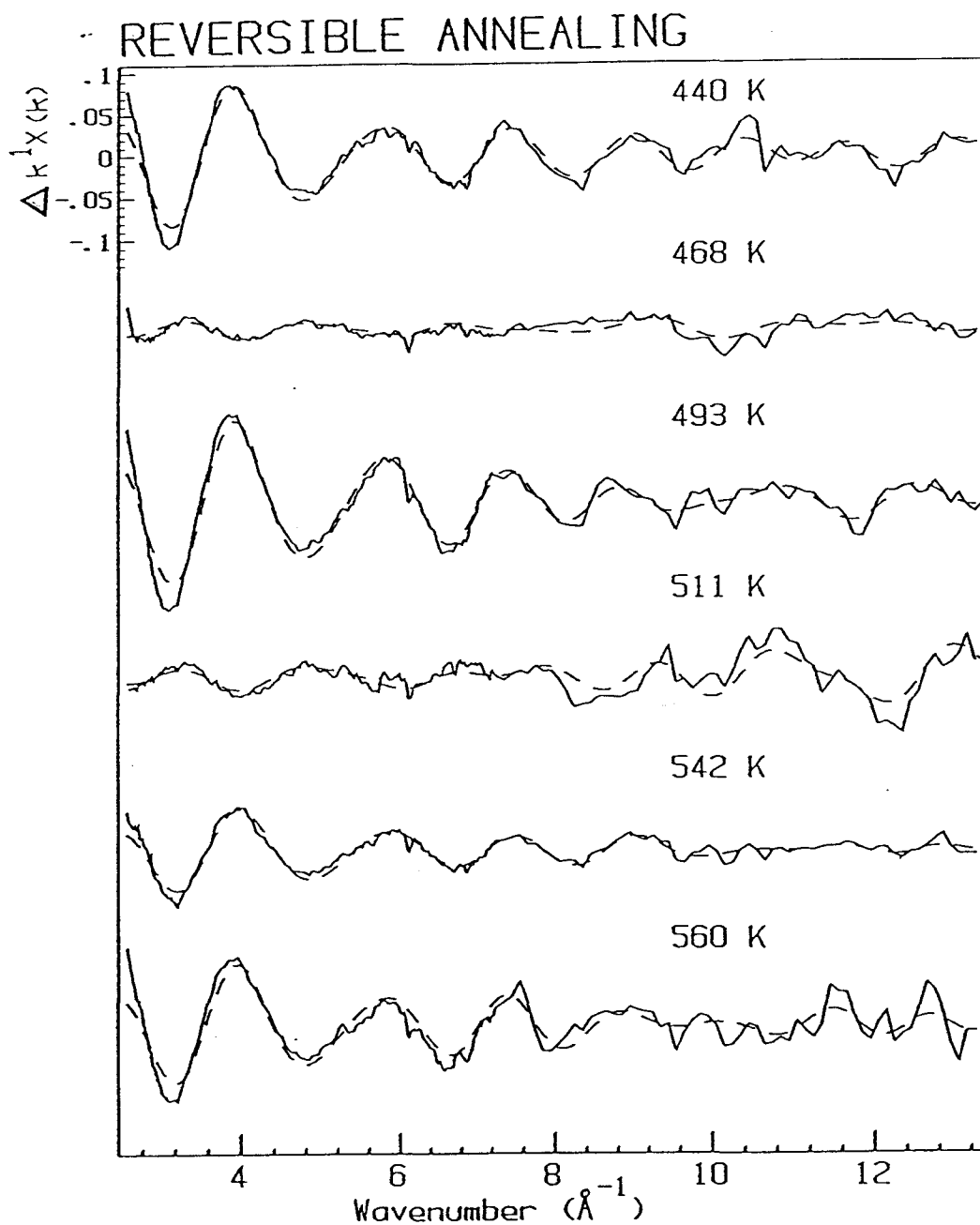


Fig. 4.10 Difference of the Ni K-edge EXAFS of various reversible samples of $\text{Pd}_{40}\text{Ni}_{40}\text{P}_{20}$ measured at 77 K. The solid lines represent raw data differences (sample-reference) and the dashed lines represent the differences of the back Fourier transforms of the first shell peaks with respect to the reference state 613 K.

increasing temperature during irreversible annealing (see sec. 4.3).

For the reversible annealing sequence, one expects an up and down trend in the difference plots (see section 4.3). This is observed in fig. 4.9 where there is an increase in the difference signal up to the sample annealed at 511K, followed by a slight decrease to sample 560K. This trend is observed in figure 4.10 if one were to ignore the 468 K and 493 K data. Since reasonable trends which matched those in $\Delta S(q)$ were observed, a systematic curve fitting analysis was initiated. The Ni K data gave a clearer indication than the Pd K data of the expected trends, so it was investigated first.

The comparisons in figs. 4.2 and 4.3 as well as the difference investigations show that the changes in the EXAFS associated with relaxation are very small. A systematic curve fit analysis is essential to have any hope in revealing trends that exist with annealing in radial distance (R), coordination number (N), and Debye-Waller factors (DW).

4.9 Multiple Fitting of the Pd₄₀Ni₄₀P₂₀ Irreversibly and Reversibly Annealed Samples.

The Fourier-filtered first shell 300 K Ni-K EXAFS spectra of 6 different reversibly annealed Pd₄₀Ni₄₀P₂₀ samples (annealed at 440K, 468K, 493K, 511K, 560K, 608K), and six irreversibly annealed samples ("as made", and annealed at

480K, 540K, 560K, 580K, 608K), measured at 300K were fitted. In addition the Fourier filtered 77 K EXAFS of three irreversible (annealed at "as made", 540K, 613K) and seven reversible (annealed at 440K, 468K, 493K, 511K, 542K, 560K, 613K) samples were analysed.

Tables 4.2 and 4.3 shows S values for fits to the first shell Ni K EXAFS of irreversible and reversible samples measured at 300 K. The S values are shown before the R and DW values were allowed to vary independently between files, and after R and DW were allowed to vary independently. These two parameters were monitored because it was deduced that they were critical in the fitting since slight changes in their values had an effect on S.

The entry "S before" in tables 4.2 and 4.3 refers to the case where the values for R and DW for one file are equal to those for all other files. Let us define the various parameters in the following way, (parameter)^x_y where x=file and y=component, in order to communicate in a simpler manner. In the "S before" we have the following $R^1_1=R^2_1=R^3_1=R^4_1$, $R^1_2=R^2_2=R^3_2=R^4_2$ etc. and similarly for Debye-Waller (DW) (a dependent variation as described in sec. 3.4b). This gives a starting point to check which parameters [R,N,DW] and components [Ni-Ni,Ni-Pd,Ni-P] have the most influence on the quality of the fit (S). Of course this answer will be dependent on the starting point. This was established in the following way. Various fits were first performed on a single file (the reference state) by random but somewhat reasonable choice of parameter value inputs. The fit showing the best S and R, N,

Table 4.2 Variance (S) obtained as a function of R independent variation for each component from the fitting of various Ni K-edge irreversible and reversible Pd₄₀Ni₄₀P₂₀ samples recorded at 300 K.

Irreversible	S		Δ S
	Before 10.E-2	After 10.E-2	
Ni	2.153	2.152	5.0E-6
Pd	2.153	2.128	2.4E-4
P	2.153	2.064	8.9E-4
Reversible			
Ni	8.705	8.688	2.3E-4
Pd	8.705	8.455	2.5E-3
P	8.705	8.453	2.3E-3

Table 4.3 Variance (S) obtained as a function of DW independent variation for each component from the fitting of various Ni K-edge irreversible and reversible Pd₄₀Ni₄₀P₂₀ samples recorded at 300 K.

Irreversible	S		Δ S
	Before 10.E-2	After 10.E-2	
Ni	2.153	2.154	9.8E-6
Pd	2.153	2.053	10.0E-4
P	2.153	2.025	1.2E-3
Reversible			
Ni	8.705	8.688	1.7E-4
Pd	8.705	8.475	2.3E-3
P	8.705	8.508	2.0E-3

DW parameter values which seemed physically reasonable was chosen as a starting point. Three additional files were then added, each starting from the same values as that from the single fitted file (reference state). Results obtained from the first set of irreversible fitting (table 3.1) seem to be fairly reasonable when considering the atomic radii for R, and estimating the DW roughly by taking 10% of R squared. In addition, N did not give negative numbers and the sum of N was within reason i.e. one expects the sum be around 6 since N is expected to be 2 to 3 times lower than what it is in reality as discussed in section 3.4c.

After the starting point was established, the R parameters are first set free to vary independently one component at a time among files being fitted while the remaining R and DW parameters remained fixed at the starting point values. That is to say that $R_1^1 \neq R_1^2 \neq R_1^3 \neq R_1^4$ after the iterations, although they all have the same value at the start, they end up with different values after the iteration process. All of the other R and DW parameters remain as a dependent variation i.e. $R_2^1 = R_2^2 = R_2^3 = R_2^4$ etc. After this procedure has been completed for the R parameters the same procedure was performed for DW. The result obtained after each independent variation is denoted to "S after". After results were obtained for one independent variation, the original starting point was used for all parameters while investigating the sensitivity of the fit quality to another parameter which was varied independently among files. The third column shows the difference (before-after). The N for each component was allowed to vary independently at all times during the fitting process. The E_o

component values were fixed at the values indicated (see appendix. I,II). Independent variation of ΔE_0 gave results which did not seem physically meaningful i.e. very large values for N, DW, and in inaccurate values of R. Although these ΔE_0 values may not be the best, they seemed to give good results for S.

The difference columns (table 4.2), indicate that allowing R(Ni-Ni) to vary independently has negligible effect on the fit quality. That is to say, S did not improve when varying R(Ni-Ni), whereas S declined more when varying R(Ni-Pd) or R(Ni-P). Similarly DW(Ni) also seemed to have negligible effect on the fitting (table 4.3).

The order in which optimization was carried out [Ni then Pd then P] is not a factor in the fitting procedure since all of the parameters were returned to a common starting point prior to each step in the controlled optimization of the fit. After the fit of four spectra were completed, 2 files were taken away and two new files were added. After fitting was complete for the six irreversible files, four new samples (reversible) were added using the parameter values of the previous four fittings and so on. Figure 4.11 is a flowchart describing the order of fitting the files, measured at 300 K. Figure 4.12 is the corresponding flowchart for the 77 K files. Since certain files (samples) were included in 2 sets of fits, two values of each parameter derived for these samples. This was used to give an estimate of the uncertainties in the results.

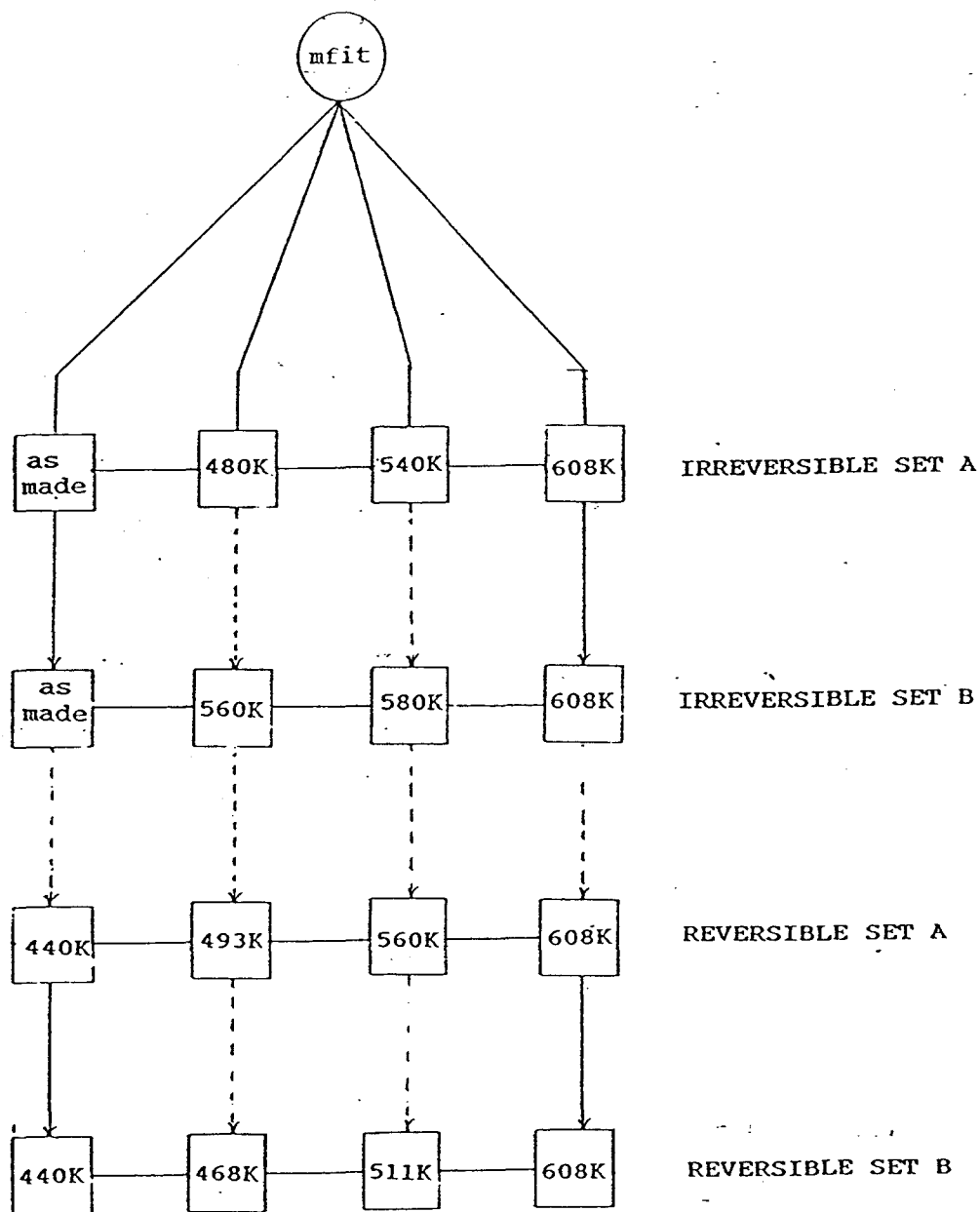


Fig. 4.11 Flowchart showing the order in which the Fourier filtered first shell Ni K EXAFS of $\text{Pd}_{40}\text{Ni}_{40}\text{P}_{20}$ samples measured at 300 K have been fitted. Solid arrows represent samples being transferred from the previous set of fits, and dashed arrows represent new files added.

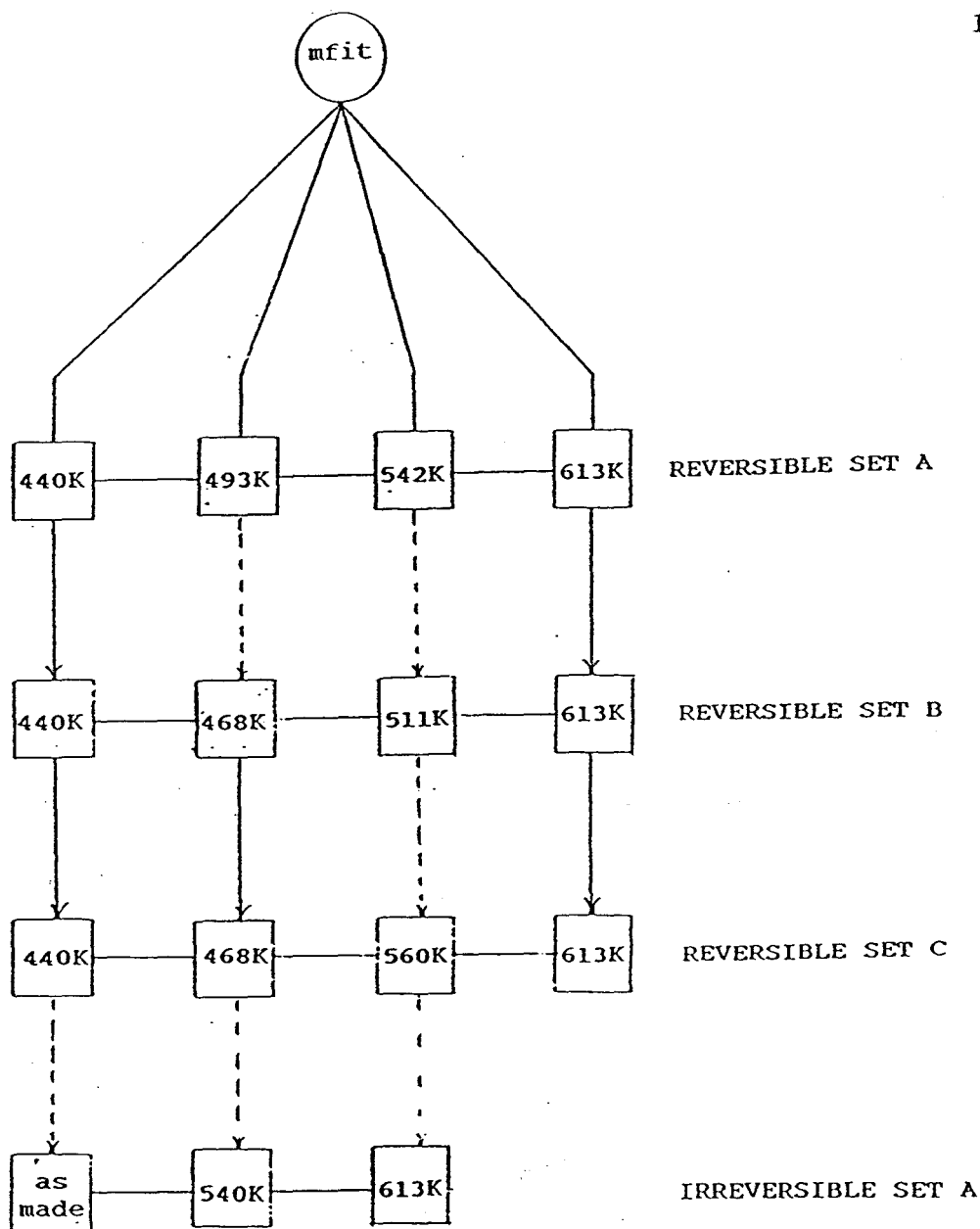


Fig. 4.12 Flowchart showing the order in which the Fourier filtered first shell Ni K EXAFS of $\text{Pd}_{40}\text{Ni}_{40}\text{P}_{20}$ samples measured at 77 K have been fitted. Solid arrows represent samples being transferred from the previous set of fits, and dashed arrows represent new files added.

The S values for irreversible and reversible annealed samples measured at 77 K were also monitored for sensitivity to variations of R and DW in a manner similar to that outlined above. Although the differences in S are not shown here, it was found that the R and DW values for all 3 components have an effect on the fitting, in contrast to the 300 K data sets where R(Ni-Ni) and DW(Ni) had negligible effect. In this case, the ΔE_0 parameter for all components was fixed to zero, and the N for each component was allowed to vary independently at all times during the fitting processes for reasons stated above. Thus, all components were allowed to vary independently with the exception of ΔE_0 being fixed to zero (see appendix. I,II).

Appendix I shows the rest of results obtained from fitting of the irreversible annealed samples measured at 300 K. Appendix II shows the corresponding results for reversible samples measured at 300 K. Appendix III and IV show results obtained from irreversible and reversible annealed samples measured at 77 K.

4.10 Presentation and Discussion of the Results of Multiple Fit Analysis of the Pd₄₀Ni₄₀P₂₀ Irreversibly and Reversibly Annealed Samples

The structural parameters derived from the fitting procedure described above have been plotted as a function of annealing temperature in order to investigate if trends exist in the results. If so, do these trends give information pertaining to the physical changes occurring in the structure of the sample with irreversible and

reversible relaxation? That is, can the answers of the curve fit analysis (as so far carried out) give information as to the validity of the analysis? If the fit results are considered meaningful, what information can be obtained from the trend lines concerning the changes that occur about the Ni atom with annealing? The success of answering these questions may: (1) assure other graduate students and/or research scientists that the fitting procedure is one that can be followed to give meaningful results, and of course (2) give an advancement to the knowledge of the Pd-Ni-P system.

Figures 4.13-4.15 show the linear trends for the irreversible samples, and figures 4.16-4.18 illustrate trends for the reversible samples. All plots summarise these results from both measurement temperatures (77 K and 300 K). The fit parameters $R(\text{Ni-X})$, $N(X)$, $DW(X)$ where $X = \text{Ni, Pd, P}$ are plotted as a function of annealing temperature. In all plots, triangle, circle, and square symbols represent values obtained from the fitting procedure for the Ni, Pd, and P components respectively. Open symbols represent fitting of the first set of four samples (set A) and closed symbols represent fitting of the second set of four samples (set B). The 560 K reversibly annealed sample measured at 77 K is shown with the symbol " " (4.16-4.18) to help distinguish this sample which was added to the previous three samples which were fit.

For the irreversibly annealed samples, measured at 300K, figure 4.13 b shows variations of $R(\text{Ni-Pd})$ and $R(\text{Ni-P})$, figure 4.14 b shows variations of

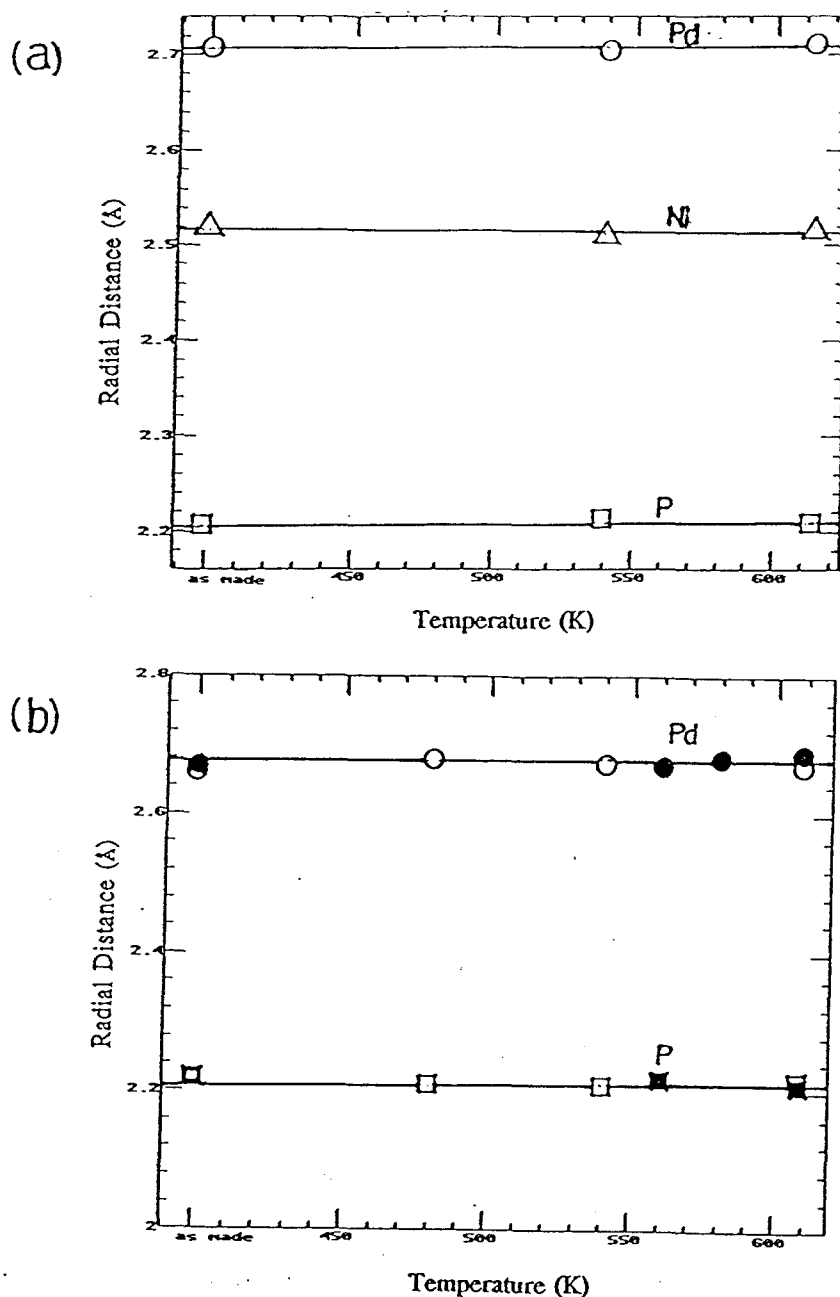


Fig. 4.13 Radial distances versus annealing temperature derived from Ni K EXAFS of various irreversibly annealed $\text{Pd}_{40}\text{Ni}_{40}\text{P}_{20}$ samples measured at (a) 77 K, (b) 300 K; circles, triangles, and squares represent backscattering components, Pd, Ni and P respectively. Open symbols represent fitting of the first set of four samples (set A), and closed symbols represent the second set of four samples (set B).

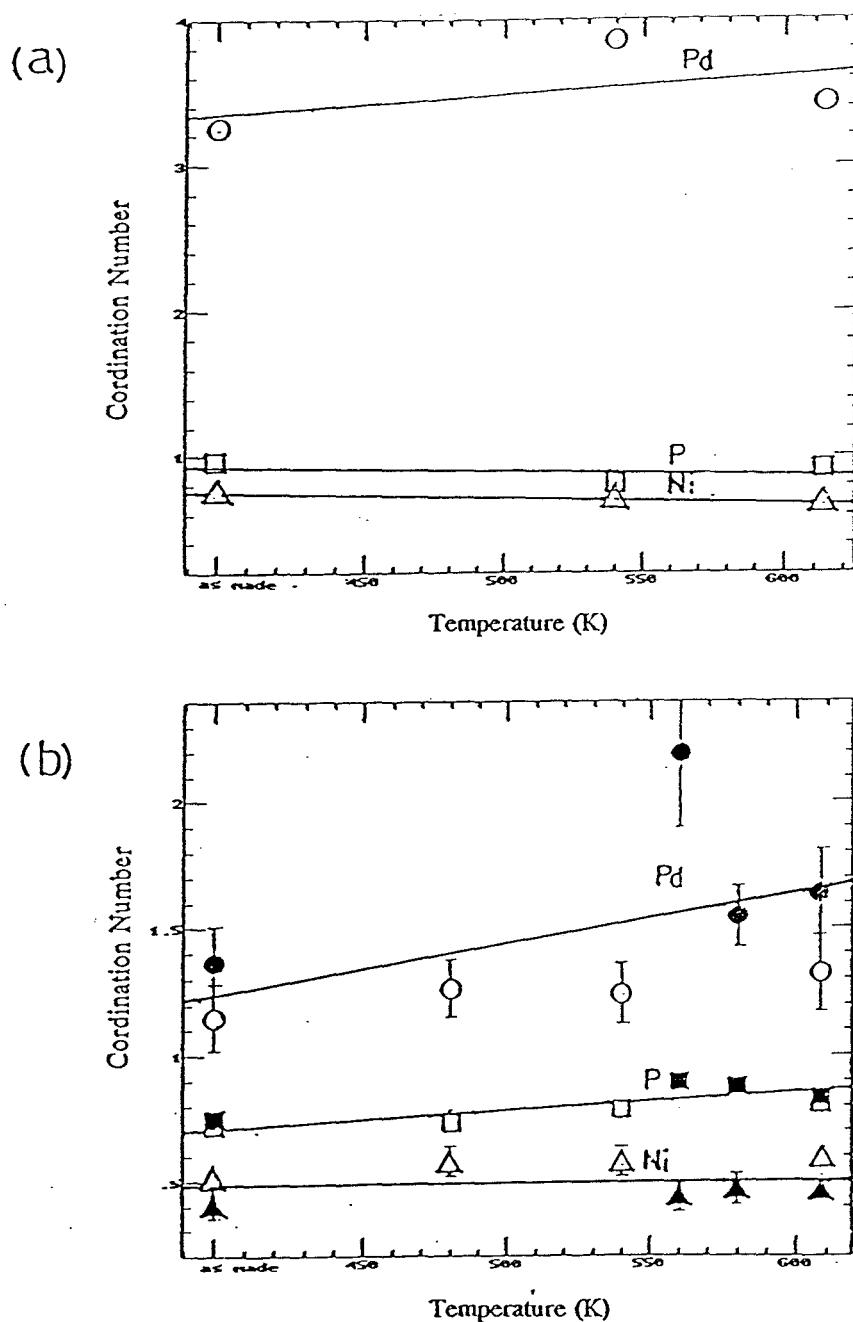


Fig. 4.14 Coordination numbers versus annealing temperature derived from Ni K EXAFS of various irreversibly annealed $\text{Pd}_{40}\text{Ni}_{40}\text{P}_{20}$ samples measured at (a) 77 K (b) 300 K; circles, triangles, and squares represent backscattering components, Pd, Ni and P respectively. Open symbols represent fitting of the first set of four samples (set A), and closed symbols represent the second set of four samples (set B). 20% error bars are shown.

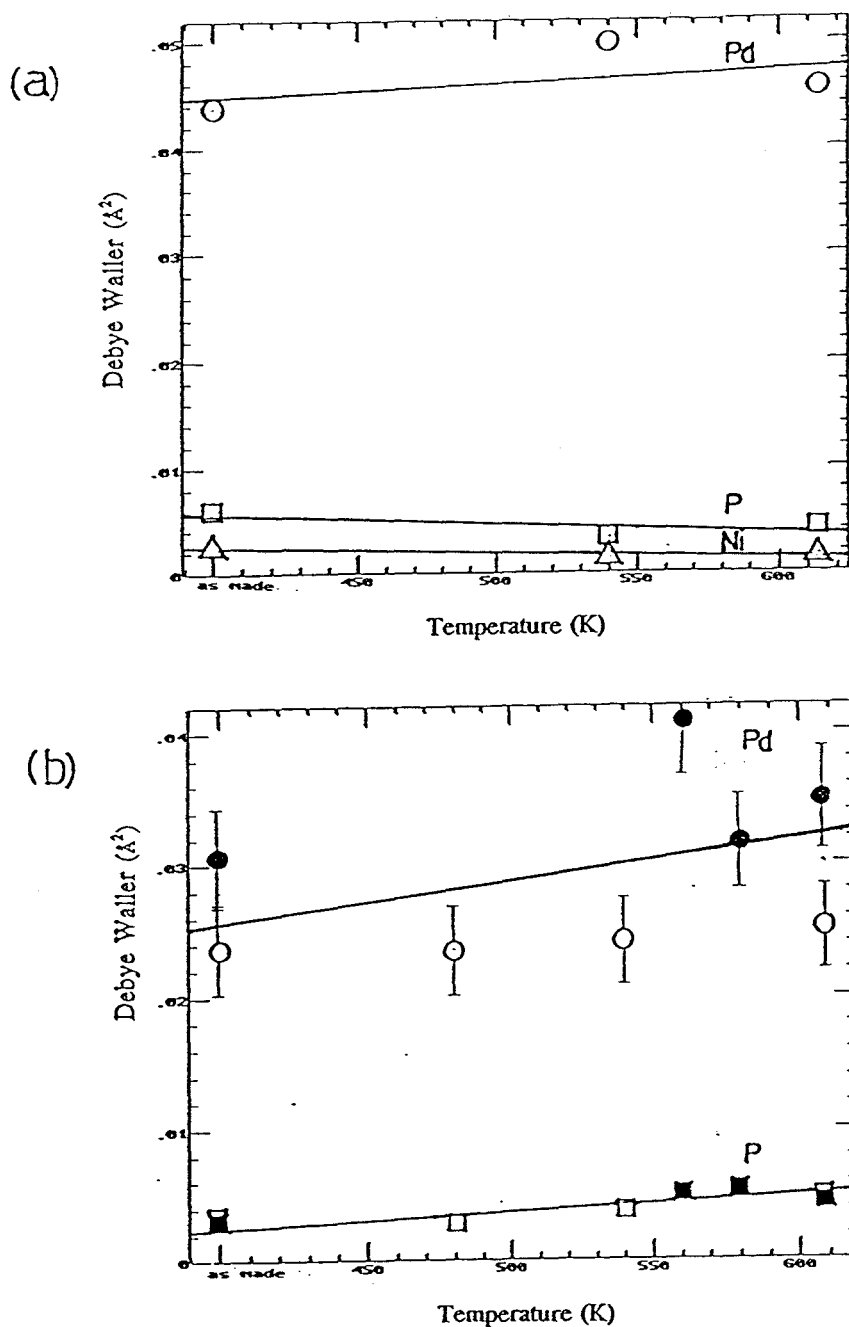


Fig. 4.15 Debye Waller factors versus annealing temperature derived from Ni K EXAFS of various irreversibly annealed $\text{Pd}_{40}\text{Ni}_{40}\text{P}_{20}$ samples measured at (a) 77 K (b) 300 K; circles, triangles, and squares represent backscattering components, Pd, Ni and P respectively. Open symbols represent fitting of the first set of four samples (set A), and closed symbols represent the second set of four samples (set B). Error bars are taken from the reproducibility in the case of multiple analysis of the same file.

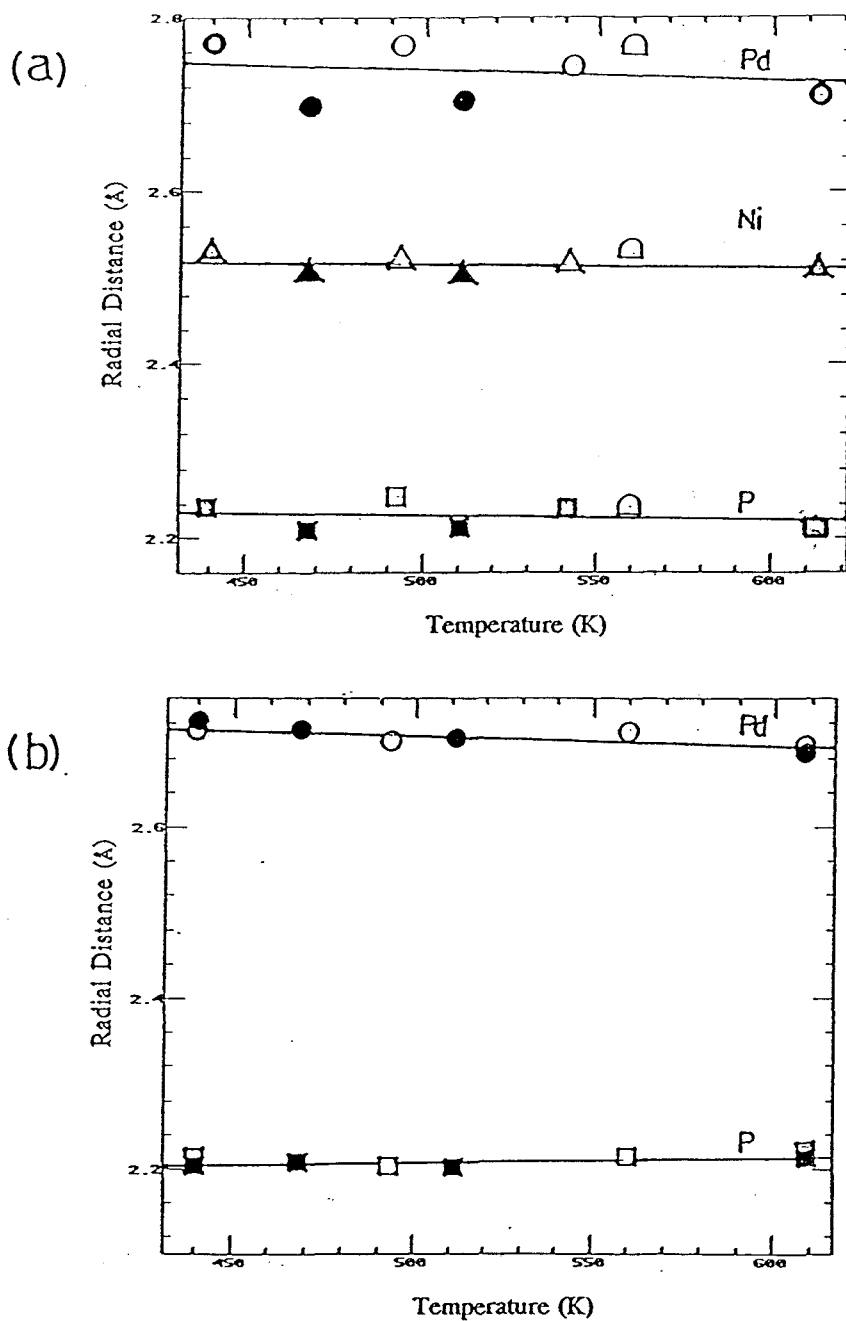


Fig. 4.16 Radial distances versus annealing temperature derived from Ni K EXAFS of various reversibly annealed $\text{Pd}_{40}\text{Ni}_{40}\text{P}_{20}$ samples measured at (a) 77 K (b) 300 K; circles, triangles, and squares represent backscattering components, Pd, Ni and P respectively. Open symbols represent fitting of the first set of four samples (set A), and closed symbols represent the second set of four samples (set B).

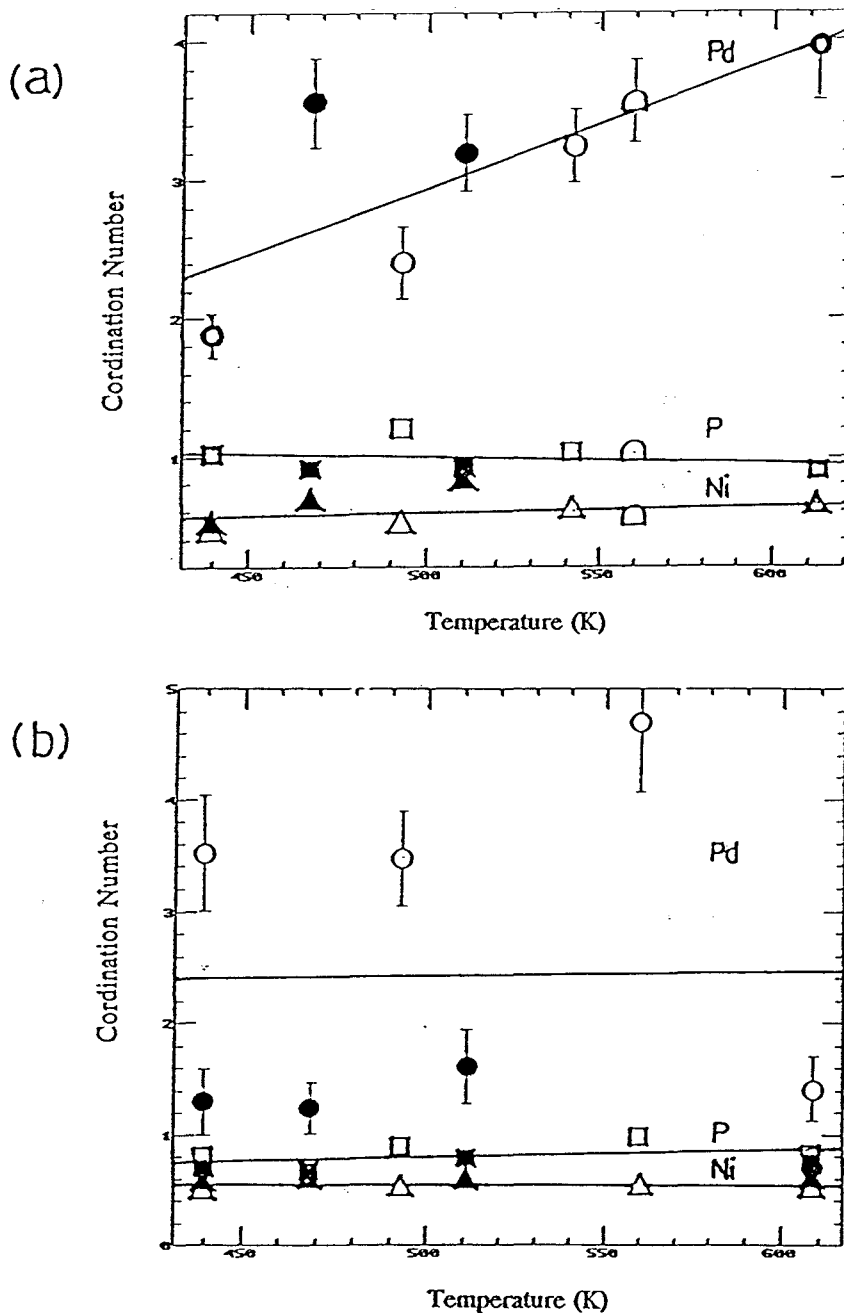


Fig. 4.17 Coordination numbers versus annealing temperature derived from Ni K EXAFS of various reversibly annealed $\text{Pd}_{40}\text{Ni}_{40}\text{P}_{20}$ samples measured at (a) 77 K (b) 300 K; circles, triangles, and squares represent backscattering components, Pd, Ni and P respectively. Open symbols represent fitting of the first set of four samples (set A), and closed symbols represent the second set of four samples (set B). 20% error bars are shown.

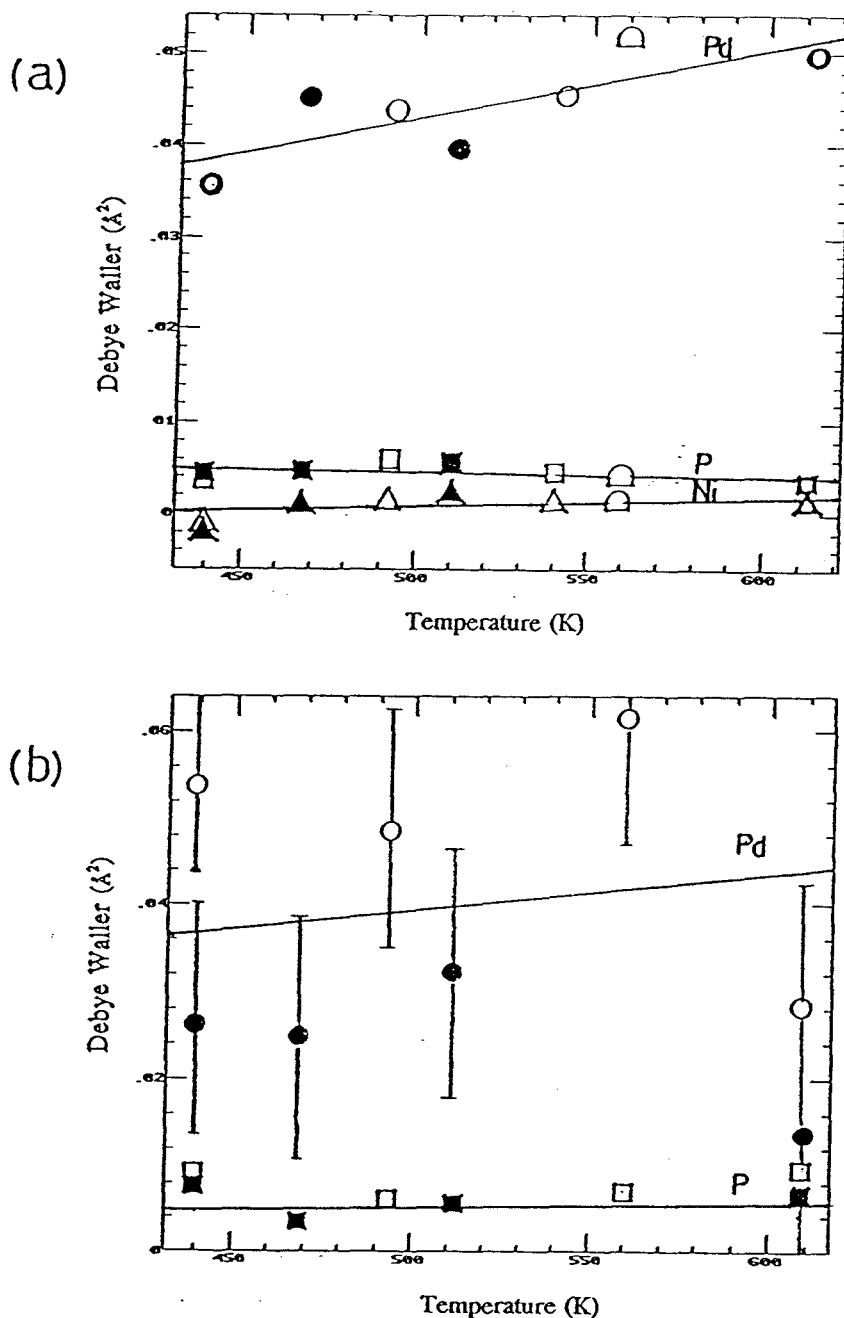


Fig. 4.18 Debye Waller factor versus annealing temperature derived from Ni K EXAFS of various reversibly annealed $\text{Pd}_{40}\text{Ni}_{40}\text{P}_{20}$ samples measured at (a) 77 K (b) 300 K; circles, triangles, and squares represent backscattering components, Pd, Ni and P respectively. Open symbols represent fitting of the first set of four samples (set A), and closed symbols represent the second set of four samples (set B). Error bars are taken from the reproducibility in the case of multiple analysis of the same file measure of uncertainty of overlapping file.

coordination number $N(\text{Ni})$, $N(\text{Pd})$ and $N(\text{P})$, and figure 4.15 b shows variations of $DW(\text{Pd})$ and $DW(\text{P})$ as a function of annealing temperature. Figures 4.16 b-4.18b show the corresponding quantities for the reversibly annealed samples. Plots for the Ni-Ni distance were not made because the values for each sample were required to be the same in the fitting procedure. Similarly plots for $DW(\text{Ni})$ were not made due to the insensitivity of the fit quality to this parameter.

Table 4.4 gives the slopes, intercepts, and correlation values for linear least square fits to all parameter plots for 300 K data (irreversible and reversible). Table 4.5 gives the slopes, intercepts, and correlation values for linear least square fits to all parameter plots (irreversible and reversible samples measured at 77 K.) The uncertainty values, discussed in section 4.9, were used as error bars on the plots of R and DW as a function of temperature (figures 4.15 b, 4.18 b).

(a) Irreversible Annealing

Figure 4.13 shows trends in R as a function of annealing temperature derived from spectra measured at 77 K and 300 K. Although $R(\text{Ni-Ni})$ was not optimized individually for each sample measured at 300 K, it was optimized to give the best single value for a set of four files. The value of $R(\text{Ni-Ni})$ in set A = 2.497 Å and set B = 2.495 Å (see fig. 4.11 to identify overlapping files). Figure 4.13 shows that there are similar trends in radial distances in data recorded at two measurement temperatures. A slight increase in $R(\text{Ni-Pd})$ and $R(\text{Ni-P})$ is observed with annealing

Table 4.4 Slopes, intercepts, and correlation values for the irreversible and reversible least square plots. Samples measured at 300 K.

Irreversible Samples	slope (10.E-4)	intercept	correlation values
R(NI-Pd)	0.25	2.66	.19
R(Ni-P)	0.27	2.20	.58
N(Ni)	0.83	0.45	.10
N(Pd)	20.14	0.43	.42
N(P)	7.45	0.41	.80
DW(Pd)	0.31	0.01	.40
DW(P)	0.13	0.00	.86
Reversible Samples			
R(Ni-Pd)	-1.17	2.77	-.71
R(Ni-P)	0.43	2.19	.51
N(Ni)	0.35	0.56	-.06
N(Pd)	3.96	2.24	.02
N(P)	6.15	0.49	.34
DW(Pd)	0.41	0.02	.19
DW(P)	0.04	0.00	.20

Table 4.5 Slopes, intercepts, and correlation values for the irreversible and reversible least square plots. Samples measured at 77 K.

Irreversible Samples	slope (10E-4)	intercept	correlation values
R(Ni-Ni)	-0.20	2.52	-0.36
R(Ni-Pd)	0.04	2.71	0.14
R(Ni-P)	0.23	2.20	0.70
N(Ni)	-3.66	0.90	-0.99
N(Pd)	13.45	2.80	0.48
N(P)	-2.84	1.04	-0.40
DW(Ni)	-0.05	0.00	-0.90
DW(Pd)	0.12	0.04	0.43
DW(P)	-0.08	0.01	-0.77
Reversible Samples			
R(Ni-Ni)	-0.28	2.53	-0.15
R(Ni-Pd)	-1.23	2.80	-0.22
R(Ni-P)	-0.53	2.25	-0.20
N(Ni)	4.68	0.36	0.22
N(Pd)	92.92	-1.71	0.76
N(P)	-4.59	1.23	-0.25
DW(Ni)	0.08	-0.00	0.45
DW(Pd)	0.75	0.01	0.79
DW(P)	-0.05	0.01	-0.31

at both the measured temperatures. In addition to this $R(\text{Ni-Ni})$ (figure 4.13 a) illustrates a slight decrease with annealing temperature.

The trends in N (fig. 4.14) and DW (fig. 4.15) show some inconsistencies between the results derived at the two measuring temperatures. The 77 K data suggests $N(\text{Ni})$, $N(\text{P})$ decreases with annealing temperature contrary to the trends measured at 300 K which indicate an increase. According to the least square slopes (table 4.4) $N(\text{Ni})$ possesses a slightly greater decrease than $N(\text{P})$ at 77 K. Although in both cases $N(\text{Pd})$ shows an increase, the slopes seem to indicate that there is a greater increase at the lower measured temperature. $N(\text{Pd})$ has the largest value and $N(\text{Ni})$ has the smallest (fig. 4.14 b).

$DW(\text{P})$ and $DW(\text{Ni})$ decrease with annealing temperature which agrees with one's intuition i.e. the irreversible annealing of an amorphous sample should cause ordering and thus a decrease in the disorder should occur. $DW(\text{P})$ increases at 77 K measured temperatures (fig.4.15a) contrary to 300 K measurements (fig. 4.15 b).

(b) Reversible Annealing

Again $R(\text{Ni-Ni})$ was not optimized individually for each sample measured at 300 K, but it was optimized to give the best single value for each set of four files. The value of $R(\text{Ni-Ni})$ is in set A=2.497 Å and set B=2.495 Å (see fig. 4.11 for overlapping files).

$R(\text{Ni-P})$ slightly decreases with annealing temperature (fig. 4.16a) contrary

to the trend observed for 300 K measurements. $R(\text{Ni-Pd})$ decreases at both measuring temperatures. $R(\text{Ni-Ni})$ shows a decrease with annealing.

$N(\text{Pd})$ increases at both measurement temperatures. In terms of the magnitude of change, $N(\text{Pd})$ changes more rapidly with annealing with 300 K measurements (fig. 4.17 b). An increase and decrease is observed for $N(\text{P})$ and $N(\text{Ni})$ for samples measured at 77K, contrary to the trends of the 300 K measurements.

$DW(\text{Ni})$ increases slightly at 77 K (fig. 4.18 a). An increase and decrease is observed for $DW(\text{Pd})$ and $DW(\text{P})$ at both temperatures.

4.11 Discussion and Conclusions

Although the magnitude of the difference plots (sec. 4.8) showed good agreement in most cases with that expected for the $\text{Pd}_{40}\text{Ni}_{40}\text{P}_{20}$ relaxation processes, as discussed in section 4.3, the trend lines for R , N , DW as a function of annealing failed to show similarities between the 77 K and 300 K measured data. Measuring EXAFS at 77 K often gives better quality data and thus should generally give more reliable structural results than measurements at 300 K. However, in this case there is relatively little change between the 77 K and 300 K EXAFS, indicating structural disorder rather than thermal motion dominates the DW term. Thus one would expect the trend lines in the R , N , DW parameters as a function of annealing temperature to

be similar in the 77 K and 300 K data sets. Since the trend lines do not stay the same, this makes one very sceptical of attributing any meaning to the results. In addition, the ratio of coordination number between Ni and Pd obtained from the fitting procedure (0.43) is not consistent with that of 2 deduced from the model A Ni K EXAFS simulations (sec. 4.6). It should be noted that the radial distances derived from MFIT are in reasonable agreement with those assumed in model A simulations while the DW factors are of similar order of magnitude but 2-3 times larger. The disagreement of the MFIT results for the 77 K and 300 K data set analysis as well as between the Ni/Pd N ratios from simulation and MFIT suggests that the analysis is not yet optimized.

Optimization of the fitting procedure is very crucial in order to derive physically meaningful results. Although the procedure used in the fitting (sec. 4.8) seemed to give confidence in achieving an optimized fit, this was not the case. The analysis must be explored to a greater degree using MFIT either by modification to the procedures used in fitting, or by program revision. The work that has been presented in this chapter will hopefully guide further analysis of these data sets. One should try to perform the curve fitting analysis using phase shifts and amplitudes derived from experiment, i.e. from EXAFS of Ni_2P and $\text{Ni}_x\text{Pd}_{1-x}$ alloys since they are better, as shown for the nickel example (sec. 3.4b). If experimental models can not be used it has been shown recently that calculated models from FEFF (Rher et. al RA90) spherical wave model) give better results than McKale's [MV+88].

Once the analysis has been optimized and consistent results from the Ni K edge data has been obtained, the Pd K edge data must be analyzed in a similar manner. One procedure of particular interest is to explore the use of MFIT to *simultaneously* fit 2 Ni K and 2 Pd K EXAFS files. The requirement that $R(\text{Ni-Pd})$ and $DW(\text{Ni-Pd})$ are identical at each edge could provide powerful constraints on the fitting procedure.

Hopefully the combination of partial information about the local structure around each atom (through Ni-K, Pd-K , and eventually P-K EXAFS) will give a more complete picture of the atomic-scale changes which occur during irreversible and reversible relaxation of $\text{Pd}_{40}\text{Ni}_{40}\text{P}_{20}$ metallic glass.

CHAPTER 5

B 1s Near Edge Spectra of Si(B) and Model Compounds

5.1 General Introduction

This chapter gives an introduction to silicon semiconductors, the doping of silicon, and in particular boron doped silicon [Si(B)]. The rest of the chapter discusses the analysis performed on and results obtained from the B 1s electron yield measurements of Si(B). In contrast to the last two chapters, the emphasis here is on near edge features. The spectra were recorded using the Canadian synchrotron radiation facility (CSRF) located at the synchrotron radiation centre in Stoughton, Wisconsin, a U.S. national facility operated by the University of Wisconsin.

5.2 Introduction

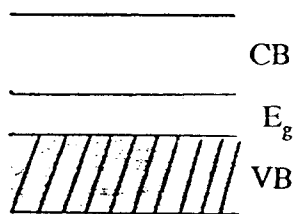
(a) Silicon Semiconductors

A semiconductor is a material having conductivity between that of an insulator and a conductor. The most widely used semiconductor material for application to electronic devices is crystalline silicon [AA71, B79]. Silicon is a group

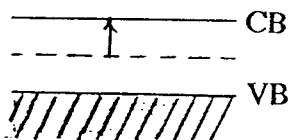
IV element which has four valence electrons available for bonding. In a silicon crystal, each of these electrons combines with an electron from another silicon atom to form a directed covalent bond. This material would be expected to be an insulator according to this simple model, since there are no free electrons. However, enough thermal agitation occurs at ambient temperatures to occasionally release an electron from its bound state, allowing it to move freely through the crystal lattice, thus conducting electricity. This thermal excitation of an electron leaves behind a positively charged region referred to as a hole. The hole also contributes to the electrical conductivity of the crystal since it is mobile like the electron. The mechanism of a moving hole can be described as follows. A bound electron from a nearby Si atom jumps into an electron-deficient region leaving behind a positive hole. Therefore, the conduction of a semiconductor involves the motion of electrons and holes in opposite directions. A more detailed discussion can be found elsewhere [AA71, G87].

(b) Doping of Silicon Semiconductors

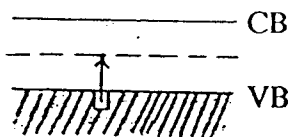
A convenient way of describing the electrical properties of a solid material is in terms of band structure. The electrons in a crystalline solid are constrained to have energies that lie in a number of energy bands. It is the way in which these bands are filled, and how they are distributed on an energy scale, that determines the electronic properties of the material. Figure 5.1a shows the simplified one dimensional band



(a)



(b)



(c)

Fig. 5.1 Depicting in (a) the simplified one dimensional band structure of a semiconductor having a narrow band gap (E_g) (b) an n-type semiconductor doped with a Group V element, and (c) p-type semiconductor doped with a Group III element. CB and VB represent the conduction and valence bands respectively. The arrows represent electronic transitions from (b) and to (c) the doping levels.

structure of a semiconductor. The rather narrow band gap (E_g) characteristic of these materials allows some electrons to be thermally excited from the filled valence band to the vacant conduction band. The electrons are immobile while they are in the valence band, but immediately when excited to the conduction band, they are free to move in response to an electric field.

The conductivity of a silicon crystal can be greatly increased by introducing a tiny controlled amount of an impurity into the crystal. This process is referred to as doping [G87]. Usually, a silicon semiconductor is doped with group V or III elements. When an atom of group V replaces a silicon atom in its lattice, an additional valence electron is introduced into the structure. Only a small amount of thermal energy is needed to free this electron for conduction. This process is illustrated in figure 5.1b. This type of semiconductor is called an n-type (negative type) because the electrons are the majority carriers of current. Positive holes still exist as in the undoped crystal (associated with the silicon atoms) but they are a lot less in number with respect to electrons. Therefore holes are minority carriers in n-type semiconductors.

A p-type semiconductor is formed when silicon is doped with electron deficient atoms (group III elements) which contains only three valence electrons (fig. 5.1c). In this case, positive holes are introduced when electrons from adjoining silicon atoms jump to the vacant orbital associated with the impurity. As a result the majority carrier is positive (holes). Since the positive holes are less mobile than free

electrons, the conductivity of p-type semiconductors is less than that of n-type.

This chapter presents the results of an X-ray absorption study performed on a p-type semiconductor, in particular boron doped silicon. The element specific character of XAS makes it ideally suited to explore electronic and geometric structure around dopants in semiconductors. Here XANES rather than EXAFS was used to obtain information.

(c) Boron Doped silicon

Recently, many new device structures have been proposed, which are based on the premise that molecular beam epitaxy (MBE) can precisely control the uniformity and distribution of dopants over exceedingly small dimensions [D86, P86]. However, for the case of silicon MBE [B85], problems such as surface segregation, low incorporation probabilities, and clustering of the dopants has hindered progress [KB88]. In principle, boron (incorporated by co-evaporation using sources ranging from elemental boron [KLP84], to boron-doped silicon [OA86] to HBO₂ [THA87, THA88] to B₂O₃ [AT85, FRW86, FWR88, JW+88]), would seem an obvious choice as the p-type dopant because of its lower ionization energy and higher solid solubility. However, recent studies suggest significant redistribution problems [TP+88].

Models of the chemical reactions occurring during boron doping of MBE layers with B₂O₃ have been proposed [AT85, FWR88]. Essentially, adsorbed B₂O₃ reacts with incoming Si to decompose to B and Si_xO_y complexes. Further interaction

with Si produces SiO which desorbs above a certain temperature. Incomplete reduction of SiO₂ to SiO at lower growth temperatures can lead to oxygen incorporation into the growing lattice. The thermodynamics of oxygen incorporation has been worked out in detail by Tuppen et al. [TP+88] and was shown to correspond well with experimental findings.

Secondary ion mass spectrometry (SIMS) and electrochemical capacitance-voltage profiling (eCV) have been used by Jackman et al. [JH+88, TP+88] to study the effect of substrate temperature on the boron incorporated by co-evaporation of B₂O₃. This study clearly demonstrated significant re-distribution and clustering of boron at growth temperatures above 700 C [JH+88]. As the substrate temperature was lowered, it was found that one could obtain abrupt interfaces and layers with electrical activity far in excess of the solubility limit of boron in Si, but that there was significant oxygen incorporation (as high as 1.5 times the amount of boron). The temperature dependence of the oxygen-to-boron ratio in both highly and lightly doped samples agrees fairly well with the thermodynamic model of Tuppen et al. [TP+88], although this model does not comment on any interaction between the oxygen and the substitutional boron. In addition, post-growth diffusion of the multi-layers showed a strong dependence on the original growth temperature.

Obviously the chemical state and possible role of the oxygen in the electrical activity and boron diffusion are important questions to address. Techniques such as Fourier transform infrared spectroscopy [O89] and Raman scattering [WSW87] have

not shown any evidence for B-O-Si complexes but it is difficult to ascertain whether the negative results are related to the absence of such complexes or simply insufficient sensitivity. X-ray absorption near edge spectroscopy can provide detailed information on local geometric and electronic structure about selected atoms. The sensitivity of X-ray absorption to local structure is particularly valuable for probing the character of point defects, about which most other techniques can provide relatively little information.

Core excitation spectroscopy is a spatially localized probe of unoccupied density of states in the region of the core excited atom. For specific reasons related to the preferred bonding modes of boron, B K-shell (1s) spectra turn out to be a remarkably effective tool for identifying boron local environments. In many boron compounds (such as BF_3 and B_2O_3) the B atom is trigonally coordinated and there is a compact empty B $2p_z$ orbital. Electric dipole B $1s \rightarrow \text{B } 2p_z$ excitations occur at low energy and are particularly sharp and intense. On the other hand, there are other boron environments, such as the icosahedra of elemental boron or the tetrahedral substitutional site of boron in a Si lattice, in which each boron atom is coordinated by four or more other atoms. In these structures the empty B $2p$ density is distributed over a wider range of energies so that the B $1s$ spectra of boron in these environments are not expected to exhibit the sharp, low energy spike characteristic of trigonal environments.

The idea of using the presence or absence of a low energy B $1s \rightarrow B 2p_z$ to distinguish trigonal and non-trigonal environments has been outlined previously by K.H. Hallmeier et al. [HS+81, SM+83], who performed electron yield measurements of the B $1s$ spectra of a range of boron-containing compounds. This work shows how this concept can be a very useful tool for studying boron dopants in semiconductors.

5.3 EHT Procedures

Although the work of Hallmeier et al. [HS+81, SM+83] convincingly showed that B $1s$ spectra are sensitive to variations in local boron geometry for their set of samples, the spectral shapes expected in Si(B) were explored via calculation (EHT) and experimental studies of model compounds which were a better match to the system. In principle a wide range of quantum mechanical calculations could be used to explore the relevant aspects of the unoccupied electronic structure. The intent of the calculations is to explore the coarse features of the spectroscopy but not necessarily to reproduce fine details of either intensity or position for each spectrum. For this purpose, the semi-empirical extended Hückel theory (EHT) [MV+72] and a one-electron frozen orbital approximation is adequate. The eigenvalues of unoccupied molecular orbitals are assumed to approximate experimental term values ($T=IP-E$). In order to correct for the strong influence of the core hole on orbital shapes and

energies, the calculations relating to B 1s spectral features have been carried out using the equivalent ionic core virtual orbital (EICVOM) approximation [RS+76]. In this procedure one calculates the molecular orbital structure of the species in which the core excited atom (boron) is replaced by the atom of one higher atomic number (carbon) and, in addition, increases the total charge of the system by 1 to account for the reorganisation associated with excitation. For all cases except those involving B-Si modelling the atomic integral parameters were the default values in the Hückel program. In B-Si complexes only the Si 3s and 3p orbitals were used in the basis set for Si since Si 3d orbitals were found to produce an enormous amount of high energy structure which, on the basis of comparison with experiment, was deemed to be unrealistic.

The values of the energies, coefficients and widths for all species as well as the (non-optimised) geometric parameters used in the calculations are shown in table 5.1. For the well-defined molecules and molecular ions (BF_3 , BF_4^-) experimental geometries were used [B77, HI+83]. For the infinite covalent solids (boron, boron oxide, boric acid [M58], and $\text{Si}(\text{B}_s)$ - boron substitutional in Si [P88]), the immediate local structure of the boron atom was used. All three of the allotropes of elemental boron are composed of B_{12} icosahedra linked at each vertex to other icosahedra. The B_{12} cluster composed of two half-icosahedra has been used to simulate the local environment of a boron atom in elemental boron. The calculation was performed in addition for $\text{B}_{12}\text{H}_{10}$ and $\text{B}_{12}\text{H}_{30}$ clusters where each of the ten exterior boron atoms is

Table 5.1. Geometry, Orbital Energies (ϵ , eV), Band Widths (W , eV), and Intensities ($c^2(C2p)$) for B 1s Excited States of BF_3 , BF_4^- , $B(OH)_3$, BO_3 , B_{12} , and BSi_4 from extended Hückel theory.

A. Geometry

Molecule:	BF_3 (a)	BF_4^- (b)	$BO_3, B(OH)_3$ (c)	B_{12} (d)	BSi_4 (e)
symmetry	D_{3h}	T_d	D_{3h}	D_{5h}	T_d
bond length (Å)	1.31	1.38	1.36 (B-O) 1.03 (O-H)	1.80 B-B _i 1.72 (B-B)	2.35 (B-Si)
bond angle	120°	109.5°	105° BOH 120° OBO	72° BBB _i 121.7° BBB	109.5° (SiBSi)

B. Results of EHT Calculations

BF_3			$B(OH)_3$			B_{12}			BSi_4		
ϵ	W	c^2	ϵ	W	c^2	ϵ	W	c^2	ϵ	W	c^2
-9.1	0.7	1.0	-8.9	1.6	0.94	-8.8	2.0	0.02	-9.1	4.0	0.08(x3)
11.9	3.8	1.6(x2)	-1.4	8.0	0.26(x2)	-8.7	2.0	0.03	-7.1	4.0	0.07(x3)
			10.7	12.	1.31(x2)	-6.9	2.0	0.03	-6.2	4.0	0.01(x3)
						-3.4	6.0	0.50	-5.4	6.0	0.03(x3)
						-2.8	6.0	0.68	0.4	12.0	0.76(x3)
						-0.6	6.0	0.14			
						2.5	8.0	0.05			
						4.7	8.0	1.19			
						0.08	4.0	0.06			
						14.5	8.0	0.24			
						17.4	8.0	0.17			
						19.8	10.0	0.05			

a. geometry from ref [B77].

b. geometry from ref. [HI+83].

c. geometry from ref. [M67]

d. ref [M67]. Boron forms crystal structures consisting of various arrangements of icosahedra connected by B-B bonds. The common unit is taken to be a B_{12} cluster consisting of two $B(B_5)$ pentagonal based pyramids (B-B_i=1.80, BBB_i= 72°) connected by a 1.72 Å B-B bond.

e. B-Si as in bulk Si [P58].

capped by one or three hydrogen atoms. Similarly the EHT calculations for Si(B_s) were carried out on three geometries: BSi₄, a B(SiH₃)₄ hydrogen capped cluster and a BSi₁₆ cluster. In these cases the results were generally similar although the inclusion of additional atoms (H or Si) at the periphery of the cluster generally reduced the amount of low energy structure in the predicted spectra. Only the 'bare' B₁₂ and BSi₄ results are presented here.

In the general case the intensities of one-electron electronic transitions depend on the symmetry and spatial distribution of the initial and final orbitals. Since core excitation is localized on a particular atom the transition intensities can be related to LCAO-MO coefficients, if certain approximations are made. In an LCAO description the optical oscillator strength (*f*) of an electric dipole B 1s excitation to a non degenerate MO (*σ*) may be expressed as [LA85]:

$$f_{\sigma} = 0.175 \cdot E \cdot \sum |c_{ha}^{\sigma} \langle \chi_{ha} | \underline{\mu} | \chi_{B1s} \rangle|^2 \quad (5-1)$$

where χ_{B1s} is the B 1s atomic orbital; c_{ha}^{σ} is the coefficient of χ_{ha} , atomic orbital *a* on atom *h* in the optical orbital denoted by *σ*; $\underline{\mu} = e\mathbf{r}$ is the dipole moment; *E* is the transition energy in eV. In this expression terms of the form $|c_{B2p}^{\sigma} \langle \chi_{B2p} | \underline{\mu} | \chi_{B1s} \rangle|^2$ will dominate the observed B 1s spectrum since empty 2p orbitals on the core excited boron have the greatest dipole overlap with the B 1s orbital. Thus the relative intensity of B 1s excitation to each unoccupied molecular orbital is approximated by the sum of

the squares of the coefficients of the 2p AO at the core excited boron in that MO. In the EICVOM approach this implies that the relative intensity of the transitions are given by $\sum c^2(C2p)$ since core-excited boron is represented by carbon in the $(Z+1)^+$ species for which the orbital structure is actually calculated. In order to better visualize the results of the calculations simulated spectra have been generated by summing gaussians of position equal to the eigenvalue, area equal to $\sum c^2_{C2p}$, and of width (W) estimated from the widths of corresponding experimental features. The values of the energies and coefficients for the unoccupied MOs and the assumed spectral widths are listed in table 1 for the plotted EHT-simulations.

5.4 The I_0 Normalization Problem

The incident photon flux (I_0) signal was not appropriate for the present study since it contained artifacts at the B 1s edge region, perhaps due to boron contamination on the gold mesh (see sec. 2.5b). It is critical that the I_0 signal does not contain structure in the spectral region of interest, particularly when attempting to study dilute systems. A common alternative I_0 monitor is measurement of the electron yield signal from a substrate free of the element of interest. The photoionization sample current of a Si wafer which had no boron doping was explored, as an accurate measure of the combination of the incident flux and the underlying Si 2p extended X-ray absorption fine structure (EXAFS) signal. In many ways this is preferable to a

simple I_0 monitor [S88c] since it corrects for the Si 2p EXAFS as well as for variations in the incident photon flux. The single crystal silicon is highly ordered and there is relatively strong Si 2p EXAFS. In practice substrate-I normalization did not work satisfactorily. It was found that the best procedure to analyze measured spectra has been to use the sample current (I) signal without explicit correction for I_0 . The reason for the failure of the clean substrate normalisation procedure is not fully understood. It may indicate that the time delay between measuring Si(B) and clean Si samples exceeded the time scale of changes in shape of the incident flux spectrum.

5.5 B 1s Spectra of Model Compounds

Figure 5.2 compares the extended Hückel simulations of B 1s spectra with the corresponding experimental results for BF_3 (gas) and KBF_4 (solid). The B 1s spectrum of BF_3 was recorded at McMaster by inelastic electron scattering [HB+84, H89, H90]. It is identical to published X-ray absorption spectra of BF_3 [F68, BK74, NAV88]. The B 1s spectrum of KBF_4 was digitized from the X-ray electron yield spectrum of the solid [SM+83]. The B 1s ionization thresholds used to place the BF_3 and KBF_4 spectra on a common term value scale are the experimental values reported in reference SM+83 ($\text{BF}_3 = 202.8$ eV; $\text{KBF}_4 = 199.8$ eV). Both spectra are shown after background subtraction. The EHT calculated term values (table 5.1) and relative

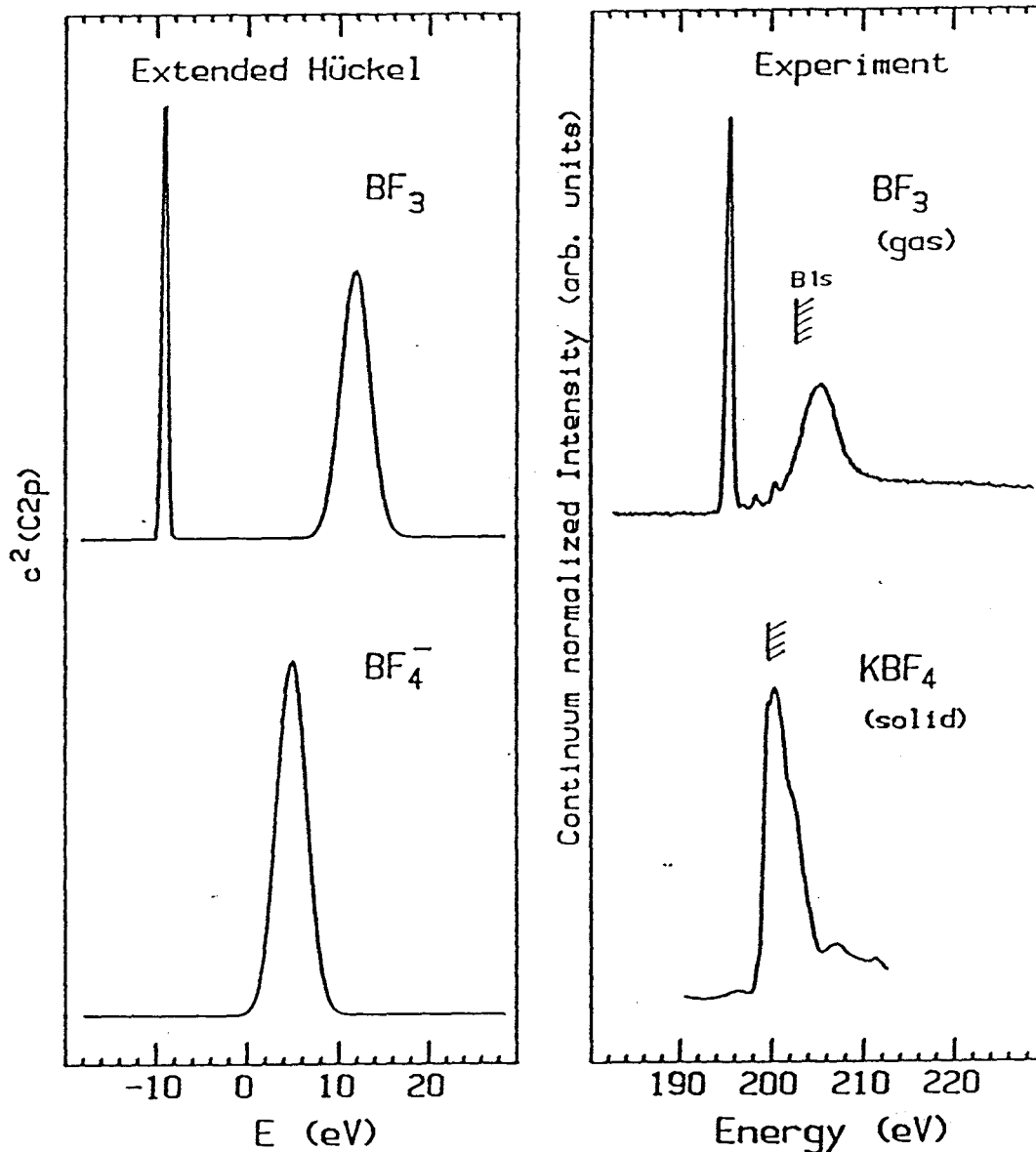


Fig. 5.2 Comparison of the B 1s experimental and calculated spectra for BF_3 (gas) and KBF_4 (solid) [SM+83]. The simulated spectra are derived from eigenvalues and eigenfunctions calculated by extended Hückel theory (EHT) using the equivalent ionic core virtual orbital method (see section 3.1 for details). The inner shell electron energy loss spectrum of BF_3 was obtained using 2.5 keV impact energy and 2° scattering angle. The spectrum of KBF_4 was measured with synchrotron radiation using electron yield detection [SM+83]. The experimental spectra of the model compounds have had a smooth background subtracted. They are plotted on an energy scale relative to their B 1s IP [SM+82].

intensities are in fairly good agreement with experiment. The sharp, intense spike observed in the calculated and experimental spectra of BF_3 is due to the $\text{B } 1s \rightarrow 2p_z$ (π^* , a_1) transition. This feature occurs at -9 eV in both the calculated and experimental spectra. In contrast, neither the calculated nor the experimental B 1s spectrum of KBF_4 exhibit this low energy spike. The absence of this spike can be explained by the fact that the B $2p_z$ orbital is now effectively filled since there are 8 valence electrons around the boron atom in BF_4^- .

The broad feature in the ionization continuum of both BF_3 and KBF_4 is attributed to $\text{B } 1s \rightarrow \sigma^*(\text{B-F})$ transitions. The experimental and calculated energies do not agree as well for the continuum as for the discrete feature. This could be related to the inadequacies of EHT at treating high energy molecular orbitals [LL88]. It is noted here, that in both the experimental and the EHT-simulated spectra the $\text{B } 1s \rightarrow \sigma^*(\text{B-F})$ transition shifts to lower energy in KBF_4 relative to that in BF_3 . This is consistent with the longer B-F bond length in BF_4^- (1.38 Å) than in BF_3 (1.31 Å) according to the well-established correlation of $1s \rightarrow \sigma^*$ energies and bond lengths [SSH84]. The simulated and experimental spectra of BF_4^- contain only one strong feature, that corresponding to the $\text{B } 1s \rightarrow \sigma^*(\text{B-F})_{t_2}$ transition. The weak features observed between the π^* and σ^* features in BF_3 are Rydberg states [F68, K74, NAV88, SM+83]. The fine structure superimposed on the main peak in the KBF_4 spectrum is likely related to multiple scattering from more distant coordination shells.

Figure 5.3 plots the EHT-simulated B 1s spectra of B(OH)_3 , BO_3 , B_{12} and BSi_4 which were derived from the results for the $(Z+1)^+$ molecules calculated in the geometries indicated in table 5.1. The EHT-simulated spectra of B(OH)_3 and BO_3 show a sharp, intense spike at -9 eV which is attributed to B $1s \rightarrow 2p_z$ transitions analogous to that in BF_3 . In each of these compounds each boron atom is trigonally coordinated with oxygen rather than fluorine but the localised empty B 2p state is very similar. At higher energy there is a feature attributable on the basis of orbital composition to B $1s \rightarrow \sigma^*(\text{B-O})$ transitions. In B(OH)_3 there is an additional weak feature around -2 eV which has $\sigma^*(\text{O-H})$ character.

The EHT-simulated spectrum of boron co-ordinated in a non-trigonal local geometry with either boron or silicon is different from that of the trigonally coordinated species, although the difference is less dramatic than in the comparison of BF_3 and BF_4^- . As shown in Fig. 5.3, the EHT-simulated B 1s spectra of B_{12} and BSi_4 consist of a number of relatively weak features between -8 and 10 eV. Since all the spectra in Figure 5.3 are plotted on the same vertical scale, the absence of any sharp low energy spike in the non-trigonal geometries is confirmed. Thus these EHT simulations predict that the B 1s spectra of boron and Si(B)_3 should consist of broad structure over a range of energies but there should not be any significant sharp, low lying structure. This picture is consistent with filling of the B 2p orbitals through more or less complete saturation of the valence shell around non-trigonally coordinated boron.

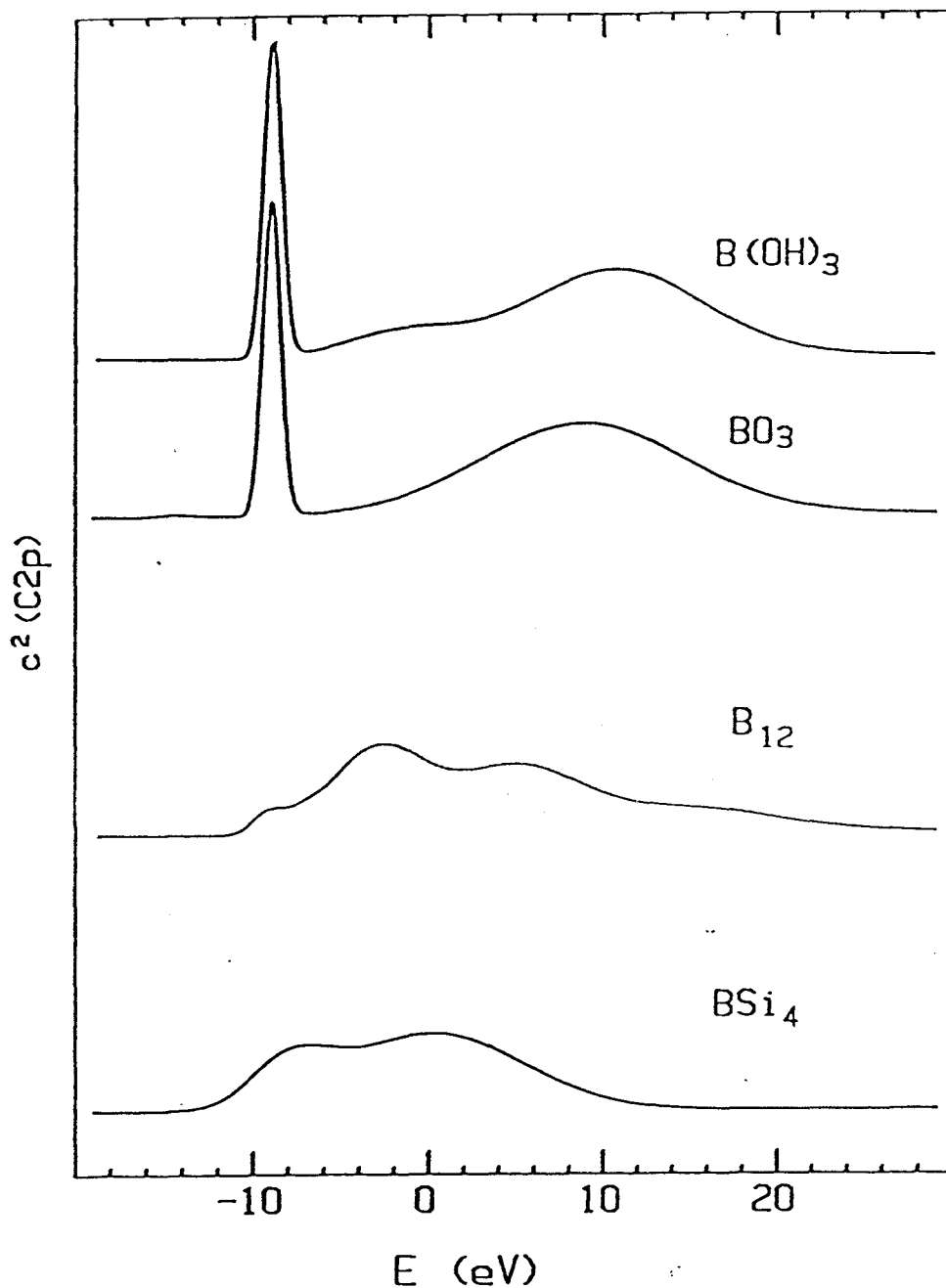


Fig. 5.3 EHT calculation of the B 1s spectra of $B(OH)_3$, BO_3 (simulating B_2O_3), B_{12} (elemental boron) and BSi_4 (substitutional boron in Si). The spectra are constructed from the eigenvalues and eigenfunctions of the equivalent core species, using the sum of the squares of the C 2p coefficients as the area of gaussians of width chosen to match the width of corresponding features in experimental spectra (see table 1 and see section 3.1 for details of geometries used and EHT results).

Experimentally, comparisons of the B 1s spectra of trigonal and non-trigonal complexed boron reveal the same trends. Figure 5.4 plots the electron yield spectra on an absolute energy scale of B(OH)_3 , B_2O_3 , and elemental boron. The spectra of B(OH)_3 and B_2O_3 are somewhat better resolved but otherwise in good agreement with those reported by Hallmeier et al. [SM+83]. The B 1s spectrum of elemental boron has not been reported previously. As expected from their very similar BO_3 trigonal local environment [M67], the spectrum of B_2O_3 is very similar to that of B(OH)_3 . The spectrum of each exhibits a sharp spike at 195 eV, corresponding to the B $1s \rightarrow 2p_z(\pi^*)$ transition, and a broad feature at 202 eV, corresponding to B $1s \rightarrow \sigma^*(\text{B-O})$ transitions. In contrast, the B 1s spectrum of elemental boron does not exhibit a strong low energy spike but rather consists of a series of broad structures spanning a wide energy range. The weak feature around 195 eV may be associated with surface oxide although there are also weak low energy peaks in the EHT simulated spectrum.

Thus both the EHT calculations and the experimental spectra of model compounds (Figs. 5.2-5.4) support the claim that the presence or absence of an intense, sharp peak around 195 eV in a B 1s spectrum can be used to ascertain whether the local environment of boron is trigonal or not. From this calibration work it is clear that, if boron K-shell near edge spectra can be acquired at the dilute concentrations typical of boron doping, then these should be useful in distinguishing tetrahedral substitutional boron dopant sites from other forms in which boron can be

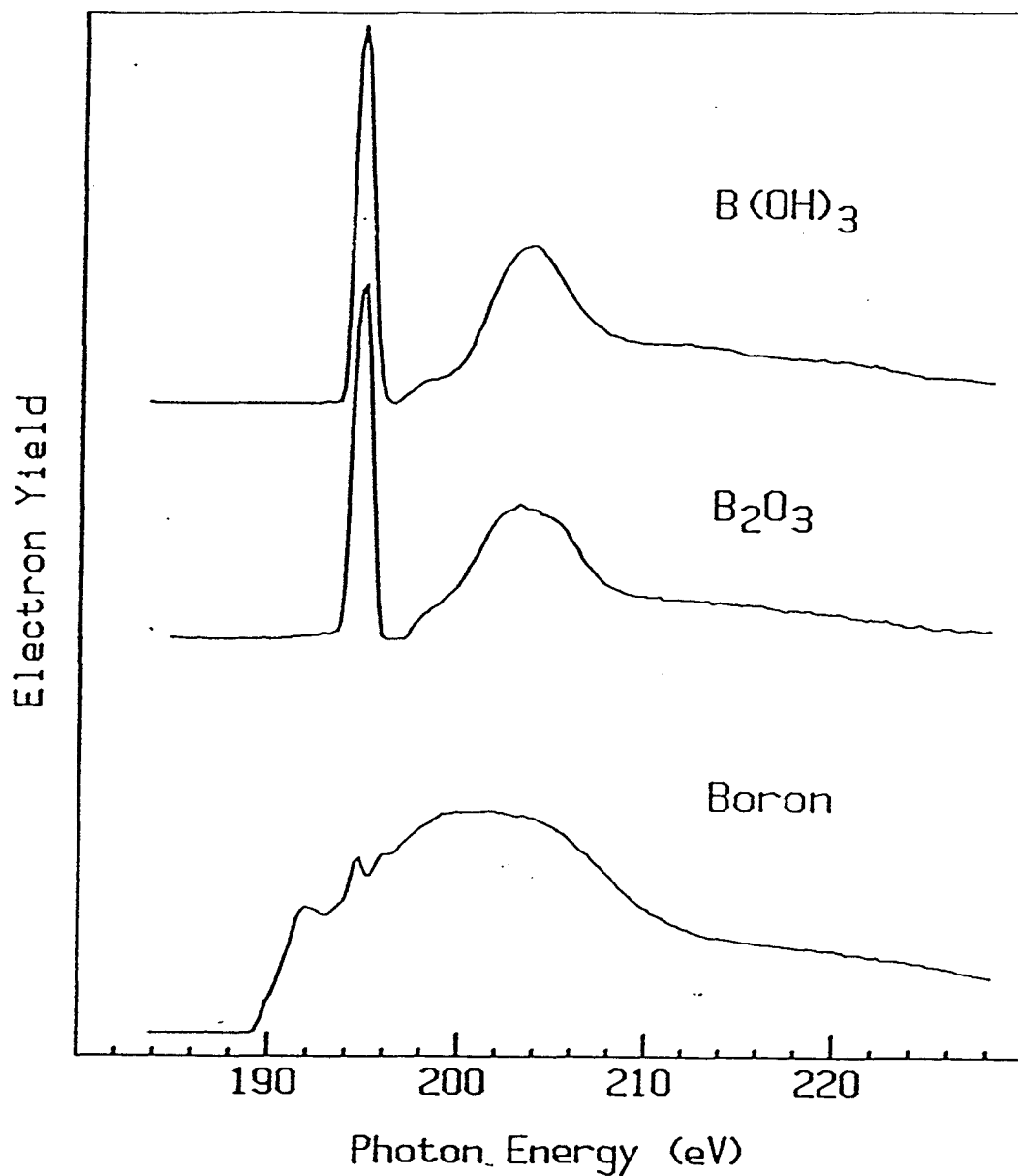


Fig. 5.4 B 1s spectra of $B(OH)_3$, B_2O_3 , and β -rhombohedral boron measured by electron yield detection. The background subtracted spectra have not been corrected for the incident flux intensity (see text for rationalisation).

incorporated into diamond-lattice semiconductors.

5.6 Effect of Etching on Si 2p and B 1s Spectra: Depth Sensitivity of Electron Yield Detection

Background subtracted Si 2p and B 1s electron yield spectra of the as-prepared high-boron sample (#271) are shown in figure 5.5. The spectra recorded before and after HF etching show significant changes in both the Si 2p and B 1s regions. Essentially the same results with regard to the effect of etching were found for all other Si(B) samples studied.

The observation of both Si and SiO₂ related signals at 100 and 108 eV respectively in the Si 2p spectra of the un-etched sample allows an estimation of the depth sensitivity of sample current (electron yield) detection at the B 1s edge. Since the ratio of the intensities of features associated with bulk Si (100 eV) and SiO₂ (108 eV) is approximately 1:1, the depth sensitivity must be of the order of 40 Å, assuming the standard protective oxide of ca. 20 Å thickness. Silicon-oxide growth measurements performed by M. Monita et al. [MO+89] indicate that less than 5 Å of oxide should re-grow during the < 5 minutes that elapsed between HF dip etching and pumpdown.

The B 1s spectrum of the as-made material is reminiscent of that of B(OH)₃ and B₂O₃ (Fig. 5.3) although the broad continuum structure is more complex and the

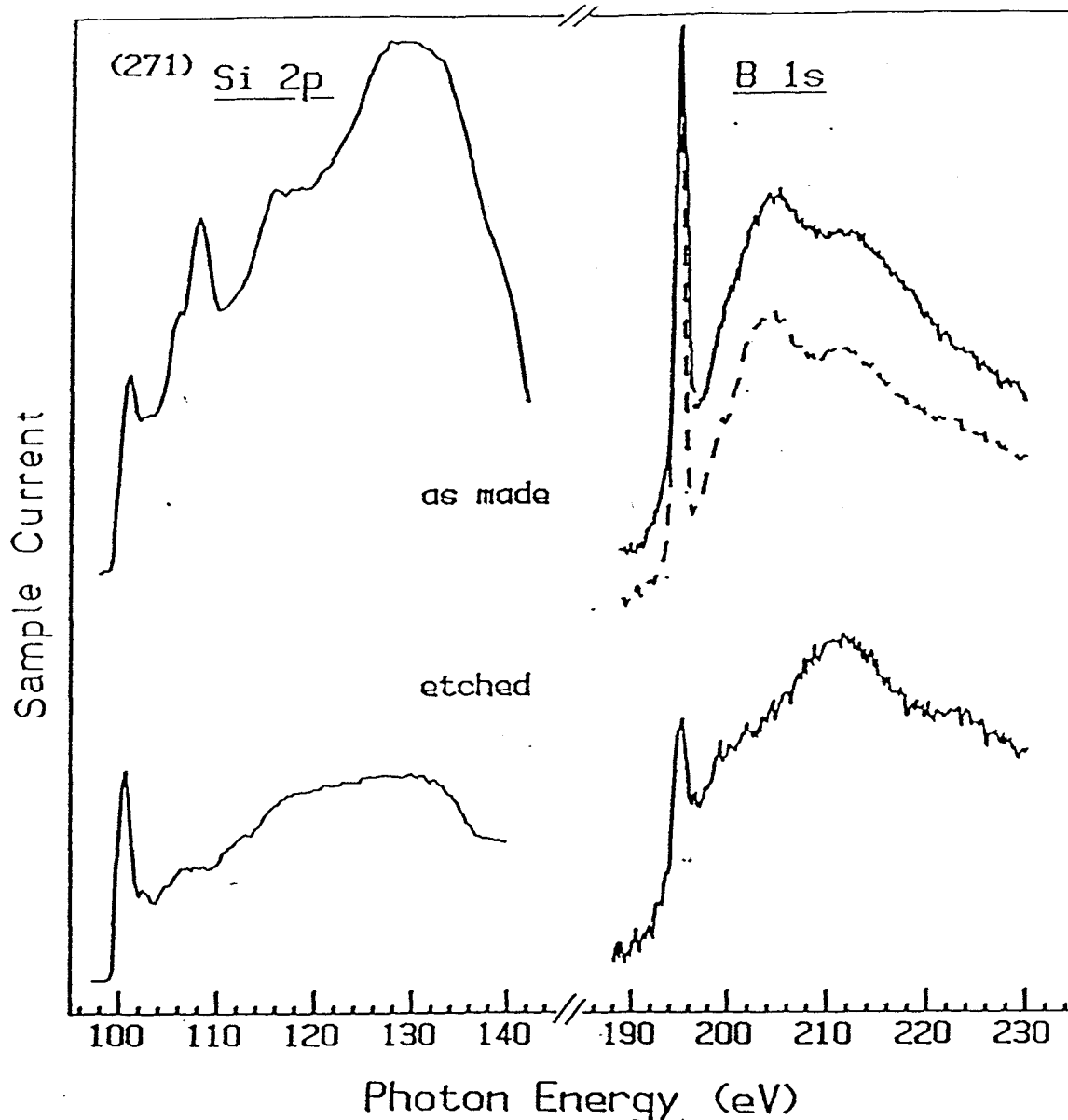


Fig. 5.5 Comparison of the Si 2p and B 1s spectra from the high concentration as-grown sample, (#271, with 3×10^{20} at. cm^{-3} of boron in the outer $0.1 \mu\text{m}$ according to SIMS) before and after etching. The background subtracted spectra have not been corrected for the incident flux. The dashed line indicates a simulation of the B 1s spectrum of the non-etched sample as a weighted sum of the spectrum of the etched sample (40%) and that of B_2O_3 (60%).

sharp peak at 195 eV is less intense. After etching, the intensity of the 195 eV 'oxide' spike in the B 1s spectrum is greatly reduced and the broad maximum at 205 eV disappears. The changes in the B 1s spectra with etching can be explained as follows. In the non-etched sample, the detected signal is produced by photoabsorption at boron both in the bulk and in the surface silicon oxide layer. Thus some of the boron atoms are in an oxygen-rich environment and are likely to have a local structure similar to that in B_2O_3 or $B(OH)_3$. During etching, this highly-oxidized form of boron is removed, hopefully revealing a spectrum representative of the chemical environment of boron in the bulk of the silicon epilayer (but see below). From the retention of a 195 eV spike, albeit weaker than that in the oxide surface layer, it appears that the detected boron after etching may be in the form of some type of BO_x complex where $1 < x < 3$ (see below) - i.e. it differs from the spectrum expected for boron in a tetrahedral substitutional environment, as suggested by the EHT-simulated spectrum of BSi_4 presented in figure 5.3. Alternatively there may be a mix of substitutional tetrahedrally coordinated boron and trigonal oxidised boron contributing to the spectrum observed after etching.

In order to support the interpretation that the boron in the un-etched surface oxide layer is in the form of a BO_y complex where $y > x$, linear combinations of the B 1s spectrum of B_2O_3 and that of the etched (3×10^{20} at.cm⁻³) material were investigated. At a ratio of 6:4, an excellent match to the B 1s spectrum of the as-grown, non-etched material is observed (see dashed line in fig. 5.5). The fact that the estimated

BO_y/BO_x ratio is similar to the relative contributions of the silicon oxide and bulk silicon to the Si 2p spectrum supports our interpretation of the chemical forms of boron contributing to the B 1s spectrum of the non-etched sample.

5.7 Effect of Annealing on the B 1s spectra and the B Environment

Figure 5.6 shows the B 1s spectra of the as-grown and annealed samples for two of the materials studied. In each case the samples were etched to remove the surface oxide layer immediately before installation in the vacuum chamber. After annealing the 271-sample, the B 1s signal is significantly stronger, as indicated by the improved statistical precision of the plot in Fig. 5.6. However the boron concentration in the sampled region appears to have increased (e.g. as a result of segregation of boron to the surface) by less than a factor of 2 since the ratio of the boron to the silicon intensity is only one-third larger than in the un-annealed sample (see table 5.2). The absence of any strong boron surface segregation with annealing is consistent with the SIMS results [JH+88]. It is suggested that the much improved signal quality, which is associated with a six fold increase in the detected sample current in both the B 1s and Si 2p regions for essentially the same incident photon flux, is related to changes in the structure at the surface which has resulted in a decrease in the work function and thus an increase in the depth sampled.

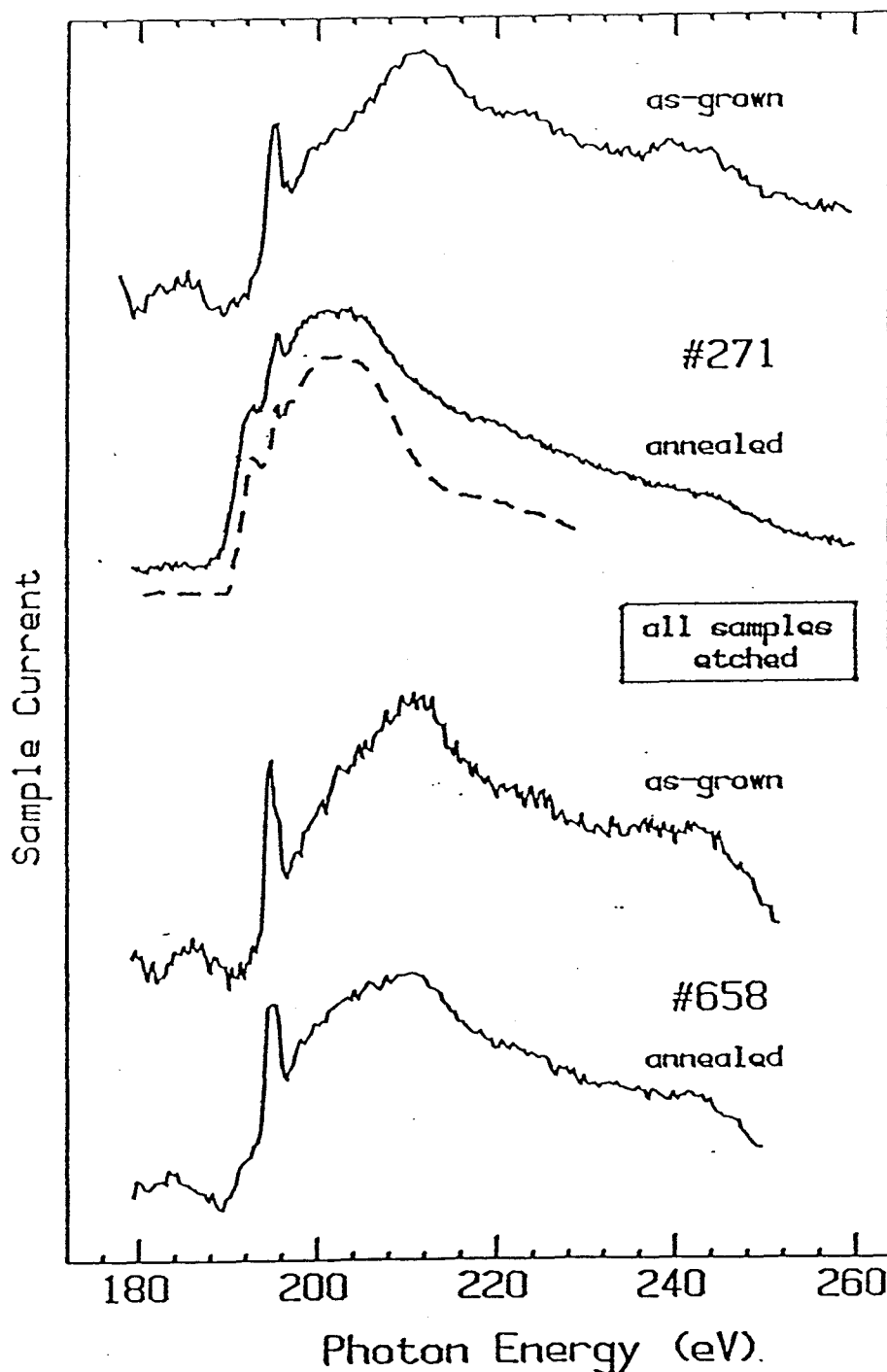


Fig. 5.6 Comparison of the B 1s spectra of the high (271) and low (658) concentration samples, as-grown and after vacuum annealing at 900°C for two hours. All Si(B) samples were etched prior to study. The spectra were measured by sample current detection. A smooth background extrapolated from the pre-edge region has been subtracted in each case. The feature around 184 eV is a Si 2p EXAFS oscillation. The dashed line just below the annealed-271 spectrum is the spectrum of boron.

Table 5.2. Oxygen, Boron and Carrier Concentrations in as-made and annealed Si(B) determined by SIMS and X-ray Absorption

Code	SIMS				XAS			Activity	
	[O] ^a (at.cm ⁻³)	[B] ^b (at.cm ⁻³)	B(at%) rel. ^c		raw ^d	B(at%) ^e rel. ^c		pred. ^f	eCV
658	1x10 ¹⁹	8x10 ¹⁹	.16	(1)	.10	50	(1)	1x10 ¹⁹	3x10 ¹⁹
658A ^g	<2x10 ¹⁸	7x10 ¹⁹	.14	0.9	.15	75	1.4	8x10 ¹⁹	6x10 ¹⁹
271	1x10 ²⁰	3x10 ²⁰	.6	3.8	.13	65	1.2	1x10 ¹⁹	8x10 ¹⁹
271A ^g	2x10 ¹⁹	9x10 ¹⁹	.18	1.1	.17	85	1.6	8x10 ¹⁹	8x10 ¹⁹

- a. Average SIMS concentration in the epilayer determined by 10 keV Cs⁺ bombardment with O⁻ detection. Note, although SIMS indicates a very uniform concentration throughout the full epilayer, determining accurate concentrations in the outer 50 Å by SIMS is very difficult. The estimated accuracy of the bulk epilayer concentration is 10%.
- b. Average SIMS concentration in the epilayer determined by 7.5 keV O₂⁺ bombardment with B⁺ detection.
- c. The entries in the "relative" columns are the ratio of each intensity to that for the 658 sample.
- d. Relative boron intensity expressed as ratio of signal above background at 215 eV (B 1s continuum) to that at 100 eV (Si 2p discrete feature). Uncertainties based on replicate determination are 40%.
- e. This estimate of the atom % of boron in the region sampled by the X-ray measurements assumes that the cross-section for X-ray absorption by Si at 100 eV is five times greater than that of B at 215 eV.
- f. Predicted from the solubility limit of boron in Si (as measured with B₂O₃ doping) [VW69].
- g. Samples annealed in vacuum at 900°C for 2.5 hours. The epitaxial layer in the 658 sample was 2.0 μm thick, grown at 700°C, while that of the 271 sample was 0.6 μm thick,

At the same time there is a dramatic change in spectral shape with annealing of the high boron concentration sample (#271). This may be attributed to a change from a trigonal BO_x to a non-trigonal boron environment. Comparison to the B 1s spectrum of elemental boron (the dashed line in figure 5.6) strongly suggests that after annealing, the boron is surrounded by boron neighbours. However the EHT simulations (Fig. 5.3) predict that boron clusters and $\text{Si}(\text{B}_s)$ may have rather similar B 1s spectra. Thus it is also possible that the change in the B 1s spectrum with annealing is associated with boron changing from a BO_x oxygen-complexed defect environment to a substitutional environment. Since the B 1s spectrum of a sample which unequivocally contains only boron at tetrahedral substitutional sites in silicon has not been obtained, the X-ray absorption evidence must be considered ambiguous.

It must be noted here that an investigation of the B 1s near edge spectrum of the $\text{Si}(111)\text{-B}(\sqrt{3}\times\sqrt{3})\text{R}30^\circ$ system has been reported by McLean et. al. [MTH90]. Their work exhibits significant differences with respect to our results in both experimental results and interpretation. Their B 1s spectra look rather similar to those shown in fig. 5.6 but the sharp feature occurs at 188.6 eV, approximately 7 eV lower than what is reported in this thesis. McLean et. al. [MTH90] attribute this feature as a B 1s excitation into an empty Si dangling bond orbital. In addition, they claim that boron is in a tetrahedral environment. Clarification of these differences is in process. In any event, the absence of any large change in electrical activity with annealing, the fact that this activity is essentially the same as that expected from boron

substitutionally incorporated at the solubility limit (at 900°C [VW69]), and the fact that most of the oxygen is removed with annealing, all suggest that the boron environment in the bulk of the annealed epilayer in the 271 sample is tetrahedral substitutional.

In sharp contrast to the high concentration sample, the shape of the B 1s spectrum of the lower boron concentration sample (#658) does not change appreciably with annealing, indicating that at this concentration (8×10^{19} at.cm⁻³ in the bulk of the epilayer, according to SIMS), the boron in the surface region is in a chemically stable environment. There is no significant change in the absolute amount of boron sampled (as indicated by the signal strength) or in the concentration within the surface region that is sampled by the current detection technique. This is not unexpected since the as-doped boron concentration is about that of the solubility limit at the 900°C anneal temperature and thus there is smaller driving force for chemical changes. The persistence of the 195 eV spike in the spectrum of the annealed 658 sample suggests that the near-surface boron remains in the form of a BO_x complex. The absence of changes in the local boron environment with annealing is not consistent with the SIMS/eCV results (table 5.2), which indicate a large drop in the oxygen concentration in the first 0.1 μm and some increase in electrical activity. This indicates that there could be large differences between the chemistry occurring in the outer 30-50 Å and that in the bulk of the 1 μm thick epilayer. Whenever a highly surface sensitive technique is used one must be very careful in assuming that the surface region

sampled is actually representative of the bulk.

In fact there is clear evidence for boron surface segregation in terms of the amounts of boron that are contributing to the detected X-ray signal. The intensities of the B 1s continuum (at 210 eV) normalised to the spike at 100 eV the Si 2p edge (which is characteristic of bulk silicon) are listed in table 5.2 for all four samples. If the boron in the surface layer sampled by the current detection scheme is in fact representative of the bulk boron, then one would expect that the boron signal in 658 should be four times smaller than that in 271 for the un-annealed samples. This is not the case. The absolute boron concentration can also be crudely estimated. At the indicated energies the Si 2p cross-section is likely about five times larger than the B 1s cross-section (there are 6 Si 2p versus 2 B 1s core electrons; per core electron, Si 2p excitation should be more intense because it is at lower energy; however 2p threshold signals are generally relatively weak compared to 1s near continuum signals because of centrifugal barrier effects). This assumed B1s/Si2p sensitivity factor of 5 has been used to estimate the boron concentration in the layer sampled by the electron yield X-ray measurements. One observes from table 5.2 that the X-ray spectral data (surface) are inconsistent with the SIMS (bulk) both in terms of the absolute and the relative amounts of boron in the 271 and 658 samples. The amount of boron in the surface region is several orders of magnitude greater than that measured by SIMS in the bulk of the epilayer. This indicates that the structure that is deduced from the B 1s spectra of the first 40 Å is unlikely to have any direct relationship to that of the boron in the

deeper portions of the silicon epilayer.

5.9 Conclusions

The model studies reported herein clearly show that B 1s spectroscopy is a very sensitive probe of the local structure of boron. In particular evidence has been presented that a strong sharp feature around 195 eV is related to trigonal coordination by oxygen. Non-trigonally co-ordinated boron, such as the tetrahedral environment of Si(B_g), does not exhibit such a spike. Although the relevance of the Si(B) results to the bulk boron environment remains uncertain since the sample current detection scheme employed is sensitive only to boron in the outer 40 Å, the dramatic variations in the boron spectra with etching, annealing and concentration indicate that B 1s spectroscopy should have very useful applications to studies of boron doping in diamond-lattice semiconductors. With fluorescence detection and/or *in situ* etching the technique should enable detailed studies of boron doping.

Spectra which would be more representative of the bulk environment may have been obtained if ion sputtering or other *in situ* surface cleaning/etching techniques were used. However these were not available at the time of these measurements. Alternatively, and probably preferably, one could use fluorescence detection, which likely probes depths of the order of 0.1 μm at the boron edge. Although a combination of fluorescence detection and *in situ* removal of the surface

layers is likely required to correctly sample the boron environment in the bulk of the epilayer, there are three main problems associated with fluorescence; (1) fluorescence yield is approximately 1×10^{-4} , therefore only 1 in 10,000 B 1s core holes decay by fluorescence rather than Auger; (2) the technology for detecting 150 eV photons is at its limits. Detectors have been only commercially available for about the past 5 yrs; (3) even after solving the technological problems, the depth sensitivity will still only be approximately less than 500 Å. Therefore, how well the 1 μm epilayer is sampled will still be in question.

CHAPTER 6

CONCLUDING REMARKS

The Ni-K edge extended X-ray absorption fine structure of various irreversibly and reversibly thermally annealed samples of the $\text{Pd}_{40}\text{Ni}_{40}\text{P}_{20}$ metallic glass have been measured at 77 K and 300 K with synchrotron radiation and have been analysed through multiple file non-linear least squares curve fitting procedures using MFIT. In all cases, EXAFS spectra for this material have not been recorded previously.

Although the magnitude of the difference plots showed good agreement in most cases with that expected from other studies of the $\text{Pd}_{40}\text{Ni}_{40}\text{P}_{20}$ relaxation processes, the trend lines (variation of R, N, DW, with annealing temperature) differed on analysis based on 77 K and 300 K measured data. Measuring EXAFS at 77 K should generally give more precise but otherwise similar trends to those measured at 300 K. Since the trend lines do not stay the same, this makes one very sceptical of attributing any meaning to the results. In addition, the ratio of coordination number between Ni and Pd obtained from the fitting procedure (0.43) is not consistent with that of 2 deduced from the model A Ni K EXAFS simulations (sec. 4.6). These results lead one to believe that the analysis of the Ni K EXAFS data

is not yet optimized.

The analysis must be explored to a greater degree either by modifying the procedures in fitting, or by program revision. The work presented in chapter 4 will hopefully guide the next graduate student and/or research scientist in the right direction of optimization.

In addition, once MFIT has been optimized and a consistent analysis of the Ni K edge data has been obtained, the Pd K edge data must be analyzed in a similar manner. Hopefully the combination of partial information about the local structure around each atom in the structure (through Ni-K, Pd-K, and eventually P-K EXAFS) will give a more complete picture of the structural changes which occur in irreversible and reversible relaxation of $\text{Pd}_{40}\text{Ni}_{40}\text{P}_{20}$.

The electron yield detection of synchrotron photoabsorption has been used to study the boron K-edge X-ray absorption near edge structure of Si(B) semiconductors. Results showed that B 1s spectroscopy is a very sensitive probe of the local structure of boron. It was found that a strong sharp peak around 195 eV is directly related to trigonally coordinated boron, analogous to Hallmeier et. al. [HS+81, SM+83] who have attributed this feature to boron trigonally coordinated in various minerals. Although McLean et. al. [MTH90] attribute a similar feature in the B 1s spectrum of an ordered B overlayer on Si(111), to B 1s excitation to an unoccupied dangling Si bond orbital, the present results suggest that non-trigonally co-

ordinated boron, such as the tetrahedral environment of Si(B_g), should not exhibit such a spike. Although the relevance of the present results to the bulk boron environment of the Si(B) epilayer is still uncertain since the sample current detection technique used is sensitive only to boron in the outer 40 Å, the dramatic variations in the boron spectra with HF etching, annealing and concentration indicate that B 1s spectroscopy should have very useful applications studies of boron doping in diamond-lattice semiconductors. With fluorescence detection and/or *in situ* etching the technique should enable detailed studies of boron doping.

Spectra which would be more representative of the bulk environment may have been obtained if we had used ion sputtering or other *in situ* surface cleaning/etching techniques. However these were not available at the time of these measurements. Alternatively one could use fluorescence detection, which probes deeper into the bulk (up to $\approx 0.1 \mu\text{m}$) at the boron edge. A combination of fluorescence detection and *in situ* removal of the surface layers is probably needed to correctly sample the boron environment in the bulk of the epilayer. However there are considerable challenges in fluorescence detection. Firstly, the fluorescence yield is approximately 1×10^{-4} , only 1 in 10,000 B 1s core holes decay by fluorescence rather than Auger. Secondly, the technology for detecting 150 eV photons is at its limits. Detectors have been available commercially for only about the past 5 years. Finally, even after solving the technological problems, the depth sensitivity will still be only approximately 500 Å. Therefore, how well the 1 μm epilayer is sampled will still be

in question.

X-ray absorption with synchrotron radiation has been shown to be a probe of the local atomic structure of different materials. The Ni K EXAFS showed the sensitivity of EXAFS to chemical ordering of the metallic glasses, both with alloy and amorphous metal comparison, and the difference plots. Although the curve fitting procedure was not optimized, and similar trends at both temperatures were not observed in all cases, one can see the potential curve fitting has in determining aspects of the local structure. In addition, electron yield XANES studies of the boron environment in Si(B) semiconductors show promise, even though there are unresolved problems associated with the high surface sensitivity. X-ray absorption techniques such as EXAFS and XANES are definitely useful structural tools for materials science.

REFERENCES

- Reference Codes:** year of publication preceded by:
initials of all authors (if < 3) or initials of first two
and if code is not unique, small a,b,c,...distinguishes.
- AA71** C.L. Alley, K.W. Atwood, Semiconductor Devices and Electronic Circuits., John Wiley and Sons, Inc., New York, 1971.
- AD75** C.A. Ashley and S. Doniach, *Phys. Rev. Lett.*, **27**, 1279 (1975).
- AT85** N. Aizaki, and T. Tatsumi, Extended Abstracts of the 17th Conference on Solid State Devices and Materials, (*Jap. Soc. Appl. Phys.*, 301 (1985)).
- AW85** S. Ainworth and D.P. Woodruff, *Solid State Commun.* **56**, 461 (1985).
- B70** E.P. Bertin, Principles and Practice of X-Ray Spectrometric Analysis, Plenum Press, New York, 35-38 (1970).
- B77** Structure Data of Free Polyatomic Molecules, Landolt-Bornstein New Series II (Springer-Verlag, Berlin, 1977) Vol. 7.
- B79** A. Bar-Lev, Semiconductors and electronic devices., Prentice Hall International, London, 1979.
- B80** A. Bianconi, *Appl. Surf. Sci.*, **6**, 392 (1980).
- B85** J.C. Bean, *Science.*, **230**, 127 (1985).
- BF+85** A. Bionconi, E.Fritsch, G. Calas, J. Petiou, *Phys. Rev. A.*, **32**, 4292 (1985).
- BGT67** C. Bingham, M.D. Godfrey, J.W. Turkey, IEE Trans. Audio and Electroacoust., **15** (2), 58 (1967).

- BK74** R.L. Barinskii and I.M. Kulikova, *Bull. Acad. Sci. USSR Phys. Ser.*, **38**, 16 (1974).
- BK89** E. Beaurepaire, J.P. Kappler, *Phys. Rev. B.*, **41**, 6768 (1989)
- BM+89** S. Bodeur, P. Millie, E. Lizon a Lagrin, I. Nenner, A. Fillipponi, F. Boscherini, S. Mobilio, *Phys. Rev. A.*, **39**, 5075 (1989).
- BRS90** R. Brüning, D.H. Ryan and J.O. Ström-Olsen, *Hyperfine Interactions* (submitted).
- BS59** H. Bethe and E. Salpeter, Quantum Mechanics of One and Two-electron Systems, Springer, Berlin, 1959, sections 59,69.
- BS83** D. Briggs, M.P. Seah, Practical Surface Analysis, John Wiley and Sons, New York, 123 (1983)
- BS90** R. Brüning and J.O. Ström-Olsen, *Phys. Rev. B* (1990) submitted.
- BTB87** G.M. Bancroft, K.H. Tan, and J.D. Bozek, Physics in Canada, (1987) 113.
- C84** G.S. Cargill III, *J. Non Crystalline Solids.*, **61**, 261 (1984).
- C85** P.H. Citrin, *Phys. Rev. B*, **31**, 700 (1985).
- CB+87** M. Choi, J. Budnick, G.H. Hayes, D.M. Pease, S.M. Heald, D.E. Sayers and R. Hasegawa., *Phys. Rev. B*, **36**, 4613 (1987).
- CBJ84** N.S. Chiu, S.H. Bauer, M.F.L. Johnson, *J. Mol. Struc.*, **125**, 33 (1984).
- CB+89** M. Choi, J.I. Budnick, D.M. Pease, G.H. Hayes, J. Wong, *Phys. Rev. B.*, **41**, 9654 (1989)
- CE+87** G. Cocco, S. Enzo, A. Balerna, S. Mobilio J.M. Dubois, *Phys. Rev. B.*, **36**, 4734 (1987).
- CG+85** E. Chasen, A.L Greer, K.F. Kelton, P.S. Pershan, L.B. Sorensen, F. Spaepen and A.H. Weiss., *Phys. Rev. B*, **32**, 3399 (1985).
- CK+78** H.S. Chen, L.C. Kimerling, J.M. Poate and V.L. Brown, *Appl. Phys. Lett.*, **32**, 461 (1978).

- CT80** B.C. Chaudari, D. Turnbull, *Scientific American*, **242 NO. 4**, 98 (1980).
- D86** G.H. Dohler, *CRC Crit. Rev. Solid State Mater. Sci.*, **13**, 196 (1986).
- DD+79** J.L. Dehmer, D. Dill, in: Electron-molecule and photon-molecule collisions, eds. T.N. Rescigno, B.V. McKoy and B. Schneider (plenum Press, New York, 225 (1979). J.L. Dehmer, D. Dill, A.C. Parr, in: Photophysics and photochemistry in the vacuum ultraviolet, eds. S.P. McGlynn, G. Findley and R. Huebner (Deidel, Dordrecht,(1983).
- E90** W.F. Egelhoff, Jr., *Crit. Rev. Sol. St. Mat. Sci.*, **16**, 213 (1990).
- EW+88** A. Erbil, W. Weber, G.S. Cargill III, and R.F. Boehme, *Phys. Rev. B.*, **34**, 1392 (1984); K.C. Pandey, A. Erbil, G.S. Cargill III, and R.F. Boehme, *Phys.Rev. Lett.* **61**, 1282 (1988).
- F68** V.A. Fomichev, *Sov. Phys. Solid State.*, **9**, 2496 (1968).
- F82** J.S. Faulkner, *Prog. Mater. Sci.*, **27**, 3 (1982).
- FRW86** E. de Frésart, S.S. Rhee, and K.L. Wang, *Appl. Phys. Lett.* **49**, 847, (1986).
- FWR88** E. de Frésart, K.L. Wang, and S.S. Rhee, *Appl. Phys. Lett.*, **53**, 48 (1988).
- G87** C.R.M. Grovenor, Materials for Semiconductor devices., The Institute of Metals, 1987.
- GD+81** G.N. Greaves, P.J. Durham, P. Quinn, G. Diakun, *Nature (London)*, **294**, 139 (1981).
- GG+82** P.H. Gaskel, D.M. Glover, A.K. Livesey, P.J. Durham, G.N. Greaves, *J. Phys. C*, **15**, L597 (1982).

- GL81** T. Gustafsson, H.J. Levinson, *Chem. Phys. Lett.*, **78**, 28 (1981);
A. Bianconi, in: Proceedings of the First International Conference on EXAFS and XANES, Frascati, Italy, 1982, Springer Series in Chemical Physics, Springer Berlin, **27**, 118 (1983);
A. Bianconi, M. Dell' Ariccia, A. Gargana, C.R. Natoli, in: Proceedings of the First International Conference on EXAFS and XANES, Frascati, Italy, 1982, Springer Series in Chemical Physics, Springer Berlin, **27**, 57 (1983);
- H78** reviews of EXAFS of amorphous materials: T.M. Hayes, *J. Non-Crystalline Solids.*, **31**, 57 (1978);
- H89** A.P. Hitchcock, *Ultramicroscopy.*, **28**, 165 (1989).
- H90** A.P. Hitchcock, *Physica Scripta.*, (1990) in press.
- HB80** A.P. Hitchcock, C.E. Brion, *J. El. Spec.*, **18**, 1 (1980).
- HB81** A.P. Hitchcock, C.E. Brion, *J. Phys.* **B14**, 4399 (1981).
- HB82** T.M. Hayes and J.B. Boyce, *Solid State Phys.*, **37**, 173 (1982).
- HB+84** A.P. Hitchcock, S. Beaulieu, T. Steel, J. Stöhr and F. Sette, *J. Chem. Phys.*, **80**, 3927 (1984).
- HI+83** A. Hasegawa, H. Ihara, M. Hayashi and M.C.R. Symons., *Mol. Phys.* **50**, 1273 (1983).
- HS80** M. Heald, E.A Stern, *Synth. Met.*, **1**, 249 (1980).
- HS+81** K.H. Hallmeier, R. Szargan, A. Meisel, E. Hartmann and E.S. Gluskin, *Spectrochimica Acta.*, **37A**, 1049 (1981).
- I84** T. Ishii, *Prog. Theor. Phys.* **72**, 412 (1984).
- IC+85** A. Inoue, H.S. Chen, T. Masumoto and S.A. Ajuria., *Sci. Rep. RITU A32*, 116 (1985).
- JH+88** T.E. Jackman D.C. Houghton, K. Song, J. McCaffrey, M.W. Denhoff, J.A. Jackman and C.G. Tuppen, *Appl. Phys. Lett.*, **53**, 877 (1988).

- JW+88** J.A. Jackman, P. Williams, T.E. Jackman, and D.C. Houghton, *in Proceedings of the 6th Int. Conf. on SIMS*, A. Beninghoven and H.W. Werner (eds.) (Wiley, London, 521 (1988)).
- K79** C. Kunz, Synchrotron Radiation Techniques and Applications., Springer-Verlag Berlin Heidelberg, 1 (1979).
- K86** J. Kirz et. al., X-ray Data Booklet, Lawrence Berkeley Laboratory, University of California, 6-2 (1986)
- KB88** K.E. Kasper and J.C. Bean, Eds, *Silicon Molecular Beam Epitaxy* (CRC Boca Ratan, FL,1988)
- KLP84** R.A.A. Kubiak, W.Y. Leong, and E.H.C. Parker, *Appl. Phys. Lett.*, **44**, 878 (1984).
- KP88** D.C. Koningsberger, R. Prins, X-ray Absorption Principles: Applications, Techniques of EXAFS, SEXAFS and XANES, John Wiley and Sons, 53-84, (1988).
- L89** F.W. Lytle, *Phys. Chem.*, **91**, 1251 (1987).
- LA85** E. Lindholm and L. Åsbrink, Molecular orbitals and their energies, studied by the semiempirical HAM Method (Springer, Berlin, 1985), p.150.
- LB77** P.A. Lee and G. Beni, *Phys. Rev. B.*, **15**, 2862 (1977).
- LC+81** P.A. Lee, P.H. Citrin, P. Eisenberger, B.M. Kinkaid, *Rev. Mod. Phys.*, **53** (4), 769 (1981).
- LL88** E. Lindholm and J. Li, *J. Phys. Chem.*, **92**, 1731 (1988).
- LP75** P.A. Lee and J.B. Pendry, *Phys. Rev. B.*, **11**, 2795 (1975).
- LSS75** F.W. Lytle, D.E. Sayers and E.A. Stern, *Phys. Rev. B.*, **11**, 4825 (1975).
- M67** E.L. Muetterties, The Chemistry of Boron and its Compounds, (Wiley, New York, 1967).

- MDG82** M.C. Munoz, P.J. Durham, and B.L. Gyorffy, *J. Phys. F*, **12**, 1497, (1982).
- MK+69** W.H. McMaster, N. Kerr del Grande, J.H. Mallet and J.H. Hubbel, *Compilation of X-ray cross sections*, Rep. UCRL-50/74, Section 2, Rev. 1, 1969 (Lawrence Radiation Laboratory, University of California)
- MO+89** M. Monita, T. Ohmi, E. Hasegawa, M. Kawakami, K. Suma, *Appl. Phys. Lett.*, **55**, 562 (1989).
- MTH90** A.B. McLean, L.J. Terminello, F.J. Himpsel, *Phys. Rev. B.*, **41**, 7694 (1990).
- MT+88** H. Maeda, H. Terauchi, M. Hida, N. Kamijo and K. Osamura, Proc. EXAFS-3, Springer Proc. in Phys. 2 (1984) (FeZr); K.B. Garg, K.S. Jerath, H.S. Chauhan and U. Chandra, *Ind. J. Phys.*, **62A**, 107 (1988) (CuZr).
- MV+72** S.P. McGlynn, L.G. Vanquickenbone, M. Kinoshita, and D.G. Carroll, *Introduction to Applied Quantum Chemistry*, (Holt, Rinehart and Winston, NY, 1972). The extended Hückel program is the Hoffman version supplied by the Quantum Chemical Program Exchange (QCMP011).
- MV+88** A.G. McKale, B.W. Veal, A.P. Paulikas, S.K. Chan, G.S. Knapp, *J. Am. Chem. Soc.*, **110**, 3763 (1988).
- N83** R. Natoli, in: *Proceedings of the First International Conference on EXAFS and XANES*, Frascati, Italy, 1982, *Springer Series in Chemical Physics*, **27**, 43 (1983).
- NAV88** S.V. Nekipelov, V.N. Akimov, A.S. Vinogradov, *Opt. Spectrosc.*, **64**, 487 (1988); *ibid*, *Sov. Phys. Sol. St.*, **30**, 2095 (1988).
- O89** B. Oliver (unpublished).
- OA86** R.M. Ostrom and F.G. Allen, *Appl. Phys. Lett.*, **48**, 221 (1986).
- OR+80** A.E. Orel, T.N. Resigno, B.V. Mckoy and P.W. Langhoff., *J. Chem. Phys.* **72**, 1265 (1980).

- P58** W.P. Pearson, Handbook of Lattice Spacings and Structures of Metals and Alloys, (Pergammon, London, 1958).
- P86** R. People, *IEE J. Quantum Electron.*, **22**, 1696, (1986).
- RA90** J.J. Rehr, R.C. Albers, *Phys. Rev. B.*, **41**, 8139 (1990).
- RM62** Gerald D. Riek and Caroline H. Macgillavry, International Tables For X-ray Crystallography, The Kynoch Press, Birmingham, England, **3**, 157 (1962).
- RS49** B.B. Rossi and H.H. Staub, Ionization Chambers and Counters: Experimental Techniques, McGraw-Hill, New York, 1949.
- RS+76** K. Radler, B. Sonntag, T.C. Chang and W.H.E. Schwarz, *Chem. Phys.*, **13**, 363 (1976); W.H.E. Schwarz, *Chem. Phys.*, **11** (1975) 217; W.H.E. Schwarz, T.C. Chang, U. Seeger and K.H. Huang, *Chem. Phys.*, **117**, 73 (1989).
- S74** E.A. Stern, *Phys. Rev. B*, **10**, 3027, (1974).
- S82** E.A. Stern, *Phys. Rev. Lett.*, **49**, 1353 (1982).
- S88a** J. Stöhr, p 618 in KP88
- S88b** IBID p 45
- S88c** IBID p 480
- SB88** D.E. Sayers, B.A. Bunker, in KP88 423 (1988)
- SB+88a** J.O. Ström-Olsen, R. Brüning, Z. Altounian and D.H. Ryan, *J. Less-Common Metals.*, **145**, 327 (1988).
- SB+88b** J.O. Ström-Olsen, R. Brüning, Z. Altounian and D.H. Ryan, Structural Relaxation in Metallic Glasses., invited review at the European Materials Research Society meeting, Strasbourg, June, 1988.
- SG+89** J.A. Sheehy, T.J. Gil, C.L. Winstead, R.E. Farren, P.W. Langhoff, *J. Chem. Phys.* **91**, 1796 (1989)

- SM+83** W.H.E. Schwartz, L. Mensching, K.H. Hallmeier, and R. Szargan, *Chem. Phys.*, **82**, 57 (1983).
- SSH84** F. Sette, J. Stöhr and A.P. Hitchcock, *J. Chem. Phys.* **81**, 4906 (1984).
- SSL71** D.E. Sayers, E.A. Stern and F.W. Lytle, *Phys. Rev. Lett.*, **27**, 1204 (1971).
- SSL75** E.A. Stern, D.E. Sayers and F.W. Lytle, *Phys. Rev. B.*, **11**, 4836 (1975).
- TB+82** K.H. Tan, G.M. Bancroft, LL Coatsworth and B.W. Yates, *Can. J. Phys.* **60**, 131 (1982).
- TH89** T. Tyliczak and A.P. Hitchcock, *Physica B.*, **158**, 335 (1989).
- THA87** T. Tatsumi, H. Hirayama, and N. Aizaki, *Appl. Phys. Lett.*, **50**, 1234 (1987); *ibid*, in press.
- THA88** T. Tatsumi, H. Hirayama, and N. Aizaki, in Silicon Molecular Beam Epitaxy II, J.C. bean and L.J. Schowalter (eds.) (CRC Boca Ratan, FL, 1988) p. 430.
- THJ90** T. Tyliczak, A.P. Hitchcock, and T.E. Jackman, *J. Vac. Sci. Tech. A.*, (1990) in press.
- TL79** B.K. Teo, P.A. Lee, *J. Am. Chem. Soc.*, **101**, 2815 (1979).
- TP+88** C.G. Tuppens, K. A. Prior, C.J. Gibbons, T.E. Jackman, and D.C. Houghton, *Appl. Phys. Lett.*, **64**, 2751 (1988).
- TS+80** A.I. Taub and F. Spaepen, *Acta Metall.*, **28**, 1781 (1980).
- VW69** G.L. Vick and K.N. Whittle, *J. Electroanalytical Soc.* **116**, 1142 (1969).
- W50** D.H. Wilkinson, Ionization Chambers and Counters, Cambridge University Press, 1950.
- W83** G. Wendin, EXAFS and Near edge structure, A. Bionconi, L. Incoccia, and S. Stipich (Eds), Springer-Verlag, Berlin 29 (1983).
- W86** J. Wong, *Mat. Sci. Eng.*, **80**, 107 (1986).

- W88** A.C. de Wilton (1988) unpublished.
- WL+84** J. Wong, F.W. Lytle, P.P. Messmer, D.H. Maylotte, *Phys. Rev. B.*, **30**, 5596 (1984).
- WSW87** A.C. de Wilton, M. Simard-Normandin, and P.T.T. Wong, *Can. J. Phys.*, **65**, 821 (1987).
- Y87** M. Ya Amusia, in *Atomic Physics 5, Proceedings of VInternational Conference on Atomic Physics*, R. Marrus, M. Prior, and H. Shugart (Eds.), Plenum, New York, 537 (1987).
- YR+88** Z. Yu, D. Rongheng, H. Gongxian and H. Zhangyi, *J. Mat. Sci. Lett.*, **7**, 555 (1988).

APPENDIX I

**Multifitting Results Obtained From MFIT For
Various Irreversibly Annealed Pd₄₀Ni₄₀P₂₀ Metallic
Glass Samples Recorded at 300 K with
Synchrotron Radiation.**

component 1 Oni.ak2
 component 2 Opd.ak2
 component 3 Op.ak2
 parameter file irrbrt.par

Onini.pk2
 Onipd.pk2
 Onip.pk2

sumsq= 2.00037E-02

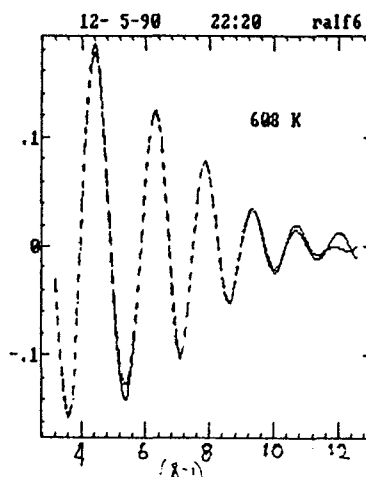
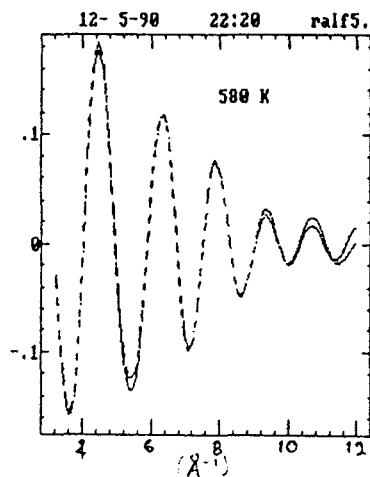
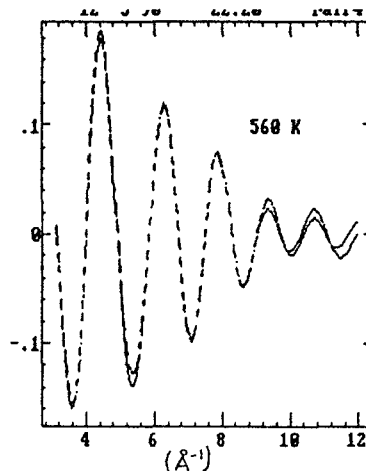
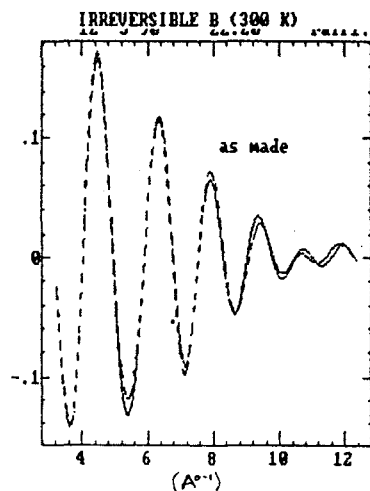
	ralf1.f					ralf4.f			
R	2.495	2.680	2.210	.0000	2.495	2.670	2.217	.0000	
N	.397	1.38	.732	.000	.429	2.19	.892	.000	
DW	1.30E-03	3.02E-02	2.67E-03	0.00E+00	1.30E-03	4.08E-02	5.03E-03	0.00E+00	
E0	.47	-.90	2.45E-02	.00	.47	-.90	2.45E-02	.00	
	ralf5.f					ralf6.f			
R	2.495	2.682	2.211	.0000	2.495	2.685	2.215	.0000	
N	.457	1.54	.869	.000	.458	1.64	.845	.000	
DW	1.30E-03	3.14E-02	5.47E-03	0.00E+00	1.30E-03	3.32E-02	4.33E-03	0.00E+00	
E0	.47	-.90	2.45E-02	.00	.47	-.90	2.45E-02	.00	

fixed parameters

1 2 3 0 0 0 0 0 0 0 0 0 0 0 0 0
 0 0 0 0 0 0 0 0 0 0 0 0 0 0 0 0

Parameters

component	1 file				2 file				3 file				4 file			
	1	2	3	4	1	2	3	4	1	2	3	4	1	2	3	4
R	18	19	20	0	18	21	24	0	18	22	25	0	18	23	26	0
N	6	4	5	0	7	10	13	0	8	11	14	0	9	12	15	0
DW	30	16	17	0	30	31	27	0	30	32	28	0	30	33	29	0
E0	1	2	3	0	1	2	3	0	1	2	3	0	1	2	3	0



APPENDIX II

**Multifitting Results Obtained From MFIT For
Various Reversibly Annealed Pd₄₀Ni₄₀P₂₀ Metallic
Glass Samples Recorded at 300 K with
Synchrotron Radiation**

component 1 Oni.ak2
 component 2 Opd.ak2
 component 3 Op.ak2
 parameter file revbrt.par

Onini.pk2
 Onipd.pk2
 Onip.pk2

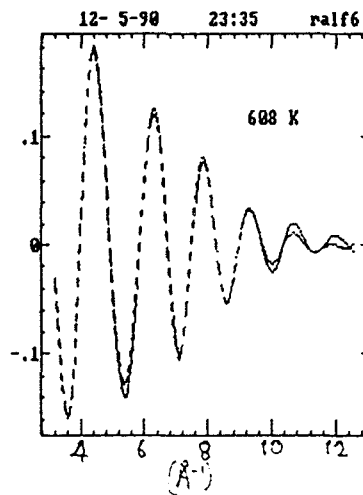
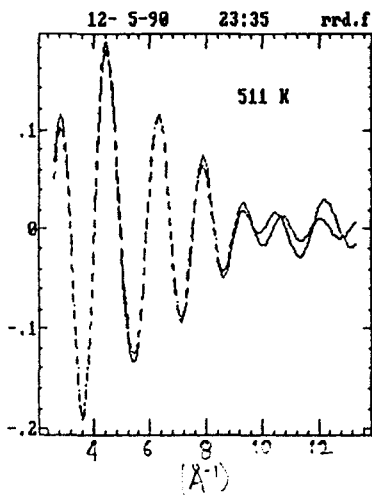
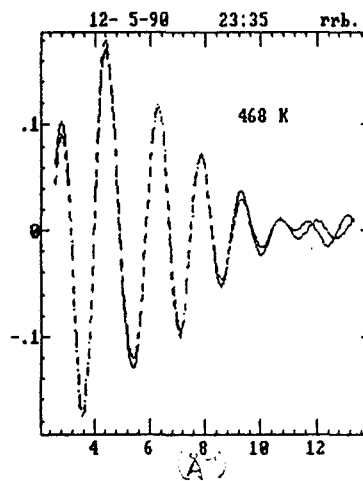
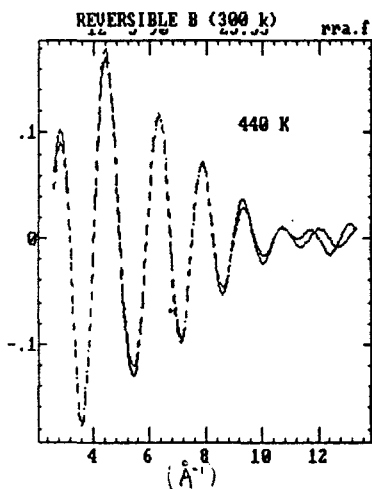
sumsq= 3.46130E-02

	rra.f				rrb.f			
R	2.474	2.713	2.209	.0000	2.474	2.713	2.209	.0000
N	.585	1.26	.684	.000	.587	1.25	.679	.000
DW	3.17E-03	2.50E-02	3.59E-03	0.00E+00	3.17E-03	2.48E-02	3.48E-03	0.00E+00
E0	5.5	-3.45E-02	-.97	.00	5.5	-3.45E-02	-.97	.00
	rrd.f				ralf6.f			
R	2.474	2.703	2.202	.0000	2.474	2.694	2.213	.0000
N	.582	1.61	.785	.000	.583	.659	.715	.000
DW	3.17E-03	3.22E-02	5.62E-03	0.00E+00	3.17E-03	1.39E-02	3.39E-03	0.00E+00
E0	5.5	-3.45E-02	-.97	.00	5.5	-3.45E-02	-.97	.00

fixed parameters

3 6 9 0 0 0 0 0 0 0 0 0 0
 0 0 0 0 0 0 0 0 0 0 0 0

component	Parameters															
	1 file				2 file				3 file				4 file			
	1	2	3	4	1	2	3	4	1	2	3	4	1	2	3	4
R	1	4	7	0	1	22	25	0	1	23	26	0	1	24	27	0
N	10	11	12	0	13	16	19	0	14	17	20	0	15	18	21	0
DW	2	5	8	0	2	28	31	0	2	29	32	0	2	30	33	0
E0	3	6	9	0	3	6	9	0	3	6	9	0	3	6	9	0



APPENDIX III

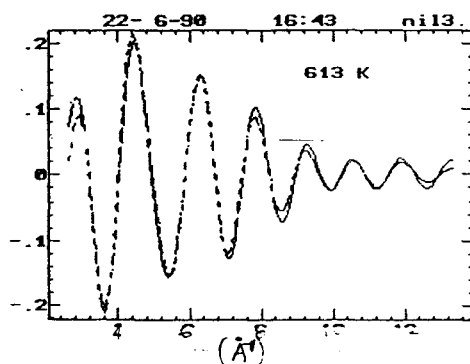
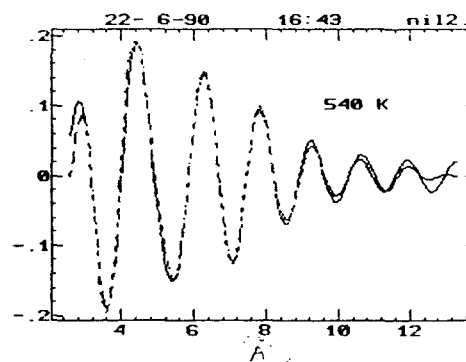
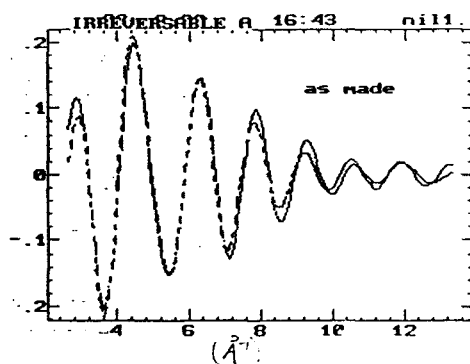
**Multifitting Results Obtained From MFIT For
Various Irreversibly Annealed Pd₄₀Ni₄₀P₂₀ Metallic
Glass Samples Recorded at 77 K with
Synchrotron Radiation**

	nil1.f				nil2.f			
R	2.519	2.708	2.205	.0000	2.509	2.704	2.212	.0000
N	.750	3.24	.953	.000	.690	3.84	.805	.000
DW	2.64E-03	4.37E-02	5.89E-03	0.00E+00	1.44E-03	1.97E-02	3.44E-03	0.00E+00
E0	.00	.00	.00	.00	.00	.00	.00	.00

	nil3.f			
R	2.517	2.710	2.209	.0000
N	.674	3.43	.918	.000
DW	1.60E-03	4.53E-02	4.29E-03	0.00E+00
E0	.00	.00	.00	.00

Parameters

component	1 file				2 file				3 file			
	1	2	3	4	1	2	3	4	1	2	3	4
R	31	13	16	0	32	14	17	0	33	15	18	0
N	4	7	19	0	5	8	11	0	6	9	12	0
DW	19	34	37	0	20	35	38	0	21	36	39	0
E0	1	2	3	0	1	2	3	0	1	2	3	0



APPENDIX IV

**Multifitting Results Obtained From MFIT For
Various Reversibly Annealed Pd₄₀Ni₄₀P₂₀ Metallic
Glass Samples Recorded at 77 K with
Synchrotron Radiation**

component 1 Oni.ak2
 component 2 Opd.ak2
 component 3 Op.ak2
 parameter file revalt.par

Onini.pk2
 Onipd.pk2
 Onip.pk2

sumsq= 9.20734E-02

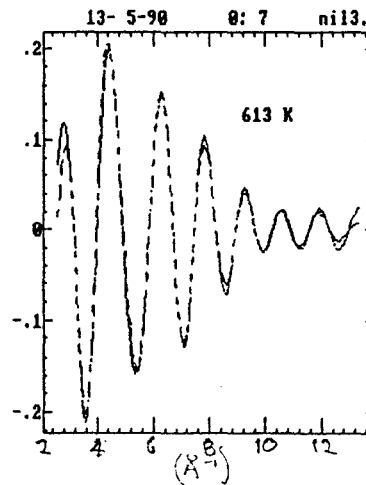
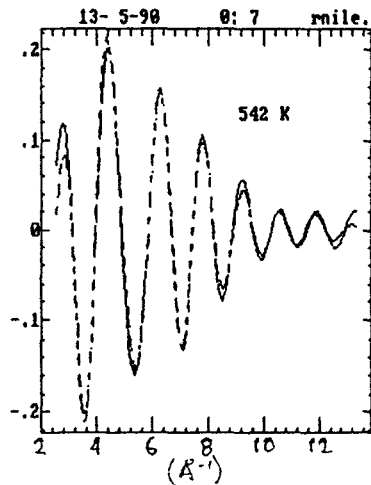
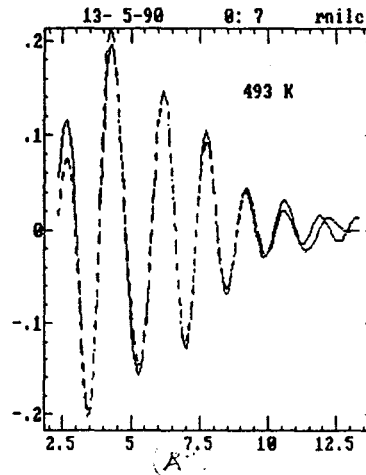
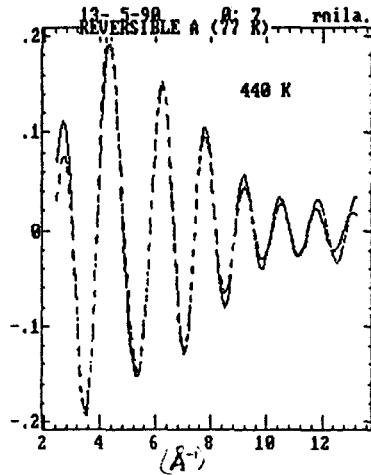
	rnila.f				rnilc.f			
R	2.530	2.771	2.235	.0000	2.519	2.767	2.249	.0000
N	.440	1.88	1.01	.000	.496	2.41	1.20	.000
DW	-1.24E-03	3.54E-02	3.60E-03	0.00E+00	1.33E-03	4.37E-02	5.89E-03	0.00E+00
E0	.00	.00	.00	.00	.00	.00	.00	.00
	rnile.f				nil3.f			
R	2.517	2.742	2.229	.0000	2.509	2.709	2.212	.0000
N	.593	3.23	1.02	.000	.626	3.95	.891	.000
DW	9.51E-04	4.53E-02	4.29E-03	0.00E+00	1.08E-03	4.97E-02	3.44E-03	0.00E+00
E0	.00	.00	.00	.00	.00	.00	.00	.00

fixed parameters

1	2	3	0	0	0	0	0	0	0	0	0	0	0	0	0	0
0	0	0	0	0	0	0	0	0	0	0	0	0	0	0	0	0

Parameters

	1 file				2 file				3 file				4 file			
component	1	2	3	4	1	2	3	4	1	2	3	4	1	2	3	4
R	19	20	21	0	31	22	25	0	32	23	26	0	33	24	27	0
N	6	4	5	0	7	10	13	0	8	11	14	0	9	12	15	0
DW	16	17	18	0	28	34	37	0	29	35	38	0	30	36	39	0
E0	1	2	3	0	1	2	3	0	1	2	3	0	1	2	3	0



component 1 Oni.ak2
 component 2 Opd.ak2
 component 3 Op.ak2
 parameter file revblt.par

Onini.pk2
 Onipd.pk2
 Onip.pk2

sumsq= 1.09308E-01

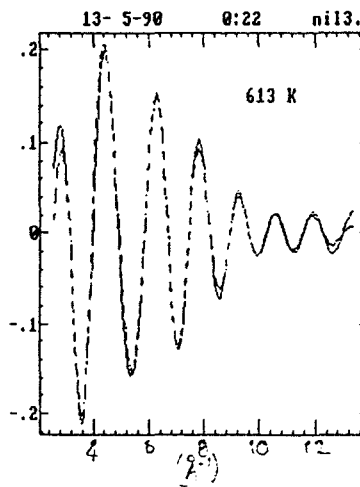
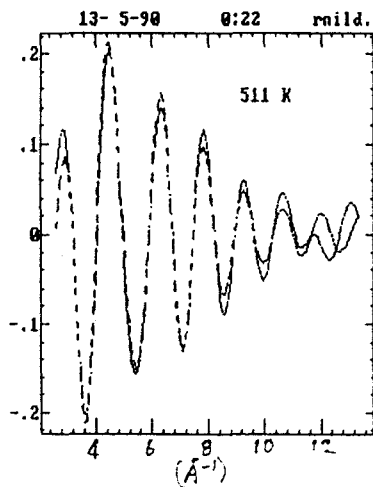
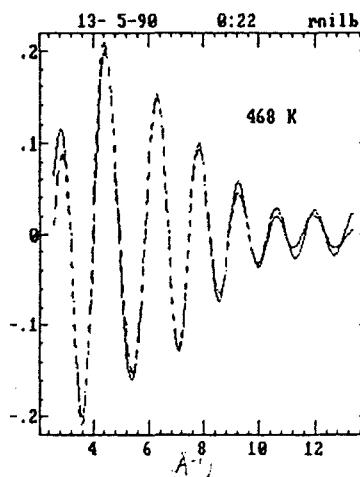
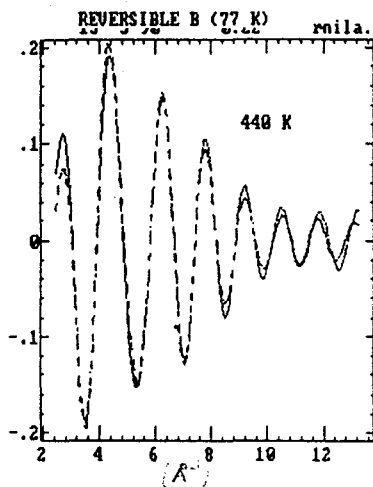
	rnila.f				rnilb.f			
R	2.530	2.771	2.235	.0000	2.504	2.698	2.208	.0000
N	.458	1.88	1.02	.000	.674	3.55	.905	.000
DW	-9.19E-04	3.51E-02	3.84E-03	0.00E+00	1.15E-03	4.51E-02	4.66E-03	0.00E+00
EO	.00	.00	.00	.00	.00	.00	.00	.00

	rnild.f				nil3.f			
R	2.503	2.704	2.210	.0000	2.509	2.709	2.212	.0000
N	.822	3.19	.915	.000	.626	3.96	.891	.000
DW	2.31E-03	3.94E-02	5.59E-03	0.00E+00	1.08E-03	4.97E-02	3.44E-03	0.00E+00
EO	.00	.00	.00	.00	.00	.00	.00	.00

fixed parameters

1 2 3 0 0 0 0 0 0 0 0 0 0
 0 0 0 0 0 0 0 0 0 0 0 0

component	Parameters															
	1 file				2 file				3 file				4 file			
	1	2	3	4	1	2	3	4	1	2	3	4	1	2	3	4
R	19	20	21	0	31	22	25	0	32	23	26	0	33	24	27	0
N	6	4	5	0	7	10	13	0	8	11	14	0	9	12	15	0
DW	16	17	18	0	28	34	37	0	29	35	38	0	30	36	39	0
EO	1	2	3	0	1	2	3	0	1	2	3	0	1	2	3	0



component 1 Oni.ak2
 component 2 Opd.ak2
 component 3 Op.ak2
 parameter file revclt.par

Onini.pk2
 Onipd.pk2
 Onip.pk2

sumsq= 2.21128E-01

	rnila.f					rnilb.f			
R	2.530	2.771	2.235	.0000	2.504	2.698	2.208	.0000	
N	.457	1.88	1.02	.000	.674	3.55	.906	.000	
DW	-9.37E-04	3.52E-02	3.84E-03	0.00E+00	1.15E-03	4.51E-02	4.67E-03	0.00E+00	
EO	.00	.00	.00	.00	.00	.00	.00	.00	
	rnilf.f					nil3.f			
R	2.503	2.703	2.210	.0000	2.509	2.709	2.212	.0000	
N	.820	3.20	.916	.000	.625	3.97	.891	.000	
DW	2.29E-03	3.96E-02	5.60E-03	0.00E+00	1.07E-03	4.99E-02	3.42E-03	0.00E+00	
EO	.00	.00	.00	.00	.00	.00	.00	.00	

fixed parameters

1 2 3 0 0 0 0 0 0 0 0 0 0 0 0 0 0 0 0 0
 0

component	Parameters															
	1 file				2 file				3 file				4 file			
	1	2	3	4	1	2	3	4	1	2	3	4	1	2	3	4
R	19	20	21	0	31	22	25	0	32	23	26	0	33	24	27	0
N	6	4	5	0	7	10	13	0	8	11	14	0	9	12	15	0
DW	16	17	18	0	28	34	37	0	29	35	38	0	30	36	39	0
EO	1	2	3	0	1	2	3	0	1	2	3	0	1	2	3	0

